Quantum Transport in Disordered and Strain-Engineered Graphene

Sebastian Gattenlöhner

Dissertation
submitted for the degree of
Doctor of Philosophy
to the Institute of Photonics and Quantum Sciences
at Heriot-Watt University, Edinburgh

Oktober 2014

Abstract

The first part of the present thesis investigates the electronic transport in strain-engineered graphene, which has been proposed as a way to circumvent the problem of an absent band-gap in this material. To that end, we calculate the conductivity, the shot noise and the density of states in the Dirac-Kronig-Penney model, which describes the phase-coherent transport in clean monolayer samples with a one-dimensional periodic modulation of the strain and the electrostatic potential. We find that periodic strains induce large pseudo-gaps and suppress charge transport in the direction of the strain modulation while the effect for periodic electrostatic potentials is weakened by Klein tunnelling.

The second part then deals with the transport properties of graphene at charge neutrality when disordered by adatoms or scalar impurities. A scattering theory for the Dirac equation yields an analytic expression for the conductivity given a particular impurity configuration; an averaging over impurity configurations is performed numerically. For strong magnetic fields, the conductivity equals the ballistic value, while for weaker fields, a rich scaling flow is obtained which is governed by fixed points of different symmetry classes. In the absence of a magnetic field, a surprising rise of the conductivity is observed when increasing the density of adatoms that are randomly arranged on sites of the same Bloch-phase.

Acknowledgements

Writing this thesis was only possible with the help and support of many kind people to whom I would like to express my most sincere gratitude.

First and foremost, I am indebted to my supervisor Dr Mikhail Titov. I am infinitely grateful for his constructive scientific guidance, his good sense of humour, which was a constant source of encouragement, and the many things he taught me along the way. I would also like to thank him for giving me the opportunity to visit him at the University of Nijmegen on several occasions during the final phase of my PhD.

The research presented in this thesis has been conducted in collaboration with many remarkable physicists. My deepest thanks go to Prof Wolfgang Belzig, Dr Igor Gornyi, Dr Wolf–Rüdiger Hannes, Prof Alexander Mirlin, and Dr Pavel Ostrovsky for giving me the opportunity to work with and learn from them. I am particularly grateful to Dr Jörg Schelter and Prof Björn Trauzettel from whom I learned a lot on the numerical aspects of quantum transport in graphene during extended visits to the University of Würzburg.

My time at the Heriot Watt University will always be connected with fond memories; many people have contributed to that. I am particularly indebted to Prof Mats Jonson for being a very supportive second supervisor and would also like to express my sincere gratitude to Prof Ian Galbraith and Prof Patrik Öhberg for helping me on numerous occasions. I was very fortunate to have been in the enjoyable and inspiring company of Jean-Christophe Denis, Matthew Edmonds, Wolf-Rüdiger Hannes, Jaroslaw Jarzynka, Nadezda Kotova, Daniel Maldonado-Mundo, Natalia and Peter McDonald, Michael Merkl, Stefan Schumacher, and many others, who always created a very pleasant and productive atmosphere at the physics department.

I am much obliged to Prof Andy Mackenzie and the other members of the administrative board for the opportunity to join the Scottish Doctoral Training Centre in Condensed Matter Physics. I benefitted greatly from the inspiring interactions with the other students of the centre and learned immensely from our joint participation in courses and

schools and would like to thank them for that.

The financial support from the Engineering and Physical Research Council and the Scottish Doctoral Training Centre in Condensed Matter Physics is gratefully acknowledged. Specifically, I am thankful for having had the opportunity to go to many instructive schools and stimulating conferences.

I would like to thank my friends Jean-Christoph Denis, Matthew Edmonds, Wolf-Rüdiger Hannes, Oliver and Jenny Henrich, Peter McDonald and my teammates from the ECC for making the life in Edinburgh even more enjoyable. Special thanks go to my flatmates Jana Werner, Giuseppe Pellegrini Masini, Adam Filipowski, and Shilong Quian.

Mein größter Dank gilt meiner Familie, meinen Eltern Rosemarie und Hansjörg Gattenlöhner, sowie meinen Geschwistern Stefan, Simone und Sandra, die mich mit unerschöpflicher Geduld unterstützt und mir stets einen großen Rückhalt gegeben haben.

Contents

List of publications

Part of the work presented in this thesis has been published in the form of articles in peer-reviewed journals:

1. S. Gattenlöhner, W. Belzig, and M. Titov, *Dirac-Kronig-Penney model for strain-engineered graphene*, Physical Review B **82**, 155417 (2010). [see Chapter 4]

2. S. Gattenlöhner, W. R. Hannes, P. Ostrovsky, I. V. Gornyi, A. D. Mirlin, and M. Titov, *Quantum Hall Criticality and Localization in Graphene with Short-Range Impurities at the Dirac Point*, Physical Review Letters **112**, 026802 (2014). [see Chapter 5]

1 Introduction

> It is an interesting intellectual game to compress an essence of a science, or a given scientific field, to a single sentence. For natural sciences in general, this sentence would probably read: *Everything consists of atoms*. [...] If we try to play the same game of putting the essence of quantum transport into one sentence, it would read: *It is not important whether a nanostructure consists of atoms.* The research in quantum transport focuses on the properties and behaviour regimes of nanostructures, which do not immediately depend on the material and atomic composition of the structure, and which cannot be explained by classical (that is, non-quantum) physics.
>
> Y. Nazarov and Y. Blanter [1]

The experimental realisation of graphene [2] and topological insulators [3] have arguably been the most influential discoveries in the field of quantum transport during the last decade. If one tried to condense into a single sentence what is common to these developments, it would probably read: *In some materials, quantum transport comes with an extra twist.* In this introduction, we highlight some of the twists displayed by graphene and discuss their role in the research problems addressed in this thesis.

Graphene – a one-atom-thick sheet of carbon atoms arranged in a honeycomb lattice – has been used as a theoretical construct to describe other carbon allotropes like graphite [4] or carbon nanotubes (see [5] for a review) for many decades. It was assumed not to exist in the free state, for there are several theoretical arguments indicating that any strictly two-dimensional crystal would be thermodynamically unstable [6, 7, 8]. Consequently, it came as a surprise, when in 2004, the group around Andre Geim and Konstantin Novoselov was able to produce the two-dimensional atomic crystal of graphene [2].

Graphene can be characterised as a gapless semiconductor (or a semi-metal of zero band overlap) with a linear dispersion and a vanishing density of states near the points where the valance and conduction band touch [4]; this happens at the high-symmetry points $\boldsymbol{K}$ and $\boldsymbol{K}'$ in the corners of the first Brillouin zone which are often referred to as 'valleys'.

The energetically low-lying electronic excitations can be described by envelope functions to the four zero-energy states at the critical points (in each valley, there are two states). These envelope functions can be arranged in a four-spinor obeying the Dirac-Weyl equation [9, 10] such that the electronic excitations in graphene behave like massless, chiral fermions. One of the first experimental verifications of this 'relativistic' behaviour was the measurement of a non-standard integer quantum Hall effect in graphene [11, 12]. Graphene's spin equivalent, called pseudo-spin, is related to the fact that the honeycomb lattice has a two-atomic unit cell; the cases 'pseudo-spin up' and 'pseudo-spin down', for instance, correspond to situations where the electron is inhabiting only one sublattice.

A large part of the interest in graphene originates from the combination of its relative simplicity (concerning production and theoretical modelling) on the one hand and the peculiarity of its electronic properties on the other. Soon after its discovery, this combination raised hopes that novel phenomena in the area of fundamental physics can be discovered in graphene, but also suggested that certain theoretical predictions and thought experiments, which could not be experimentally observed in their original contexts, can be realised in graphene.

The first example of the latter scenario was the idea [13] that the transport properties of graphene should show signatures of the Klein 'paradox'. The Klein 'paradox' has already been conjectured in the very early days of quantum mechanics [14] but could not be observed in the field of high energy physics. A few years after the discovery by Geim and Novoselov, several groups were indeed able to show the impact of Klein tunnelling[1] on their transport measurements in graphene [15, 16, 17]. References [18] and [19] thoroughly review the physics of Klein tunnelling in graphene.

The most recent example of such a well known but yet unmeasured effect was seen in the first experimental observation [20, 21, 22] of the 'Hofstadter butterfly', the fractal energy spectrum of electrons exposed to both a quantising magnetic field and a periodic electrostatic potential [23]. To produce such a periodic potential is comparatively simple in graphene by taking advantage of the Moiré effect, depositing the sample on a boron nitride substrate with an almost commensurate hexagonal lattice structure.

Electron transport in *undoped* graphene proved unusual even without external potentials or disorder. The current is carried by evanescent modes leading to a finite minimal conductivity in spite of the vanishing density of states and there are surprising similarities with transport in diffusive conductors [24, 25]. The Fano factor, for instance, which is given by $F = 1/3$ in diffusive wires, has been predicted to have the same value for

[1] Note that there is actually no paradox and the more appropriate word 'tunnelling' has to be understood in the sense of inter-band tunnelling as opposed to tunnelling that involves evanescent waves.

graphene samples with a large aspect ratio [25], which has indeed been measured [26].

Another part of the enormous interest in graphene is due to its favourable characteristics as a potential material for applications. In many of its properties, graphene outperforms any other material such that the non-scientific press started to habitually call it the 'miracle material'. The 'Roadmap to graphene' [27], which played an important role in the successful bid for the Future & Emerging Technologies Flagship grant, highlights the following advantageous material properties:

- The crystal quality of graphene is extremely high with a room temperature mobility of $2.5 \times 10^5\,\mathrm{cm^2\,V^{-1}\,s^{-1}}$ [28].
- It is mechanically very robust with a Young's modulus of 1TPa and an intrinsic strength of 130 GPa [29].
- Graphene has a very large thermal conductivity exceeding a value of $3\,000\,\mathrm{W\,mK^{-1}}$ [30].
- It features an optical absorption of exactly $\pi\alpha \approx 2.3\%$ in the infrared limit [31] (α being the fine structure constant).
- Graphene is fully impermeable to gases [32],
- and sustains high densities of electric current, which can be up to a million times higher than in copper [33].

Based on these properties, the roadmap article suggests applications for graphene in areas as diverse as electronics, photonics, as composite material/paint/coating, for energy generation and storage, in metrology, for sensors, and in biology.

There are also challenges set by the peculiar properties of graphene, however. One of these challenges is the absence of a band gap which makes it hard to build standard electronic devices, such as field-effect transistors, in the usual way. Several ways of introducing a band gap to graphene have been proposed, but have the downside of introducing disorder or edge roughness, thereby decreasing the mobility of electrons in the system. There has been a promising suggestion to use strains to alter the band structure of graphene without destroying its other advantageous properties [34]. On the level of the Dirac equation, the straining of graphene leads to an additional vector potential (as was first discussed for carbon nanotubes [35]). The approach proposed in Ref. [34] aims to induce such vector potentials in a very controlled way by patterning the substrate rather than manipulating the graphene sheet itself. Graphene samples with a periodic modulation in strain have already been realised experimentally [36, 37, 38, 39].

Motivated by the above proposal, **Chapter 4** investigates the Dirac-Kronig-Penney model, which describes the phase-coherent transport in clean monolayer samples with a

one-dimensional periodic modulation of the vector and the electrostatic potential. The effect of one-dimensional (vector) potentials on the Dirac equation has been intensively studied by many groups [40, 41, 42, 43, 44, 45, 46, 47, 48, 49, 50, 51] with a focus on the changed band structure, while the present work investigates the transport properties directly by calculating, among other things, the conductivity and the shot noise in a two terminal setup. We demonstrate that periodic strains can induce large pseudo-gaps and suppress charge transport in the direction of the strain modulation, while the effect for periodic electrostatic potentials is weakened by Klein tunnelling.

Another intense area of graphene research investigates the physics of Anderson localisation [52] and its precursors. Early transport measurements showed a strong suppression (or even absence) of the weak-localisation magneto-resistance in graphene [53]. Weak localisation [54] is the effect that the resistivity is increased, relative to classical expectations, by the quantum mechanical interference of different scattering paths. The largest contribution to this increased resistivity is due to pairs of returning trajectories that can be transversed either clockwise or counterclockwise and, in the presence of time-reversal symmetry, interfere constructively; a magnetic field breaking the time-reversal symmetry removes this largest contribution and consequently leads to a smaller resistivity, an effect called negative magneto-resistance. In graphene with smooth disorder and negligible trigonal warping (the same holds for carbon nanotubes, where this phenomenon was first discussed [55]), the time-reversed paths pick up a relative Berry phase of π turning the constructive interference into a destructive one, the quantum mechanical increase of the resistivity into a decrease, and the negative magneto-resistance into a positive one. As was demonstrated later theoretically [56] and experimentally [57], both weak anti-localisation and weak localisation effects can be realised in graphene depending on the nature of the dominant scattering mechanism (intra-valley or inter-valley scattering, respectively).

These early findings suggested that while graphene behaves like a typical two-dimensional electronic system when the disorder does not preserve any of this material's special symmetries, a rich variety of localisation phenomena can be expected when certain symmetries are preserved. This potential richness can be quantified in the following way: when perturbed by suitable disorder, undoped graphene may realise any of ten symmetry classes [58] of the exhaustive Altand-Zirnbauer classification scheme [59, 60]. This makes graphene an ideal experimental and theoretical model system to study the physics of Anderson localisation in two dimensions.

Motivated by the above, **Chapter 5** considers transport in disordered graphene at the Dirac point, restricting ourselves to two types of short-range scatterers: adatoms

that mix the valleys and 'scalar' impurities that do not mix them.[2] The unfolded scattering formalism [61, 62] is used to provide an analytic expression for the conductivity in the presence of disorder, which is then numerically averaged over many impurity configurations. Compared to an earlier study of disordered graphene that employed the unfolded scattering formalism [62], the current work also allows for non-resonant impurities and non-zero magnetic fields perpendicular to the sample. The additional freedom to vary the magnetic field and the impurity strength enables us to explore six of the ten symmetry classes of the Altland-Zirnbauer classification scheme.

In the absence of a magnetic field, the results indicate that adatom disorder, which breaks the chiral symmetry of the Dirac Hamiltonian, leads to localisation but also that the localisation length diverges when the adatom strength approaches the vacancy limit of an infinite scattering length (in which case the chiral symmetry is reinstalled). While this is more or less expected in view of Ref. [62], it is surprising that the scattering length needs to be exponentially large for this behaviour to be observed. As the scattering length of a vacancy ceases to be infinite away from the Dirac point, this sheds some light on the question why numerical works, such as [63], see localisation in the presence of vacancies even when the sample doping is extremely close to zero.

At very strong magnetic fields, the Dirac point conductivity is found to take its ballistic value of $4e^2/\pi h$, independent of the impurity configuration. Although the details of this surprising phenomenon are not fully understood, it is likely that an explanation includes the following ingredients: the fact that magnetic fields are unable to change the Dirac point conductivity in *clean* graphene [64, in particular Sec. V.C], the observation that the Dirac point conductivity is typically carried by only a small number of modes (see Section 3.3), and the finding that s-wave scatterers are unable to fully lift the degeneracy of a Landau level when the flux per impurity is large compared to the flux quantum [65, 66].

For weaker magnetic fields, a rich scaling flow is observed which is consistent with the theory [67] proposed for the integer quantum Hall effect in graphene.

Schelter et al. [68] demonstrated that the Dirac point conductivity of a graphene sample with two vacancies (one located on the A site of the unit cell $\boldsymbol{R}_1$, the other on the B site of the unit cell at $\boldsymbol{R}_2$) crucially depends on the Bloch phases $e^{i\boldsymbol{K}\boldsymbol{R}_{1,2}} \in \left\{e^{2\pi i c/3} | c = 0, \pm 1\right\}$ and called c the colour index of the vacancy site.

[2] We use the term 'adatom' for any impurity that, on the tight-binding level, would be modelled as an isolated on-site potential (i.e. we do not study other commonly realised adatom types like those located in the middle of the carbon-carbon bonds or in the hexagon centres) whereas scalar potentials are smooth on the length scale of the lattice constant and thus appear as diagonal matrices in pseudospin⊗valley-space on the level of the Dirac-description of graphene.

The vacancy colour remains to be important in disordered systems with many vacancies. Ostrovsky et al. [62] found that when the numbers of vacancies on the two sublattices are equal and become sufficiently large, the Dirac point conductivity saturates at a constant value that depends on whether the vacancy sites are all of the same colour or not: when the colours are random, the configuration-averaged conductivity remains roughly at its ballistic value, while for the single colour case, saturation happens at a conductivity that is roughly twice as large (the concrete value depends the on the lattice orientation). The physical origin of this behaviour is not yet understood.

The concept of colours also applies to adatoms and it seems likely that the freedom to vary the adatom strength helps to develop a deeper understanding of the problem. To this end, **Chapter 6** presents work in progress studying the transport properties of graphene with many randomly placed single-colour adatoms. We use the unfolded scattering formalism and the software package Kwant [69] to obtain the conductivity for a single impurity configuration and average over many such configurations. Surprisingly, a rise of the conductivity is observed when increasing the density of single-colour adatoms although localisation was seen in the corresponding the random-colour case (see Chapter 5).

The main chapters 4, 5, and 6 are preceded by two technical ones: **Chapter 2** discusses the basic electronic properties of graphene with an emphasis on its continuum description within the effective-mass approximation. **Chapter 3** is an introduction to quantum transport in graphene and has a dual purpose: first, it introduces the methods and the notation used in the present thesis; second, by applying these methods to clean graphene, it allows us to discuss some of those physical phenomena in their most simple form that will be relevant to the more complicated systems studied in later chapters.

References of Chapter 1

[1] Nazarov, Y. V. & Blanter, Y. M. *Quantum Transport.* Introduction to Nanoscience (Cambridge University Press, Cambridge, 2009).

[2] Novoselov, K. S. *et al.* Electric field effect in atomically thin carbon films. *Science* **306**, 666–669 (2004).

[3] Konig, M. *et al.* Quantum Spin Hall Insulator State in HgTe Quantum Wells. *Science* **318**, 766–770 (2007).

[4] Wallace, P. The Band Theory of Graphite. *Physical Review* **71**, 622–634 (1947).

[5] Ando, T. Theory of Electronic States and Transport in Carbon Nanotubes. *Journal of the Physical Society of Japan* **74**, 777–817 (2005).

[6] Peierls, R. Quelques propriétés typiques des corps solides. *Annales de l'institut Henri Poincaré* **5**, 177–222 (1935).

[7] Landau, L. D. On the theory of phase transitions. I. *Zh. Eksp. Teor. Fiz.* 19–32 (1937).

[8] Mermin, N. Crystalline Order in Two Dimensions. *Physical Review* **176**, 250–254 (1968).

[9] Semenoff, G. W. Condensed-matter simulation of a three-dimensional anomaly. *Physical Review Letters* **53**, 2449–2452 (1984).

[10] DiVincenzo, D. P. & Mele, E. J. Self-consistent effective-mass theory for intralayer screening in graphite intercalation compounds. *Physical Review B* **29**, 1685 (1984).

[11] Novoselov, K. S. *et al.* Two-dimensional gas of massless Dirac fermions in graphene. *Nature* **438**, 197–200 (2005).

[12] Zhang, Y., Tan, Y.-W., Stormer, H. L. & Kim, P. Experimental observation of the quantum Hall effect and Berry's phase in graphene. *Nature* **438**, 201–204 (2005).

[13] Katsnelson, M. I., Novoselov, K. S. & Geim, A. K. Chiral tunnelling and the Klein paradox in graphene. *Nature Physics* **2**, 620–625 (2006).

[14] Klein, O. Die Reflexion von Elektronen an einem Potentialsprung nach der relativistischen Dynamik von Dirac. *Zeitschrift für Physik* **53**, 157–165 (1929).

[15] Huard, B. *et al.* Transport measurements across a tunable potential barrier in graphene. *Physical Review Letters* **98**, 236803 (2007).

[16] Gorbachev, R. V., Mayorov, A. S., Savchenko, A. K., Horsell, D. W. & Guinea, F. Conductance of pnp Graphene Structures with "Air-Bridge" Top Gates. *Nano Letters* **8**, 1995–1999 (2008).

[17] Young, A. F. & Kim, P. Quantum interference and Klein tunnelling in graphene heterojunctions. *Nature Physics* **5**, 222–226 (2009).

[18] Beenakker, C. W. J. Colloquium: Andreev reflection and Klein tunneling in graphene. *Reviews of Modern Physics* **80**, 1337 (2008).

[19] Allain, P. & Fuchs, J.-N. Klein tunneling in graphene: optics with massless electrons. *European Physical Journal B* (2011).

[20] Ponomarenko, L. A. *et al.* Cloning of Dirac fermions in graphene superlattices. *Nature* **497**, 594–597 (2013).

[21] Dean, C. R. *et al.* Hofstadter's butterfly and the fractal quantum Hall effect in moiré superlattices. *Nature* **497**, 598–602 (2013).

[22] Hunt, B. *et al.* Massive Dirac Fermions and Hofstadter Butterfly in a van der Waals Heterostructure. *Science* **340**, 1427–1430 (2013).

[23] Hofstadter, D. R. Energy levels and wave functions of Bloch electrons in rational and irrational magnetic fields. *Physical Review B* **14**, 2239 (1976).

[24] Katsnelson, M. I. Zitterbewegung, chirality, and minimal conductivity in graphene. *European Physical Journal B* **51**, 157–160 (2006).

[25] Tworzydło, J., Trauzettel, B., Titov, M., Rycerz, A. & Beenakker, C. W. J. Sub-Poissonian Shot Noise in Graphene. *Physical Review Letters* **96** (2006).

[26] Danneau, R. *et al.* Shot noise in ballistic graphene. *Physical Review Letters* **100**, 196802 (2008).

[27] Novoselov, K. S. *et al.* A roadmap for graphene. *Nature* **490**, 192–200 (2012).

[28] Mayorov, A. S. *et al.* Micrometer-Scale Ballistic Transport in Encapsulated Graphene at Room Temperature. *Nano Letters* **11**, 2396–2399 (2011).

[29] Lee, C., Wei, X., Kysar, J. W. & Hone, J. Measurement of the Elastic Properties and Intrinsic Strength of Monolayer Graphene. *Science* **321**, 385–388 (2008).

[30] Balandin, A. A. Thermal properties of graphene and nanostructured carbon materials. *Nature Materials* **10**, 569–581 (2011).

[31] Nair, R. R. *et al.* Fine Structure Constant Defines Visual Transparency of Graphene. *Science* **320**, 1308–1308 (2008).

[32] Bunch, J. S. *et al.* Impermeable Atomic Membranes from Graphene Sheets. *Nano Letters* **8**, 2458–2462 (2008).

[33] Moser, J., Barreiro, A. & Bachtold, A. Current-induced cleaning of graphene. *Applied Physics Letters* **91**, 163513 (2007).

[34] Pereira, V. M. & Neto, A. C. Strain engineering of graphene's electronic structure. *Physical Review Letters* **103**, 046801 (2009).

[35] Suzuura, H. & Ando, T. Phonons and electron-phonon scattering in carbon nanotubes. *Physical Review B* **65**, 235412 (2002).

[36] Bao, W. *et al.* Controlled ripple texturing of suspended graphene and ultrathin graphite membranes. *Nature Nanotechnology* **4**, 562–566 (2009).

[37] Pletikosić, I. *et al.* Dirac cones and minigaps for graphene on Ir (111). *Physical Review Letters* **102**, 056808 (2009).

[38] Vazquez de Parga, A. L. *et al.* Periodically Rippled Graphene: Growth and Spatially Resolved Electronic Structure. *Physical Review Letters* (2008).

[39] Teague, M. L., Lai, A. P., Velasco, J. & Hughes, C. R. Evidence for Strain-Induced Local Conductance Modulations in Single-Layer Graphene. *Nano Letters* 2542–2546 (2009).

[40] Park, C.-H., Son, Y.-W., Yang, L., Cohen, M. L. & Louie, S. G. Electron beam supercollimation in graphene superlattices. *Nano Letters* **8**, 2920–2924 (2008).

[41] Park, C.-H., Son, Y.-W., Yang, L., Cohen, M. L. & Louie, S. G. Landau levels and quantum Hall effect in graphene superlattices. *Physical Review Letters* **103**, 046808 (2009).

[42] Park, C.-H., Yang, L., Son, Y.-W., Cohen, M. L. & Louie, S. G. Anisotropic behaviours of massless Dirac fermions in graphene under periodic potentials. *Nature Physics* **4**, 213–217 (2008).

[43] Dell'Anna, L. & De Martino, A. Multiple magnetic barriers in graphene. *Physical Review B* **79**, 045420 (2009).

[44] Snyman, I. Gapped state of a carbon monolayer in periodic magnetic and electric fields. *Physical Review B* **80**, 054303 (2009).

[45] Brey, L. & Fertig, H. A. Emerging zero modes for graphene in a periodic potential. *Physical Review Letters* **103**, 046809 (2009).

[46] Esmailpour, M., Esmailpour, A., Asgari, R., Elahi, M. & Tabar, M. R. R. Effect of a gap opening on the conductance of graphene superlattices. *Solid State Communications* **150**, 655–659 (2010).

[47] Wang, L.-G. & Zhu, S.-Y. Electronic band gaps and transport properties in graphene superlattices with one-dimensional periodic potentials of square barriers. *Physical Review B* **81**, 205444 (2010).

[48] Tan, L. Z., Park, C.-H. & Louie, S. G. Graphene Dirac fermions in one-dimensional inhomogeneous field profiles: Transforming magnetic to electric field. *Physical Review B* **81**, 195426 (2010).

[49] Park, C. H., Tan, L. Z. & Louie, S. G. Theory of the electronic and transport properties of graphene under a periodic electric or magnetic field. *Physica E: Low-dimensional Systems* (2011).

[50] Novikov, D. S. Electron properties of carbon nanotubes in a periodic potential. *Physical Review B* **72**, 235428 (2005).

[51] Novikov, D. S. Devil's staircase of incompressible electron states in a nanotube. *Physical Review Letters* **95**, 066401 (2005).

[52] Anderson, P. W. Absence of diffusion in certain random lattices. *Physical Review* (1958).

[53] Morozov, S. V. *et al.* Strong suppression of weak localization in graphene. *Physical Review Letters* **97**, 016801 (2006).

[54] Altshuler, B. L., Khmel'nitskii, D. E., Larkin, A. I. & Lee, P. Magnetoresistance and Hall effect in a disordered two-dimensional electron gas. *Physical Review B* **22**, 5142 (1980).

[55] Ando, T., Nakanishi, T. & Saito, R. Berry's Phase and Absence of Back Scattering in Carbon Nanotubes. *Journal of the Physical Society of Japan* **67**, 2857–2862 (1998).

[56] McCann, E. *et al.* Weak-Localization Magnetoresistance and Valley Symmetry in Graphene. *Physical Review Letters* **97** (2006).

[57] Tikhonenko, F. V., Kozikov, A. A., Savchenko, A. K. & Gorbachev, R. V. Transition between electron localization and antilocalization in graphene. *Physical Review Letters* **103**, 226801 (2009).

[58] Mirlin, A. D., Evers, F., Gornyi, I. V. & Ostrovsky, P. Anderson transitions: Criticality, symmetries and topologies. *International Journal Of Modern Physics B* **24**, 1577–1620 (2010).

[59] Zirnbauer, M. R. Riemannian symmetric superspaces and their origin in random matrix theory. *J. Math. Phys.* **37**, 4986 (1996).

[60] Altland, A. & Zirnbauer, M. R. Nonstandard symmetry classes in mesoscopic normal-superconducting hybrid structures. *Physical Review B* **55**, 1142–1161 (1997).

[61] Titov, M., Ostrovsky, P., Gornyi, I. V., Schuessler, A. & Mirlin, A. D. Charge Transport in Graphene with Resonant Scatterers. *Physical Review Letters* **104** (2010).

[62] Ostrovsky, P., Titov, M., Bera, S., Gornyi, I. V. & Mirlin, A. D. Diffusion and Criticality in Undoped Graphene with Resonant Scatterers. *Physical Review Letters* **105**, 266803 (2010).

[63] Cresti, A., Ortmann, F., Louvet, T., Van Tuan, D. & Roche, S. Broken Symmetries, Zero-Energy Modes, and Quantum Transport in Disordered Graphene: From Supermetallic to Insulating Regimes. *Physical Review Letters* **110**, 196601 (2013).

[64] Schuessler, A., Ostrovsky, P., Gornyi, I. V. & Mirlin, A. D. Analytic theory of ballistic transport in disordered graphene. *Physical Review B* **79**, 075405 (2009).

[65] Brezin, E., Gross, D. & Itzykson, C. Density of states in the presence of a strong magnetic field and random impurities. *Nuclear Physics B* **235**, 24–44 (1984).

[66] Gredeskul, S., Zusman, M., Avishai, Y. & Azbel, M. Electron in two-dimensional system with point scatterers and magnetic field. *IMA VOLUMES IN MATHEMATICS AND ITS APPLICATIONS* **96**, 95–142 (1998).

[67] Ostrovsky, P., Gornyi, I. V. & Mirlin, A. D. Theory of anomalous quantum Hall effects in graphene. *Physical Review B* **77**, 195430 (2008).

[68] Schelter, J., Ostrovsky, P., Gornyi, I. V., Trauzettel, B. & Titov, M. Color-dependent conductance of graphene with adatoms. *Physical Review Letters* **106**, 166806 (2011).

[69] Groth, C. W., Wimmer, M., Akhmerov, A. R. & Waintal, X. Kwant: a software package for quantum transport. *New Journal of Physics* **16**, 063065 (2014).

2 Electronic properties of single-layer graphene

In this chapter, we review the basic electronic properties of graphene. As there is a large quantity of good review articles and text books available on this topic (for instance Ref. [1] and Ref. [2], to name just two from each category), we restrict ourselves to a discussion of graphene's peculiar bandstructure and its effective-mass description by means of the Dirac-Weyl equation.

2.1 The bandstructure of graphene

We begin by discussing the energy dispersion of conduction electrons in graphene by means of a tight binding model (as was first done by P. R. Wallace in 1947, see Ref. [3]). The idea behind this model is to assume that the electronic states are well localised on a periodic lattice and that the only dynamics possible for the electrons is to jump between these lattice sites. The main input to this theory is the lattice structure of the system under consideration, while our ignorance about other microscopic details is dumped into the hopping energies associated with the jumping processes. We therefore discuss the lattice structure of graphene, next.

Graphene is a two-dimensional allotrope of carbon, where sp^2-hybridised carbon atoms are connected by strong σ-bonds thereby creating a honeycomb lattice. The remaining p_z-orbitals overlap only weakly and form the band of mobile electrons we intend to describe by the tight-binding model. To construct the honeycomb lattice, we introduce a two-atomic unit cell and the two basis vectors

$$\boldsymbol{a}_1 = \frac{a}{2}\begin{pmatrix} 3 \\ \sqrt{3} \end{pmatrix}, \qquad \boldsymbol{a}_2 = \frac{a}{2}\begin{pmatrix} 3 \\ -\sqrt{3} \end{pmatrix} \tag{2.1}$$

of the hexagonal lattice, where $a \approx 1.42\,\text{Å}$ (see Figure 2.1a).

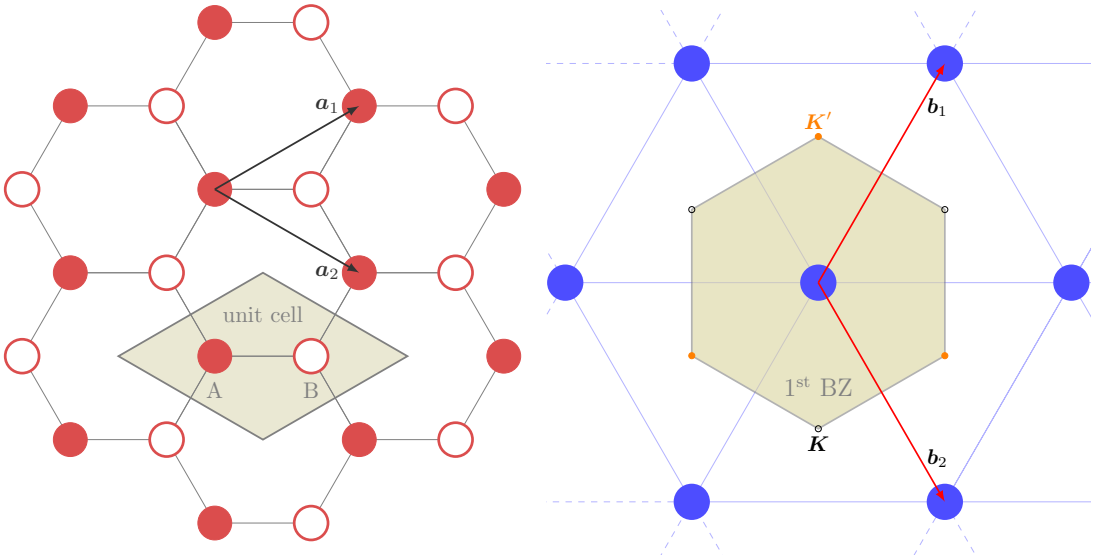

(a) coordinate space (b) reciprocal space

Figure 2.1: The lattice structure of graphene in coordinate space (a) and reciprocal space (b). The unit cells of the direct and the reciprocal lattice are shown in yellow and have areas $A_{\text{UC}} = \sqrt{27}a^2/2$ and $A_{\text{BZ}} = (2\pi)^2/A_{\text{UC}}$, respectively.

To a first approximation, we will only take into account hopping between nearest neighbours such that the tight-binding Hamiltonian is of the form

$$H = -t \sum_{\langle ij \rangle, \sigma} a^\dagger_{i\sigma} b_{j\sigma} + \text{h.c.}, \tag{2.2}$$

where $a^\dagger_{i\sigma}$ ($b^\dagger_{i\sigma}$) is the creation operator of an electron on sublattice A (B), located in unit cell $\boldsymbol{R}_i = m\boldsymbol{a}_1 + n\boldsymbol{a}_2, i = (m, n)$ and having the spin $\sigma \in \{\uparrow, \downarrow\}$; $t \approx 2.7\text{eV}$ is the nearest-neighbour hopping energy and h.c. denotes Hermitian conjugation. The symbol $\langle ij \rangle$ means that the sum is over nearest neighbour sites only (with the notation introduced in Fig. 2.1a, we would have $\boldsymbol{R}_i - \boldsymbol{R}_j \in \{\boldsymbol{0}, -\boldsymbol{a}_1, -\boldsymbol{a}_2\}$ for nearest neighbours i and j).

In (pseudo-)momentum representation, Hamiltonian (2.2) can written as

$$H = \sum_{\boldsymbol{k}, \sigma} \begin{pmatrix} a^\dagger_{\boldsymbol{k}\sigma} & b^\dagger_{\boldsymbol{k}\sigma} \end{pmatrix} \begin{pmatrix} 0 & -tf(\boldsymbol{k}) \\ -tf(\boldsymbol{k})^* & 0 \end{pmatrix} \begin{pmatrix} a_{\boldsymbol{k}\sigma} \\ b_{\boldsymbol{k}\sigma} \end{pmatrix}, \tag{2.3}$$

where $f(\boldsymbol{k}) = 1 + e^{-i\boldsymbol{k}\boldsymbol{a}_1} + e^{-i\boldsymbol{k}\boldsymbol{a}_2}$. Here, $\boldsymbol{k}$ denotes a vector in the first Brillouin zone

(see Fig. 2.1b) which means that $\boldsymbol{k} = \tilde{k}_1\boldsymbol{b}_1 + \tilde{k}_2\boldsymbol{b}_2$, where

$$\boldsymbol{b}_1 = \frac{2\pi}{3a}\begin{pmatrix}1\\ \sqrt{3}\end{pmatrix}, \qquad \boldsymbol{b}_2 = \frac{2\pi}{3a}\begin{pmatrix}1\\ -\sqrt{3}\end{pmatrix} \tag{2.4}$$

are the basis vectors of the reciprocal lattice and $\tilde{k}_i \in [-1/2, 1/2]$. The Hamiltonian (2.3) can easily be diagonalised yielding the dispersion relation [3]

$$\varepsilon(\boldsymbol{k}) = \pm t|f(\boldsymbol{k})| = 2\cos\left(\sqrt{3}k_y a\right) + 4\cos\left((\sqrt{3}/2)k_y a\right)\cos\left((3/2)k_x a\right). \tag{2.5}$$

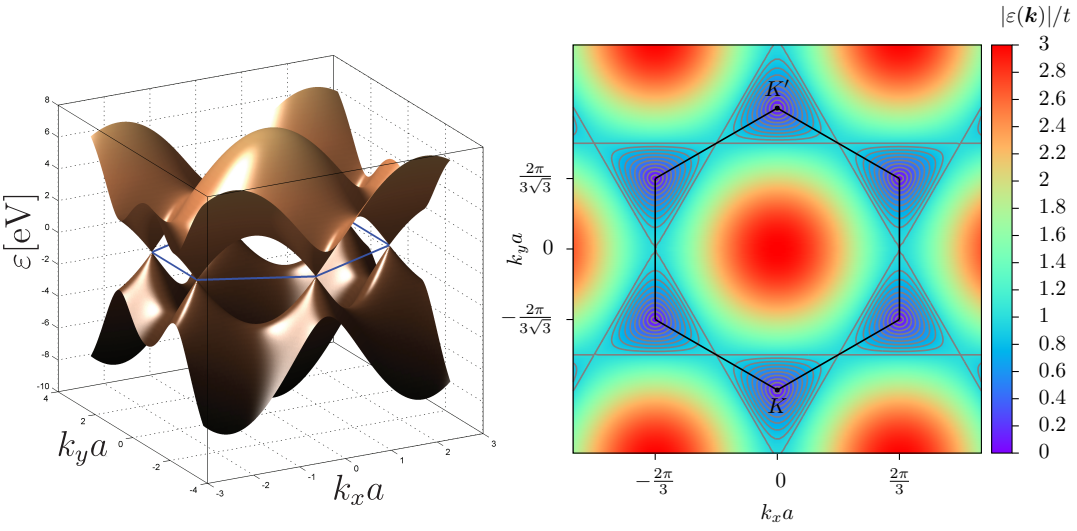

(a) (b)

Figure 2.2: Spectrum of the tight binding Hamiltonian (2.2) according to Eq. (2.5): as a 3D plot (a) and as a contour plot (b).

The above energy spectrum consists of two bands, where the lower one is usually called the π^*-band and the upper one the π-band. The π^*-band and the π-band touch each other at six points in the $\varepsilon = 0$-plane (where only two of these are inequivalent, as the others differ only by a reciprocal lattice vector). These intersections coincide with the corners of the first Brillouin zone, which are called Dirac points, for reasons that will

become clear later. We denote them as[1]

$$\boldsymbol{K} = \left(0, -\frac{4\pi}{3\sqrt{3}a}\right), \qquad \boldsymbol{K}' = \left(0, \frac{4\pi}{3\sqrt{3}a}\right). \tag{2.6}$$

We can easily convince ourselves that $\varepsilon = 0$ is the Fermi energy of the given system (leading to a point-like Fermi surface). To understand this, imagine a graphene crystal consisting of N unit cells. Due to the finiteness of the sample, $\boldsymbol{k}$ becomes discrete with N allowed $\boldsymbol{k}$ vectors in the first Brillouin zone. There are two electron states for each allowed $\boldsymbol{k}$ vector in each energy band, as a consequence of the spin degeneracy and the Pauli principle. Since two carbon atoms sit in each unit cell, we have to distribute a number of $2N$ p_z-electrons, what exactly fills the lower π^*-band in the ground state, yielding a Fermi energy of $\varepsilon_F = 0$.

In the vicinity of the Dirac-points (i.e. for electrons near the Fermi energy) the band structure possesses a cone-like form. To investigate this quantitatively, we now write $\boldsymbol{k} = \boldsymbol{K} + \boldsymbol{p}$ or $\boldsymbol{k} = \boldsymbol{K}' + \boldsymbol{p}$, with $\boldsymbol{p} = p(\cos\theta_{\boldsymbol{p}}, \sin\theta_{\boldsymbol{p}})$, and expand Eq. (2.5) up to quadratic order in p. This yields [4]

$$\varepsilon(\boldsymbol{K} + \boldsymbol{p}) = \pm\frac{3at}{2}p \mp \frac{3}{8}ta^2\sin(3\theta_{\boldsymbol{q}})p^2 + \mathcal{O}(p^3), \tag{2.7a}$$

$$\varepsilon(\boldsymbol{K}' + \boldsymbol{p}) = \pm\frac{3at}{2}p \pm \frac{3}{8}ta^2\sin(3\theta_{\boldsymbol{p}})p^2 + \mathcal{O}(p^3). \tag{2.7b}$$

Up to linear order in p, we find around both $\boldsymbol{K}$ and $\boldsymbol{K}'$

$$\varepsilon(\boldsymbol{p}) = \pm\hbar v p, \tag{2.8}$$

what is equivalent to the energy spectrum of a massless relativistic particle with an effective speed of light given by the Fermi velocity

$$v \equiv \frac{3at}{2\hbar} \approx 1 \times 10^6\,\mathrm{m/s} \approx \frac{1}{300}c. \tag{2.9}$$

We want to stress the following properties of this cone-like dispersion:

- (2.8) is isotropic, i.e. the dispersion of the low-lying excitations does not reflect that there is a lattice, in the sense, that the spontaneously broken rotational symmetry

[1] This choice of Dirac points has the advantage that $\boldsymbol{K}' = -\boldsymbol{K}$ allowing for more compact notations than with other choices.

of the crystallised system (down to a sixfold symmetry) is only apparent in higher than linear order in $\boldsymbol{p}$.

- There exists a particle-hole symmetry, in the sense that $\varepsilon(\boldsymbol{p})$ is mirror symmetric with respect to the plane given by $\varepsilon = 0$ (this statement is trivial in the case where only nearest-neighbour hopping is taken into account but continues to hold close to the Dirac points even when further hoppings are included).

The quadratic term in Eq. (2.7) breaks the isotropy of the dispersion. One can see this effect, often referred to as 'trigonal warping', most clearly in the curves of constant energy around the Dirac points (Fig. 2.2(b)): very close to $\boldsymbol{K}$ and $\boldsymbol{K}'$ they start out as circles and become more and more triangular upon increasing p.

In this thesis, we are exclusively concerned with the physics very close to the Dirac points featuring a conic dispersion.

2.2 The effective Hamiltonian around the Dirac points

In the previous section, the dispersion of graphene was discussed and it was emphasised that close to the Fermi energy it coincides with the dispersion of massless relativistic particles. As References [5, 6] demonstrated roughly twenty years before the relativistic Quantum Hall effect in graphene was seen in experiments (see [7, 8]), this analogy goes even further in that the energetically low-lying electronic excitations in graphene can be described by a four-component spinor obeying the Dirac-Weyl equation. In this section we will elaborate on this statement.

The starting point of an effective treatment of the energetically low-lying excitations is the tight-binding Hamiltonian in momentum space, Eq. (2.3), and the observation that the Fermi surface is given by the two inequivalent Dirac points $\boldsymbol{K}$ and $\boldsymbol{K}'$. It is therefore sensible to introduce an effective Hamiltonian that only acts on states of momenta of the form $\pm\boldsymbol{K} + \boldsymbol{p}$ with $|\boldsymbol{p}|$ sufficiently small. Taking advantage of the fact that

$$f(\pm\boldsymbol{K} + \boldsymbol{p}) = \frac{3ai}{2}(p_x \mp ip_y) + \mathcal{O}(\boldsymbol{p}^2), \tag{2.10}$$

we can write the effective Hamiltonian as

$$H \approx \sum_{\boldsymbol{p},\sigma} \tilde{\Psi}(\boldsymbol{p})^\dagger \tilde{\mathcal{H}}(\boldsymbol{p}) \tilde{\Psi}(\boldsymbol{p}), \tag{2.11a}$$

where $\tilde{\Psi}(\boldsymbol{p}) = \left(a_{\boldsymbol{K}+\boldsymbol{p},\sigma}, b_{\boldsymbol{K}+\boldsymbol{p},\sigma}, a_{\boldsymbol{K}'+\boldsymbol{p},\sigma}, b_{\boldsymbol{K}'+\boldsymbol{p},\sigma}\right)^T$ and

$$\tilde{\mathcal{H}} = \begin{pmatrix} 0 & -iv(p_x - ip_y) & 0 & 0 \\ iv(p_x + ip_y) & 0 & 0 & 0 \\ 0 & 0 & 0 & -iv(p_x + ip_y) \\ 0 & 0 & iv(p_x - ip_y) & 0 \end{pmatrix}. \tag{2.11b}$$

This already looks very similar to the Dirac-Weyl equation in momentum representation and can be brought to a more convenient form by rearranging the spinor components. The following choice is commonly made

$$H \approx \sum_{\boldsymbol{p},\sigma} \Psi(\boldsymbol{p})^\dagger \mathcal{H}(\boldsymbol{p}) \Psi(\boldsymbol{p}), \tag{2.12a}$$

where

$$\Psi(\boldsymbol{p}) = \begin{pmatrix} e^{i\pi/4} a_{\boldsymbol{K}+\boldsymbol{p},\sigma} \\ e^{i\pi/4} b_{\boldsymbol{K}+\boldsymbol{p},\sigma} \\ e^{-i\pi/4} b_{\boldsymbol{K}'+\boldsymbol{p},\sigma} \\ e^{i\pi/4} a_{\boldsymbol{K}'+\boldsymbol{p},\sigma} \end{pmatrix}, \qquad \mathcal{H} = \begin{pmatrix} 0 & v(p_x - ip_y) & 0 & 0 \\ v(p_x + ip_y) & 0 & 0 & 0 \\ 0 & 0 & 0 & v(p_x - ip_y) \\ 0 & 0 & v(p_x + ip_y) & 0 \end{pmatrix}. \tag{2.12b}$$

On the level of wave functions, this leads to the eigenvalue equation

$$v \begin{pmatrix} 0 & p_x - ip_y & 0 & 0 \\ p_x + ip_y & 0 & 0 & \\ 0 & 0 & 0 & p_x - ip_y \\ 0 & 0 & p_x + ip_y & 0 \end{pmatrix} \Psi(\boldsymbol{p}) = \varepsilon_p \Psi(\boldsymbol{p}) \tag{2.13}$$

which reads

$$-i\hbar v \begin{pmatrix} 0 & \partial_x - i\partial_y & 0 & 0 \\ \partial_x + i\partial_y & 0 & 0 & \\ 0 & 0 & 0 & \partial_x - i\partial_y \\ 0 & 0 & \partial_x + i\partial_y & 0 \end{pmatrix} \Psi(\boldsymbol{r}) = \varepsilon_p \Psi(\boldsymbol{r}) \tag{2.14}$$

in coordinate representation. In both representations, the notation was slightly simplified (abused) by using the same symbols for the objects in first quantised notation as for the corresponding Fock space operators (which should cause no problems as it is clear from the context what is meant and we will almost exclusively use the first quantised form from now on).

We close this section by commenting on Eq. (2.14) and by introducing some further

simplifying notation and helpful nomenclature.

- The first two spinor components of $\Psi(\boldsymbol{r})$ belong to excitations in the vicinity of the $\boldsymbol{K}$ point while the second pair of spinor components belongs to excitations in the vicinity of the $\boldsymbol{K}'$ point; one often expresses this by saying that those two pairs of spinor components belong to different *valleys*.

- In each valley, the excitation can be on sublattice A or on sublattice B. In analogy to spin, one often relates this sublattice degree of freedom with a so-called *pseudo-spin*. In the $\boldsymbol{K}$-valley, a pseudo-spin pointing up the z-axis corresponds to an excitation on the A sublattice while a pseudo-spin pointing down the $z-axis$ describes an excitation on sublattice B (it is the other way around in the other valley); a pseudo-spin lying in the x-y-plane corresponds to an excitation on both sublattices.

- Using the standard definition of Pauli matrices in sublattice and valley space,

$$\sigma_x = \left(\begin{smallmatrix} 0 & 1 \\ 1 & 0 \end{smallmatrix}\right), \qquad \sigma_y = \left(\begin{smallmatrix} 0 & -i \\ i & 0 \end{smallmatrix}\right), \qquad \sigma_z = \left(\begin{smallmatrix} 1 & 0 \\ 0 & -1 \end{smallmatrix}\right), \qquad \sigma_0 = \left(\begin{smallmatrix} 1 & 0 \\ 0 & 1 \end{smallmatrix}\right), \tag{2.15a}$$

$$\tau_x = \left(\begin{smallmatrix} 0 & 1 \\ 1 & 0 \end{smallmatrix}\right), \qquad \tau_y = \left(\begin{smallmatrix} 0 & -i \\ i & 0 \end{smallmatrix}\right), \qquad \tau_z = \left(\begin{smallmatrix} 1 & 0 \\ 0 & -1 \end{smallmatrix}\right), \qquad \tau_0 = \left(\begin{smallmatrix} 1 & 0 \\ 0 & 1 \end{smallmatrix}\right), \tag{2.15b}$$

  while adopting the notation $\boldsymbol{\sigma} = (\sigma_x, \sigma_y)^T$, allows us to write Eq. (2.14) very compactly as

$$-i\hbar(\boldsymbol{\sigma} \otimes \tau_0) \cdot \boldsymbol{\nabla}\Psi(\boldsymbol{r}) \equiv -i\hbar\boldsymbol{\sigma} \cdot \boldsymbol{\nabla}\Psi(\boldsymbol{r}) = \varepsilon\Psi(\boldsymbol{r}). \tag{2.16}$$

- We will typcically use units such that $\hbar v = 1$.

References of Chapter 2

[1] Neto, A. H. C., Guinea, F., Peres, N., Novoselov, K. S. & Geim, A. K. The electronic properties of graphene. *Reviews of Modern Physics* **81**, 109 (2009).

[2] Katsnelson, M. I. *Graphene.* Carbon in Two Dimensions (Cambridge University Press, Cambridge, 2012).

[3] Wallace, P. The Band Theory of Graphite. *Physical Review* **71**, 622–634 (1947).

[4] Ando, T., Nakanishi, T. & Saito, R. Berry's Phase and Absence of Back Scattering in

Carbon Nanotubes. *Journal of the Physical Society of Japan* **67**, 2857–2862 (1998).

[5] DiVincenzo, D. P. & Mele, E. J. Self-consistent effective-mass theory for intralayer screening in graphite intercalation compounds. *Physical Review B* **29**, 1685 (1984).

[6] Semenoff, G. W. Condensed-matter simulation of a three-dimensional anomaly. *Physical Review Letters* **53**, 2449–2452 (1984).

[7] Novoselov, K. S. *et al.* Two-dimensional gas of massless Dirac fermions in graphene. *Nature* **438**, 197–200 (2005).

[8] Zhang, Y., Tan, Y.-W., Stormer, H. L. & Kim, P. Experimental observation of the quantum Hall effect and Berry's phase in graphene. *Nature* **438**, 201–204 (2005).

3 Quantum transport in graphene

> Theories of the known, which are described by different physical ideas, may be equivalent in all their predictions and hence scientifically indistinguishable. However, they are not psychologically identical when trying to move on from that base into the unknown. For different views suggest different kinds of modifications which might be made and hence are not equivalent in the hypotheses one generates from them in one's attempt to understand what is not yet understood.
>
> Richard P. Feynman [1]

Following the philosophy expressed in the above quotation, we will now discuss multiple conceptual and computational frameworks for studying quantum transport in graphene and apply them to understand some of the transport properties of clean graphene. By doing so, this chapter aims to fulfil a dual purpose: First, it introduces the methods and the notation used in later chapters; second, it allows us to discuss some of those physical phenomena in their most simple form that will be relevant to the more complicated systems studied in later chapters.

We begin by describing Landauer's viewpoint on quantum transport, which tries to understand the resistance of a conductor from its scattering properties and can be condensed into the formula that bears his name (Section 3.1).

Section 3.2 introduces the transfer matrix formalism as a means to evaluate Landauer's formula and uses it to study the basic transport properties of ballistic graphene; another way to evaluate it is the mode-matching approach explained in Section 3.3, where the conductance of graphene at zero doping is calculated when there is a constant magnetic field perpendicular to the sample.

We close this chapter with a discussion of the matrix Green's function formalism (Sec-

tion 3.4) which is particularly convenient to calculate the conductance of systems with finite-range impurities using the unfolded scattering formalism (Section 3.5).

3.1 The Landauer approach to quantum transport in graphene

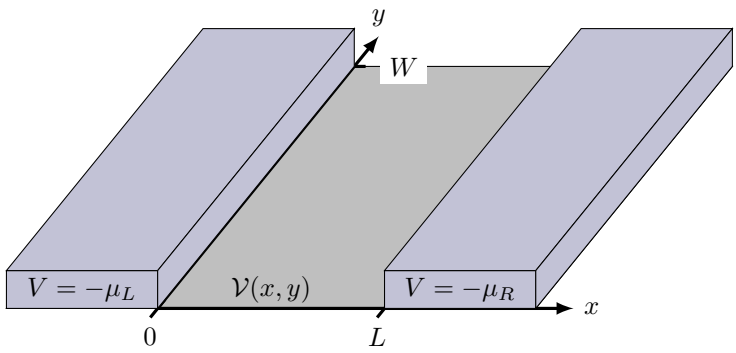

Figure 3.1: The idealised two-terminal setup considered throughout this thesis: two leads, modelled as perfect semi-infinite graphene waveguides of width W, connect a graphene sample of length L and width W to reservoirs held at local chemical potentials μ_L and μ_R. Dirac fermions in the sample are exposed to a scattering potential $\mathcal{V}$ which in general is a 8×8 matrix in spin⊗pseudospin⊗valley-space; for spin- and valley-independent scattering, we often write $\mathcal{V}(x, y) = V(x, y) + \sigma_x V_x(x, y) + \sigma_y V_y(x, y) + \sigma_z V_z(x, y)$. The bias voltage $V_{\text{bias}} = \mu_L - \mu_R$ gives rise to a current I that we will study in the zero-bias, zero-temperature limit. This figure is a slightly adapted version of Fig. 1 in Ref. [2].

In this section we will very briefly discuss the Landauer formula [3] to compute the conductance G in the zero-bias-, zero-temperature-limit,

$$G = \lim_{V_{\text{bias}} \to 0} \lim_{k_B T \to 0} \frac{I}{V_{\text{bias}}}, \tag{3.1}$$

where V_{bias} denotes the bias voltage, $k_B T$ the Boltzmann constant times the temperature and I the time average of the electric current. We will restrict ourselves to describe its *application* to the very idealised two-terminal setup shown in Fig. 3.1. This avoids a lengthy discussion of the physical subtleties and the justification of this simple-looking formula that took the quantum transport community more than a decade to fully understand (see [4] for a review).

The key idea of Landauer's approach is that the electronic conduction in a standard transport setup can be conveniently thought of as a scattering problem in which the

conductance can be deduced from the transmission properties of waves reaching the sample region via leads that act as ideal waveguides. Let us therefore start our discussion of the Landauer formula by describing the form of the wave functions in such leads. The Hamiltonian in the leads, when modelled as in Fig. 3.1, is given by

$$H = -i\boldsymbol{\sigma} \cdot \boldsymbol{\nabla} - \mu_F, \tag{3.2}$$

where we have used that for the Landauer description of the zero-bias limit, we can set $\mu_L = \mu_R \equiv \mu_F$. Since we are only interested in the transport properties at zero temperature, we only need to consider the eigenvalue equation $H\Psi(x, y) = 0$ at zero energy. The general solution of this equation in the leads can be written in a very compact form when we introduce the notion of channels. Each channel is associated with a left-moving and a right-moving plain wave with certain specified quantum numbers. For the considered system we can choose the following quantum numbers – the transversal momentum q_m (which can take a discrete set of values that depend on the boundary conditions), the valley index κ (which can either be $\boldsymbol{K}$ or $\boldsymbol{K}'$) and the electron spin σ ($\uparrow$ or $\downarrow$) – and combine them into the compound index $\boldsymbol{n} = (q_m, \kappa, \sigma)$. To be concrete, let us write down the following right- and left-going wave functions in the channel $\boldsymbol{n} = (q_m, \kappa, \sigma)$

$$\Psi_{\rightarrow,\boldsymbol{n}}(x, y) = \frac{e^{ik_m x + iq_m y}}{\sqrt{2W\cos\theta_m}} \begin{pmatrix} 1 \\ e^{i\theta_m} \end{pmatrix} \otimes \chi_{\kappa,\sigma}, \tag{3.3a}$$

$$\Psi_{\leftarrow,\boldsymbol{n}}(x, y) = \frac{e^{-ik_m x + iq_m y}}{\sqrt{2W\cos\theta_m}} \begin{pmatrix} 1 \\ -e^{-i\theta_m} \end{pmatrix} \otimes \chi_{\kappa,\sigma}, \tag{3.3b}$$

where

$$k_m = \sqrt{k_F^2 - q_m^2}, \tag{3.3c}$$

is the modulus of the wave's longitudinal momentum, the angle θ_m is defined by

$$e^{i\theta_m} = \frac{k_m + iq_m}{k_F}, \tag{3.3d}$$

and $\chi_{\kappa,\sigma}$ is a spinor in valley⊗spin-space corresponding to the valley κ and the spin σ.

(3.3e)

With these definitions the general solution to the equation $H\Psi(x,y) = 0$ reads

$$\Psi(x,y) = \begin{cases} \sum_{\boldsymbol{n}} \left[a_L^{\boldsymbol{n}} \Psi_{\rightarrow,\boldsymbol{n}} + b_L^{\boldsymbol{n}} \Psi_{\leftarrow,\boldsymbol{n}}\right], & x < 0 \\ \sum_{\boldsymbol{n}} \left[b_R^{\boldsymbol{n}} \Psi_{\rightarrow,\boldsymbol{n}} + a_L^{\boldsymbol{n}} \Psi_{\leftarrow,\boldsymbol{n}}\right] & x > L \end{cases}, \tag{3.4}$$

where the $a_L^{\boldsymbol{n}}, b_L^{\boldsymbol{n}}, a_R^{\boldsymbol{n}}, b_R^{\boldsymbol{n}}$ are complex numbers that can be interpreted as flux amplitudes (to see this, one can check that $\Psi_{\rightarrow,\boldsymbol{n}}$ and $\Psi_{\leftarrow,\boldsymbol{n}}$ are normalised such that the x-component of the probability current is of unit modulus: $\int_0^W \Psi_{\rightarrow,\boldsymbol{n}}(x,y)^\dagger \sigma_x \Psi_{\rightarrow,\boldsymbol{n}}(x,y)\mathrm{d}y = 1$ and $\int_0^W \Psi_{\leftarrow,\boldsymbol{n}}(x,y)^\dagger \sigma_x \Psi_{\leftarrow,\boldsymbol{n}}(x,y)\mathrm{d}y = -1$). One can show that for given incoming flux amplitudes (the a's), the outgoing flux amplitudes (the b's) are fixed by the condition $[-i\boldsymbol{\sigma}\cdot\boldsymbol{\nabla} + \mathcal{V}(x,y)]\Psi(x,y) = 0$ (for all $0 < x < L$); if we combine the incoming flux amplitudes of all the channels into vectors $\boldsymbol{a}_L$ and $\boldsymbol{a}_R$ and do the same with the outgoing flux amplitudes (calling those vectors $\boldsymbol{b}_L$ and $\boldsymbol{b}_R$), we can express this statement as

$$\begin{pmatrix} \boldsymbol{b}_L \\ \boldsymbol{b}_R \end{pmatrix} = S \begin{pmatrix} \boldsymbol{a}_L \\ \boldsymbol{a}_R \end{pmatrix} = \begin{pmatrix} \mathbf{r} & \mathbf{t}' \\ \mathbf{t} & \mathbf{r}' \end{pmatrix} \begin{pmatrix} \boldsymbol{a}_L \\ \boldsymbol{a}_R \end{pmatrix}. \tag{3.5}$$

S is called the *scattering matrix* of our transport setup. The scattering matrix has dimension $2N_c \times 2N_c$ (N_c being the number of channels), while its sub-blocks $\mathbf{t}, \mathbf{t}', \mathbf{r}, \mathbf{r}'$ are $N_c \times N_c$ matrices in channel space. We are now in the position to write down Landauer's expression for the conductance in the zero-bias, zero-temperature limit. It reads

$$G = \frac{e^2}{h} \mathrm{Tr}\, \mathbf{t}^\dagger \mathbf{t}, \tag{3.6}$$

where $e^2/h = 1/25\,812\,\Omega$ is called the conductance quantum (or the inverse von-Klitzing-constant).

It is important to note that the elements of the scattering matrix are not fully independent of each other as a consequence of the conservation of flux: S has to be unitary. To see that, note that the total current in x-direction, $\int_0^W \Psi(x,y)^\dagger \sigma_x \Psi(x,y)\mathrm{d}y$, when evaluated in the left lead is given by $\boldsymbol{a}_L^\dagger \boldsymbol{a}_L - \boldsymbol{b}_L^\dagger \boldsymbol{b}_L$ and has to be equal to the total current in x-direction in the right lead given by $\boldsymbol{b}_R^\dagger \boldsymbol{b}_R - \boldsymbol{a}_R^\dagger \boldsymbol{a}_R$. This can be compactly written as

$$\begin{pmatrix} \boldsymbol{a}_L^\dagger & \boldsymbol{a}_R^\dagger \end{pmatrix} \begin{pmatrix} \boldsymbol{a}_L \\ \boldsymbol{a}_R \end{pmatrix} = \begin{pmatrix} \boldsymbol{b}_L^\dagger & \boldsymbol{b}_R^\dagger \end{pmatrix} \begin{pmatrix} \boldsymbol{b}_L \\ \boldsymbol{b}_R \end{pmatrix} \overset{(3.5)}{=} \begin{pmatrix} \boldsymbol{a}_L^\dagger & \boldsymbol{a}_R^\dagger \end{pmatrix} S^\dagger S \begin{pmatrix} \boldsymbol{a}_L \\ \boldsymbol{a}_R \end{pmatrix}, \tag{3.7}$$

making the unitarity of S evident. The unitary of the scattering matrix, $S^\dagger S = S S^\dagger =$

$\mathbb{1}_{2N_c\times 2N_c}$, therefore imposes the following constraints

$$\mathbf{r}^\dagger\mathbf{r}+\mathbf{t}^\dagger\mathbf{t}=\mathbf{1}, \qquad \mathbf{r}^\dagger\mathbf{t}'+\mathbf{t}^\dagger\mathbf{r}'=\mathbf{0}, \tag{3.8a}$$

$$\mathbf{t}'^\dagger\mathbf{r}+\mathbf{r}'^\dagger\mathbf{t}=\mathbf{0}, \qquad \mathbf{t}'^\dagger\mathbf{t}'+\mathbf{r}'^\dagger\mathbf{r}'=\mathbf{1}, \tag{3.8b}$$

$$\mathbf{r}\mathbf{r}^\dagger+\mathbf{t}'\mathbf{t}'^\dagger=\mathbf{1}, \qquad \mathbf{r}\mathbf{t}^\dagger+\mathbf{t}'\mathbf{r}'^\dagger=\mathbf{0}, \tag{3.8c}$$

$$\mathbf{t}\mathbf{r}^\dagger+\mathbf{r}'\mathbf{t}'^\dagger=\mathbf{0}, \qquad \mathbf{t}\mathbf{t}^\dagger+\mathbf{r}'\mathbf{r}'^\dagger=\mathbf{1}. \tag{3.8d}$$

If the matrix $\mathbf{t}$, the matrix of transmission amplitudes, is diagonal in channel space, the Landauer formula allows for a particularly intuitive interpretation that becomes apparent when writing it in a slightly different way. To that end, we define the quantity $T_{\boldsymbol{n}}=|t_{\boldsymbol{n}}|^2$, which can be understood as the transmission probability of channel $\boldsymbol{n}$ (note that (3.8a) guarantees that $0\leq|t_{\boldsymbol{n}}|^2\leq 1$). With this definition, we can rewrite the Landauer formula as

$$G=\frac{e^2}{h}\sum_{\boldsymbol{n}}T_{\boldsymbol{n}} \tag{3.9}$$

suggesting that each channel contributes to G a conductance quantum weighted with the corresponding transmission probability.

We conclude this section commenting on a notational simplification that becomes possible when the scattering does not depend on the spin- or valley-degree of freedom. In that case we can use the transversal momentum as the channel index, $\boldsymbol{n}=(q_m)$, and take the valley- and spin-degree of freedom into account by including multiplicative constants 2_v and 2_s, respectively, in the Landauer formula: $G=(2_v2_se^2/h)\mathrm{Tr}\,\mathbf{t}^\dagger\mathbf{t}$.

3.2 The transfer matrix formalism

3.2.1 Definition of transfer matrix

Equation (3.5) can readily be rearranged to express the flux amplitudes on the right in terms of the flux amplitudes on the left:

$$\begin{pmatrix}\boldsymbol{b}_R\\ \boldsymbol{a}_R\end{pmatrix}=\begin{pmatrix}\mathbf{t}-\mathbf{r}'\mathbf{t}'^{-1}\mathbf{r} & \mathbf{r}'\mathbf{t}'^{-1}\\ -\mathbf{t}'^{-1}\mathbf{r} & \mathbf{t}'^{-1}\end{pmatrix}\begin{pmatrix}\boldsymbol{a}_L\\ \boldsymbol{b}_L\end{pmatrix}. \tag{3.10}$$

The expression $\mathbf{t}-\mathbf{r}'\mathbf{t}'^{-1}\mathbf{r}$ can be simplified to $(\mathbf{t}^{-1})^\dagger$, as according to (3.8d) one finds

$\mathbf{1} = \mathbf{t}\mathbf{t}^\dagger + \mathbf{r}'\mathbf{r}'^\dagger = \mathbf{t}\mathbf{t}^\dagger + \mathbf{r}'\mathbf{t}'^{-1}\underbrace{\mathbf{t}'\mathbf{r}'^\dagger}_{=-\mathbf{r}\mathbf{t}^\dagger} = (\mathbf{t} - \mathbf{r}'\mathbf{t}'^{-1}\mathbf{r})\mathbf{t}^\dagger$. The matrix

$$\mathcal{M} = \begin{pmatrix} (\mathbf{t}^{-1})^\dagger & \mathbf{r}'\mathbf{t}'^{-1} \\ -\mathbf{t}'^{-1}\mathbf{r} & \mathbf{t}'^{-1} \end{pmatrix}, \qquad \begin{pmatrix} \boldsymbol{b}_R \\ \boldsymbol{a}_R \end{pmatrix} = \mathcal{M} \begin{pmatrix} \boldsymbol{a}_L \\ \boldsymbol{b}_L \end{pmatrix}. \tag{3.11}$$

that relates the flux amplitudes on the right to the ones on the left is called the *transfer matrix*. The main practical advantage of introducing the transfer matrix is that it is multiplicative by definition, i.e. when considering two scattering regions in series, the total transfer matrix is just the matrix product of the two individual transfer matrices $\mathcal{M} = \mathcal{M}_2\mathcal{M}_1$.

3.2.2 Pseudo-unitarity of the transfer matrix

The flux conservation as expressed by the transfer matrix reads

$$\begin{aligned} \begin{pmatrix} \boldsymbol{a}_L^\dagger & \boldsymbol{b}_L^\dagger \end{pmatrix} \underbrace{\begin{pmatrix} \mathbf{1} & \mathbf{0} \\ \mathbf{0} & -\mathbf{1} \end{pmatrix}}_{\equiv\Sigma} \begin{pmatrix} \boldsymbol{a}_L \\ \boldsymbol{b}_L \end{pmatrix} &= \begin{pmatrix} \boldsymbol{b}_R^\dagger & \boldsymbol{a}_R^\dagger \end{pmatrix} \Sigma \begin{pmatrix} \boldsymbol{b}_R \\ \boldsymbol{a}_R \end{pmatrix} \\ &\overset{(3.10)}{=} \begin{pmatrix} \boldsymbol{a}_L^\dagger & \boldsymbol{b}_L^\dagger \end{pmatrix} \mathcal{M}^\dagger \Sigma \mathcal{M} \begin{pmatrix} \boldsymbol{a}_L \\ \boldsymbol{b}_L \end{pmatrix} \end{aligned}, \tag{3.12}$$

i.e. the transfer matrix obeys the pseudo-unitarity condition

$$\mathcal{M}^\dagger \Sigma \mathcal{M} = \Sigma. \tag{3.13}$$

This leads to a couple of practical consequences:

1. Equation (3.13) makes inverting the transfer matrix trivial:

$$\mathcal{M}^{-1} = \Sigma \mathcal{M}^\dagger \Sigma = \begin{pmatrix} \mathcal{M}_{11}^\dagger & -\mathcal{M}_{21}^\dagger \\ -\mathcal{M}_{12}^\dagger & \mathcal{M}_{22}^\dagger \end{pmatrix}. \tag{3.14}$$

2. The matrix $\mathcal{M}^\dagger\mathcal{M}$ has positive real eigenvalues (as any invertible matrix of the form $A^\dagger A$) that come in N_c reciprocal pairs $\left(\mu_i, \mu_i^{-1}\right)$. To see the latter note that when $|\mu\rangle$ is an eigenvector of $\mathcal{M}^\dagger\mathcal{M}$ to the eigenvalue $\mu \in \mathbb{R}^+$ then $\Sigma|\mu\rangle$ is an eigenvector of $\mathcal{M}^\dagger\mathcal{M}$ to the eigenvalue μ^{-1}: $\mathcal{M}^\dagger\mathcal{M}\Sigma|\mu\rangle \overset{(3.13)}{=} \left(\Sigma\mathcal{M}^{-1}\Sigma\right)\left(\Sigma\mathcal{M}^{\dagger -1}\Sigma\right)\Sigma|\mu\rangle = \Sigma(\mathcal{M}^\dagger\mathcal{M})^{-1}|\mu\rangle = \mu^{-1}\Sigma|\mu\rangle$.

3.2.3 The Pichard formula

In this section we prove the Pichard formula [5]

$$\begin{aligned} \mathrm{G} &= \frac{2_s 2_v e^2}{h} \mathrm{Tr}\, \frac{2 \cdot \mathbb{1}}{\mathcal{M}^\dagger \mathcal{M} + (\mathcal{M}^\dagger \mathcal{M})^{-1} + 2 \cdot \mathbb{1}} \\ &= \frac{2_s 2_v e^2}{h} \sum_{i=1}^{N_c} \frac{4}{\mu_i + \mu_i^{-1} + 2} \end{aligned} \tag{3.15}$$

which expresses the conductance in terms of the matrix $\mathcal{M}^\dagger \mathcal{M}$ (or, equivalently, its eigenvalues μ_1, μ_1^{-1}, …, $\mu_{N_c}, \mu_{N_c}^{-1}$).[1]

Proof of the Pichard formula 1. With Equation (3.14) it is straightforward to convince oneself that

$$\begin{aligned} \frac{1}{\mathcal{M}^\dagger \mathcal{M} + (\mathcal{M}^\dagger \mathcal{M})^{-1} + 2 \cdot \mathbb{1}} &= \frac{1}{2} \begin{pmatrix} \mathcal{M}_{11}^\dagger \mathcal{M}_{11} + \mathcal{M}_{21}^\dagger \mathcal{M}_{21} + \mathbf{1} & \mathbf{0} \\ 0 & \mathcal{M}_{12}^\dagger \mathcal{M}_{12} + \mathcal{M}_{22}^\dagger \mathcal{M}_{22} + \mathbf{1} \end{pmatrix}^{-1} \\ &\overset{(3.10)}{=} \frac{1}{2} \begin{pmatrix} \mathbf{t}^{-1} (\mathbf{t}^{-1})^\dagger + \mathbf{r}^\dagger (\mathbf{t}'^{-1})^\dagger \mathbf{t}'^{-1} r + \mathbf{1} & \mathbf{0} \\ \mathbf{0} & (\mathbf{t}'^{-1})^\dagger \mathbf{t}'^{-1} + (\mathbf{t}^{-1})^\dagger \mathbf{r}'^\dagger \mathbf{r}' \mathbf{t}'^{-1} + \mathbf{1} \end{pmatrix}^{-1}. \end{aligned} \tag{3.16}$$

2. Use the unitarity of the scattering matrix, Eq. (3.8), to show that $\mathbf{r}^\dagger (\mathbf{t}'^{-1})^\dagger \mathbf{t}'^{-1} \mathbf{r} + \mathbf{1} = \mathbf{t}^{-1} (\mathbf{t}^{-1})^\dagger$ and $(\mathbf{t}^{-1})^\dagger \mathbf{r}'^\dagger \mathbf{r}' \mathbf{t}'^{-1} + \mathbf{1} = (\mathbf{t}'^{-1})^\dagger \mathbf{t}'^{-1}$:

$$\mathbf{r}^\dagger (\mathbf{t}'^{-1})^\dagger \mathbf{t}'^{-1} \mathbf{r} + \mathbf{1} = \mathbf{t}^{-1} (\mathbf{t}^{-1})^\dagger \qquad \Leftrightarrow \tag{3.17a}$$

$$\underbrace{\mathbf{t}\mathbf{r}^\dagger}_{\overset{(3.8c)}{=} -\mathbf{r}'\mathbf{t}'^\dagger} (\mathbf{t}'^{-1})^\dagger \mathbf{t}'^{-1} \underbrace{\mathbf{r}\mathbf{t}^\dagger}_{\overset{(3.8c)}{=} -\mathbf{t}'\mathbf{r}'^\dagger} + \mathbf{t}\mathbf{t}^\dagger = \mathbf{1} \qquad \Leftrightarrow \tag{3.17b}$$

$$\mathbf{r}'\mathbf{r}'^\dagger + \mathbf{t}\mathbf{t}^\dagger = \mathbf{1} \qquad \Leftrightarrow \text{Eq. (3.8d)} \tag{3.17c}$$

$$(\mathbf{t}^{-1})^\dagger \mathbf{r}'^\dagger \mathbf{r}' \mathbf{t}'^{-1} + \mathbf{1} = (\mathbf{t}'^{-1})^\dagger \mathbf{t}'^{-1} \qquad \Leftrightarrow \tag{3.18a}$$

$$\mathbf{r}'^\dagger \mathbf{r}' + \mathbf{t}'^\dagger \mathbf{t}' = \mathbf{1} \qquad \Leftrightarrow \text{Eq. (3.8b)} \tag{3.18b}$$

[1] Here and in the following, I leave it to the reader to figure out the dimensions of unit and zero matrices.

3. Combining steps 1 and 2 of this proof yields the identity

$$\frac{\mathbb{1}}{\mathcal{M}^\dagger\mathcal{M} + (\mathcal{M}^\dagger\mathcal{M})^{-1} + 2\cdot\mathbb{1}} = \frac{1}{4}\begin{pmatrix} \mathbf{t}^\dagger\mathbf{t} & 0 \\ 0 & \mathbf{t}'\mathbf{t}'^\dagger \end{pmatrix}^{-1}. \tag{3.19}$$

4. We note that $\mathbf{t}^\dagger\mathbf{t} = \mathbf{t}'^\dagger\mathbf{t}'$ follows from the unitarity of the scattering matrix:

$$\mathbf{t}^\dagger\mathbf{t} - \mathbf{t}'^\dagger\mathbf{t}' = (\mathbf{t}^\dagger\mathbf{t} + \mathbf{r}'^\dagger\mathbf{r}') - (\mathbf{t}'^\dagger\mathbf{t}' + \mathbf{r}'^\dagger\mathbf{r}') \overset{(3.8b),(3.8b)}{=} \mathbf{1} - \mathbf{1} = \mathbf{0}. \tag{3.20}$$

5. Steps 3 and 4 combine to the statement

$$\mathrm{Tr}\,\mathbf{t}^\dagger\mathbf{t} = \mathrm{Tr}\,\frac{2\cdot\mathbb{1}}{\mathcal{M}^\dagger\mathcal{M} + (\mathcal{M}^\dagger\mathcal{M})^{-1} + 2\cdot\mathbb{1}}, \tag{3.21}$$

such that plugging this into the Landauer formula, $\mathrm{G} = (2_s 2_v e^2/h)\mathrm{Tr}\,\mathbf{t}^\dagger\mathbf{t}$, indeed proves the Pichard formula. □

3.2.4 The spatial propagator

To describe the quasi-1D transport in a typical transport setup, it is very useful to make the ansatz

$$\Psi(x, y) = \mathcal{T}_{xx'}(y)\Psi(x', y) \tag{3.22}$$

for the spinor $\Psi(x, y)$ that solves the Dirac equation for the studied setup, where $\mathcal{T}_{xx'}(y)$ is a spatial propagator that relates the Dirac spinor at one longitudinal coordinate x to the Dirac spinor at coordinate $x' \leq x$.

By construction, this operator is multiplicative (i.e. $\mathcal{T}_{xx''}(y) = \mathcal{T}_{xx'}(y)\mathcal{T}_{x'x''}(y)$ for all $x'' < x' < x$) and satisfies the initial condition $\mathcal{T}_{xx}(y) = 1$.

In transversal momentum space, Eq. (3.22) can be written as

$$\begin{aligned}
\Psi_n(x) &= \frac{1}{W}\int_0^W \mathrm{d}y\ e^{-iq_n y}\mathcal{T}_{xx'}(y)\Psi(x',y) \\
&= \frac{1}{W}\int_0^W \mathrm{d}y \int_0^W \mathrm{d}y'\ e^{-iq_n y}\mathcal{T}_{xx'}(y)\Psi(x',y')\delta(y-y') \\
&\approx \frac{1}{W}\int_0^W \mathrm{d}y \int_0^W \mathrm{d}y'\ e^{-iq_n y}\mathcal{T}_{xx'}(y)\Psi(x',y') \underbrace{\sum_{m=-M}^{M}\frac{e^{iq_m(y-y')}}{W}}_{=\delta(y-y')\text{ as }M\to\infty} \\
&= \sum_{m=-M}^{M}\left[\frac{1}{W}\int_0^W \mathrm{d}y\ e^{-i(q_n-q_m)y}\mathcal{T}_{xx'}(y)\right]\left[\frac{1}{W}\int_0^W \mathrm{d}y'\ e^{-iq_m y}\Psi(x',y')\right] \\
&\equiv \sum_{m=-M}^{M}(\hat{\mathcal{T}}_{xx'})_{nm}\Psi_m(x').
\end{aligned} \tag{3.23}$$

In the rest of this section, we study how the transfer matrix and the spatial propagator are related.

For transport calculations we often only need to consider the case $x' = 0$ and therefore use the notation $\mathcal{T}_x(y) \equiv \mathcal{T}_{x0}(y)$. Now we can use the identities and definitions

$$\Psi_n(L) = \frac{1}{\sqrt{W}}\mathcal{L}_n e^{i\sigma_z k_n L}\begin{pmatrix} b_R^n \\ a_R^n \end{pmatrix}, \tag{3.24a}$$

$$\Psi_n(0) = \frac{1}{\sqrt{W}}\mathcal{L}_n \begin{pmatrix} a_L^n \\ b_L^n \end{pmatrix}, \tag{3.24b}$$

$$\mathcal{L}_n = \frac{1}{\sqrt{2\cos\theta_n}}\begin{pmatrix} 1 & 1 \\ e^{i\theta_n} & -e^{-i\theta_n} \end{pmatrix}, \tag{3.24c}$$

to see that components of $\hat{\mathcal{T}}_L$ are related to the components of $\mathcal{M}$ via

$$\begin{aligned}
\begin{pmatrix} b_R^n \\ a_R^n \end{pmatrix} &= \sum_{m=-M}^{M} e^{-i\sigma_z k_n L}\mathcal{L}_n^{-1}(\hat{\mathcal{T}}_L)_{nm}\mathcal{L}_m \begin{pmatrix} a_L^m \\ b_L^m \end{pmatrix} \\
&\stackrel{!}{=} \sum_{m=-M}^{M}\mathcal{M}_{nm}\begin{pmatrix} a_L^m \\ b_L^m \end{pmatrix}.
\end{aligned} \tag{3.25}$$

From this we can deduce the relation between the spatial propagator and the transfer matrix we were looking for:

$$\mathcal{M}_{nm} = \mathcal{L}_n^{-1}(\hat{\mathcal{T}}_L)_{nm}\mathcal{L}_m. \tag{3.26}$$

Here the unitary matrix $\exp[-i\sigma_z k_n L]$ could be omitted as it will cancel in any transport-related expression which are all of the form $(\mathcal{M}^\dagger\mathcal{M})^n$ (This unitary factor would not have appeared in the first place if one defined the scattering states in the right lead to be proportional to $\exp[ik_n(x-L)]$).

3.2.5 Application: conductance of ballistic graphene

We consider the ballistic transport setup described by the Hamiltonian

$$H = -i\boldsymbol{\sigma}\cdot\boldsymbol{\nabla} + V(x), \tag{3.27}$$

where the scalar potential $V(x)$ is given by

$$V(x) = \begin{cases} V_S, & 0 < x < L \\ V_L = -\mu_F, & \text{otherwise} \end{cases} \tag{3.28}$$

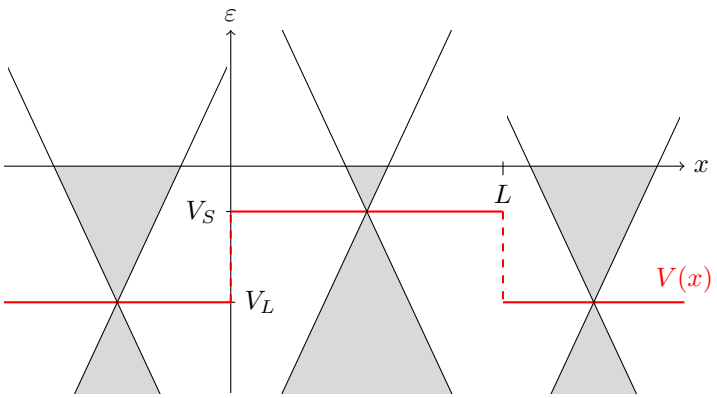

Figure 3.2: Potential profile for the ballistic setup. Note that the small bias voltage between the left and the right lead (which is implicitly assumed when using the Landauer formula later) is not shown.

The spatial propagator of this system can be found by solving the ordinary differential

equation

$$\partial_x \hat{\mathcal{T}}(x) = \left[\sigma_z \otimes \hat{q} + i\sigma_x \otimes \hat{1}(E - V_S)\right] \hat{\mathcal{T}}(x), \qquad \hat{\mathcal{T}}(0) = \hat{1}, \tag{3.29}$$

where $\hat{q}$ is the diagonal matrix $\mathrm{diag}\,(q_{-M}, \ldots, q_M)$ of transversal momenta. The solution at $E = 0$, which is only relevant one for transport at zero temperature, reads $(\hat{\mathcal{T}}_L)_{nm} = \delta_{nm} \exp\left[q_n \sigma_z - i V_s \sigma_x\right] L$ and can be expanded as

$$(\hat{\mathcal{T}}_L)_{nm} = \delta_{nm} \begin{pmatrix} \cosh \kappa_n L + (q_n/\kappa_n) \sinh \kappa_n L & -i(V_S/\kappa_n) \sinh \kappa_n L \\ -i(V_S/\kappa_n) \sinh \kappa_n L & \cosh \kappa_n L - (q_n/\kappa_n) \sinh \kappa_n L \end{pmatrix}, \tag{3.30}$$

where $\kappa_n = \sqrt{q_n^2 - V_S^2}$ (when this quantity becomes imaginary, it is useful to define also the quantity $p_n = \sqrt{V_S^2 - q_n^2}$). With this result we can easily invert the 11-component of Eq. (3.26) yielding a transmission amplitude given by

$$t_m = \frac{\kappa_m \cos\theta_m}{\kappa_m \cos\theta_m \cosh \kappa_m L - i(V_S + q_m \sin\theta_m) \sinh \kappa L}, \tag{3.31}$$

and a corresponding transmission $T_{q_m}(V_S) = t_m^\dagger t_m$ given by

$$\begin{aligned} t_m^\dagger t_m &= \frac{1}{\cosh^2 \kappa_m L - \left|\frac{V_S + q_m \sin\theta_m}{\kappa_m \cos\theta_m} \sinh \kappa_m L\right|^2} \\ &= \frac{1}{1 + \xi_m \left|\frac{q_m}{\kappa_m} \sinh \kappa_m L\right|^2}, \qquad \xi_m = \frac{(1 - V_S/V_L)^2}{1 - q_m^2/V_L^2}. \end{aligned} \tag{3.32}$$

Plugging this result into the Landauer formula for the conductance at zero temperature yields

$$\mathrm{G}_{\mathrm{ballistic}} = \frac{2_s 2_v e^2}{h} \sum_m \frac{1}{1 + \xi_m \left|\frac{q_m}{\kappa_m} \sinh \kappa_m L\right|^2}. \tag{3.33}$$

In the following we discuss the physical content of this result.

We first deal with the question of transversal boundary conditions. We do this by reproducing the conductance calculated numerically using the Kwant code [6] with the result given in Eq. (3.33) by using the proper channel-index-dependence of the transversal momentum q_m for the given edge configuration. Figure 3.3 shows that for the cases we are interested in ($W \gg L$, small sample dopings), the concrete choice of boundary

conditions is not very important so we can choose the mathematically simple periodic boundary conditions and integrate over the transversal momentum variable instead of summing it.

Figure 3.4 studies the dependence of the conductivity on a finite doping in the leads. We can observe that studying the physics around the Dirac point, the approximation of infinite doping in the leads is an uncritical one.

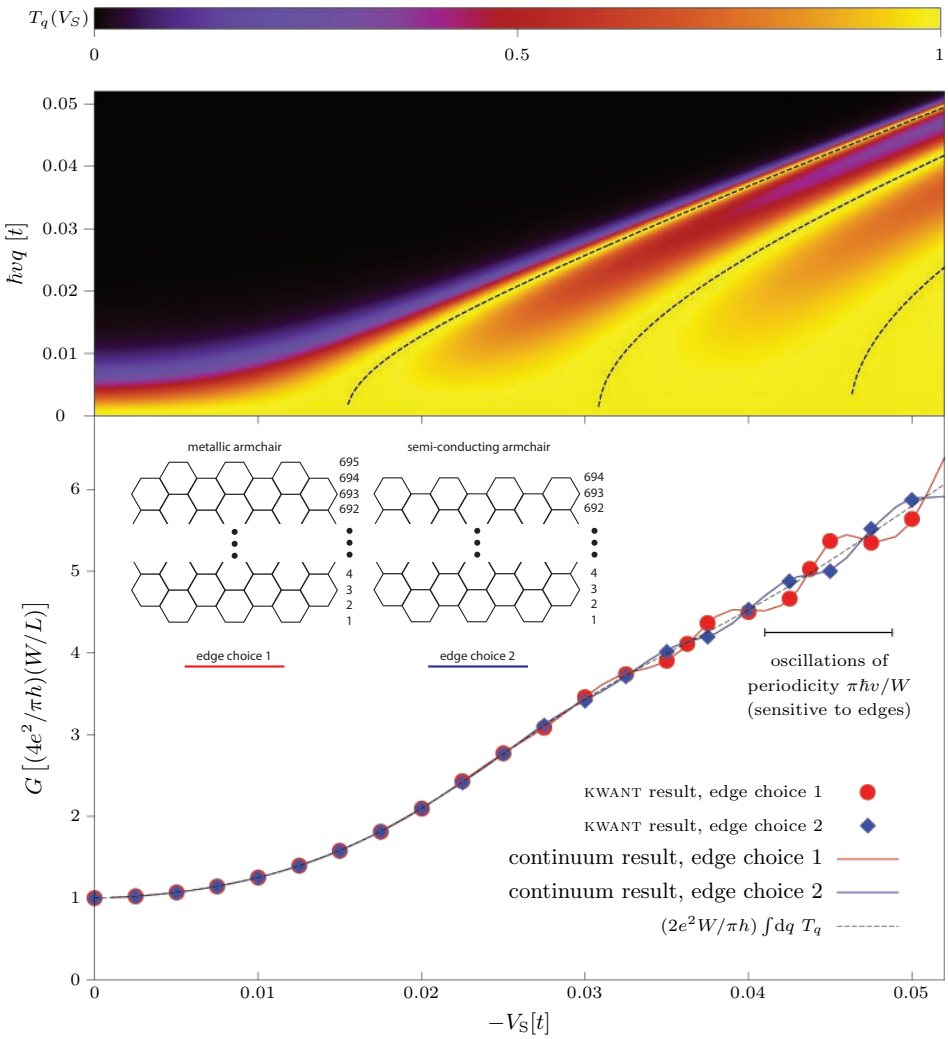

Figure 3.3: Comparison of the continuum result for the conductance, Eq. (3.33), with the conductance calculated by the Kwant package for samples characterised by $L = 204a, W = 348\sqrt{3}a \approx 600a, \mu_F = 0.15t$ and two different transversal boundary conditions. The **upper panel** shows the continuum result for the transmission $T_q(V_S)$, see Eq. (3.32), for the same parameter values as used for the Kwant simulation. The dashed curves indicate where the longitudinal momentum is a multiple of π/L (i.e. the dashed lines satisfy $q = \sqrt{V_S^2 - (m\pi/L)^2}, m = 1, 2, 3$). The **lower panel** shows that the Kwant conductances for metallic and semi-conducting armchair boundary conditions are reproduced by the continuum calculation when summing over the appropriate q-values (see [7]), while the integrated transmission interpolates between the two conductances.

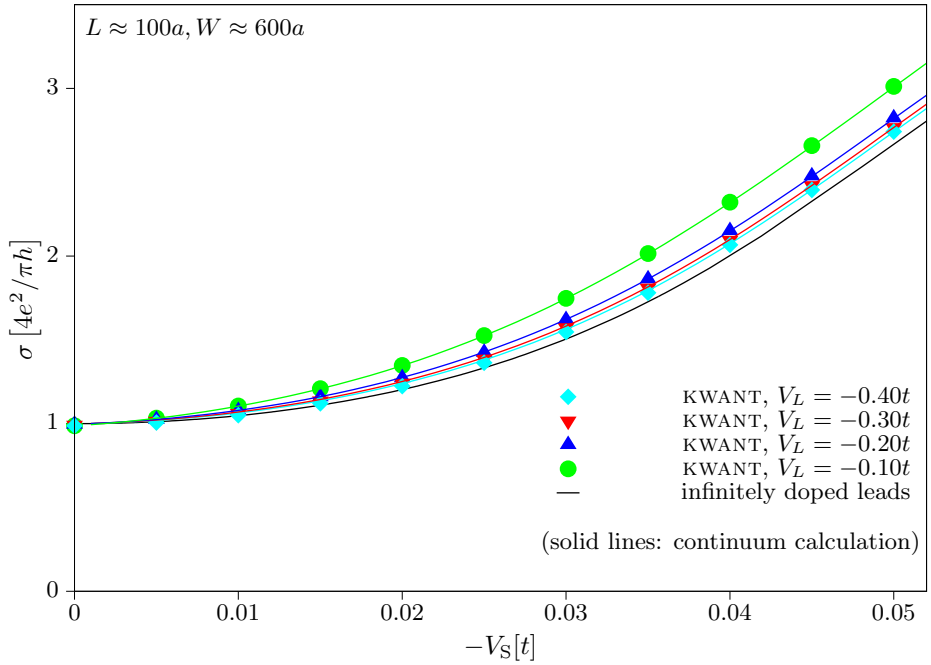

Figure 3.4: Conductivity of ballistic graphene attached to leads of various doping as a function of the sample doping. Note that for small values of the sample doping, there is hardly any dependence on the doping in the leads.

3.3 The mode-matching approach applied to clean graphene in a constant magnetic field

We shall now discuss the eigenstates and the conductance of a ballistic graphene sample at the Dirac point exposed to a constant, perpendicular magnetic field using the mode-matching approach employed in Ref. [7] to study the non-magnetic situation.

While all results derived in this section are elementary, they are still helpful in providing intuition for the more complicated case where the graphene sample is not only exposed to a magnetic field but is also disordered by short-ranged impurities as will be discussed in Chapter 5.

The states in the sample

This section discusses the eigenstates in a the zero-energy eigenstates of the Hamiltonian $H = v\boldsymbol{\sigma}\cdot(\boldsymbol{p}+(e/c)\boldsymbol{A})$, where $-e$ is the electron charge and inside the sample $\boldsymbol{\nabla}\times\boldsymbol{A} = B\boldsymbol{e}_z$. The geometry of the sample is assumed to be rectangular with $W \gg L$ and periodic boundary conditions are imposed in transversal direction. The leads are modelled by infinitely doped graphene waveguides. In the Landau gauge with $\boldsymbol{A} = (0, Bx + A_0)^{\mathrm{T}}$, the Dirac equation at zero energy takes the simple form

$$\left(\frac{\partial}{\partial_x} + i\frac{\partial}{\partial_y} + \frac{\beta(x+a_0)}{\ell_B^2}\right)\Psi_1 = 0, \tag{3.34a}$$

$$\left(\frac{\partial}{\partial_x} - i\frac{\partial}{\partial_y} - \frac{\beta(x+a_0)}{\ell_B^2}\right)\Psi_2 = 0. \tag{3.34b}$$

Here we introduced the magnetic length $\ell_B = \sqrt{\hbar c/e|B|}$ and used the abbreviations $a_0 = A_0/B$ and $\beta = \operatorname{sign} B$. Making the ansatz $\Psi_{1,2}(x,y) = \exp(iqy)\Psi_{1,2}(x)$, one finds

$$\left(\frac{\partial}{\partial_x} + \frac{\beta(x-x_0)}{\ell_B^2}\right)\Psi_1 = 0, \tag{3.35a}$$

$$\left(\frac{\partial}{\partial_x} - \frac{\beta(x-x_0)}{\ell_B^2}\right)\Psi_2 = 0, \tag{3.35b}$$

where $x_0 = \beta q\ell_B^2 - a_0$. Above set of equations is readily solved by

$$\Psi(x,y) = \sum_q e^{iqy}\begin{pmatrix} c_{q1}\cdot\exp\left[-\beta(x-x_0(q))^2/2\ell_B^2\right] \\ c_{q2}\cdot\exp\left[+\beta(x-x_0(q))^2/2\ell_B^2\right]\end{pmatrix}. \tag{3.36}$$

We see that the basis functions are plain waves in the y-direction times a Gaussian centred at x_0 in the x-direction. Because of the one-to-one correspondence of transversal momentum and the centre coordinate, $x_0(q) = \beta q \ell_B^2 - a_0, q(x_0) = \beta x_0/\ell_B^2 + eA_0/\hbar$, one can label the states either by q or x_0 and we will use both possibilities in the further text.

In an infinite system, one set of constants $\{c_{1q}\}$ or $\{c_{2q}\}$ necessarily vanishes for all q, as otherwise the wave function would not be normalisable. In a finite system, however, both sublattices can be populated; as will be shown later, one even needs finite amplitudes on both sublattices in order to match the boundary conditions at the leads-sample interfaces in our transport setup.

The states in the leads

The Hamiltonian in the leads has the form $H = v\boldsymbol{\sigma} \cdot (\boldsymbol{p} + (e/c)\boldsymbol{A}) - V_L$, where V_L is the constant scalar potential in the leads (assumed to be the same in both leads) and $\boldsymbol{A}$ takes the constant values $(0, A_0)^{\mathrm{T}}$ and $(0, A_0 + BL)^{\mathrm{T}}$ in the left and right lead, respectively. In the limit $V_L \to \infty$, the constant vector potential in the leads is irrelevant and the eigenstates are given by

$$\Phi_{q\eta}(x, y) = e^{i(\eta k x + qy)} \begin{pmatrix} 1 \\ \eta \end{pmatrix}, \qquad \eta = \pm, \qquad k = V_L. \tag{3.37}$$

Here, the symbol η distinguishes right-moving ($\eta = +1$) and left-moving states ($\eta = -1$).

Matching the wave functions

We make the following *ansatz* for the wave function coming in from the left at fixed transversal momentum q

$$\Psi_{qL}(x, y) = \begin{cases} \Phi_{q+}(x, y) + \sum_{q'} r_{qq'} \Phi_{q'-}(x, y), & \text{if } x < 0 \\ \sum_{q'} e^{iq'y} \begin{pmatrix} c_{qq'1} \cdot \exp\left[-\beta(x - x_0(q'))^2/2\ell_B^2\right] \\ c_{qq'2} \cdot \exp\left[+\beta(x - x_0(q'))^2/2\ell_B^2\right] \end{pmatrix}, & \text{if } 0 < x < L \\ \sum_{q'} t_{qq'} \Phi_{q'+}(x, y), & \text{if } x > L. \end{cases} \tag{3.38}$$

and demand that it be continuous at $x = 0$ and $x = L$. Solving the resulting linear equations yields

$$\begin{aligned} t_{qq'} &= \frac{\delta_{qq'} \cdot e^{-i\mu L}}{\cosh\left[(q - \frac{e}{\hbar c}(BL/2 + A_0))L\right]} \\ &= \frac{\delta_{qq'} \cdot e^{-i\mu L}}{\cosh\left[\frac{L}{\ell_B^2}(x_0(q) - L/2)\right]}, \end{aligned} \tag{3.39a}$$

$$c_{qq'1} = \frac{\delta_{qq'} \cdot e^{\beta(x_0(q)-L)^2/2\ell_B^2}}{\cosh\left[\frac{L}{\ell_B^2}(x_0(q) - L/2)\right]}, \tag{3.39b}$$

$$c_{qq'2} = \frac{\delta_{qq'} \cdot e^{-\beta(x_0(q)-L)^2/2\ell_B^2}}{\cosh\left[\frac{L}{\ell_B^2}(x_0(q) - L/2)\right]}, \tag{3.39c}$$

$$r_{qq'} = \delta_{qq'} \cdot \beta \tanh\left[\frac{L}{\ell_B^2}(x_0(q) - L/2)\right]. \tag{3.39d}$$

As the transmission matrix is diagonal, the transmission coefficient is simply given by $T_q = |t_{qq}|^2$, i.e.

$$T(x_0) = \frac{1}{\cosh^2\left[\frac{L}{\ell_B^2}(x_0 - L/2)\right]}. \tag{3.40}$$

As this is up to a shift the same transmission coefficient as in the non-magnetic case, the conductivity remains at $4e^2/\pi h$ in the limit $W \gg L$.

The scattering solution for an intial wave coming in from the left at transversal momentum q takes the following form in the sample:

$$\Psi_{qL}(x, y) = \frac{e^{iqy}}{\cosh\left[\frac{L}{\ell_B^2}(x_0(q) - L/2)\right]} \begin{pmatrix} \exp\left[\frac{\beta}{2\ell_B^2}\left([L - x_0(q)]^2 - [x - x_0(q)]^2\right)\right] \\ \exp\left[-\frac{\beta}{2\ell_B^2}\left([L - x_0(q)]^2 - [x - x_0(q)]^2\right)\right] \end{pmatrix}. \tag{3.41a}$$

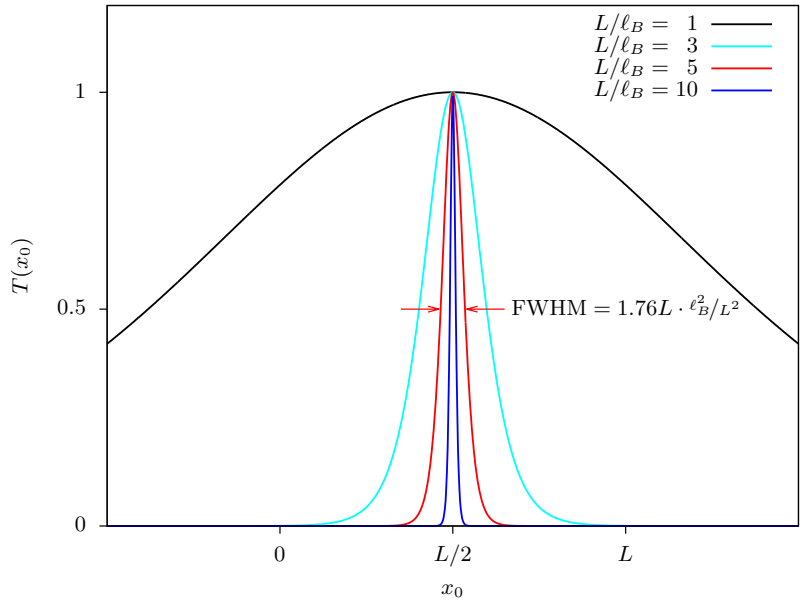

Figure 3.5: For large magnetic fields, only states with centres x_0 close to the middle of the sample contribute significantly to transport, as this plot of the transmission coefficient $T(x_0)$ (see Eq. (3.40)) demonstrates. In particular, the states whose centres are outside the sample are only important for small magnetic fields.

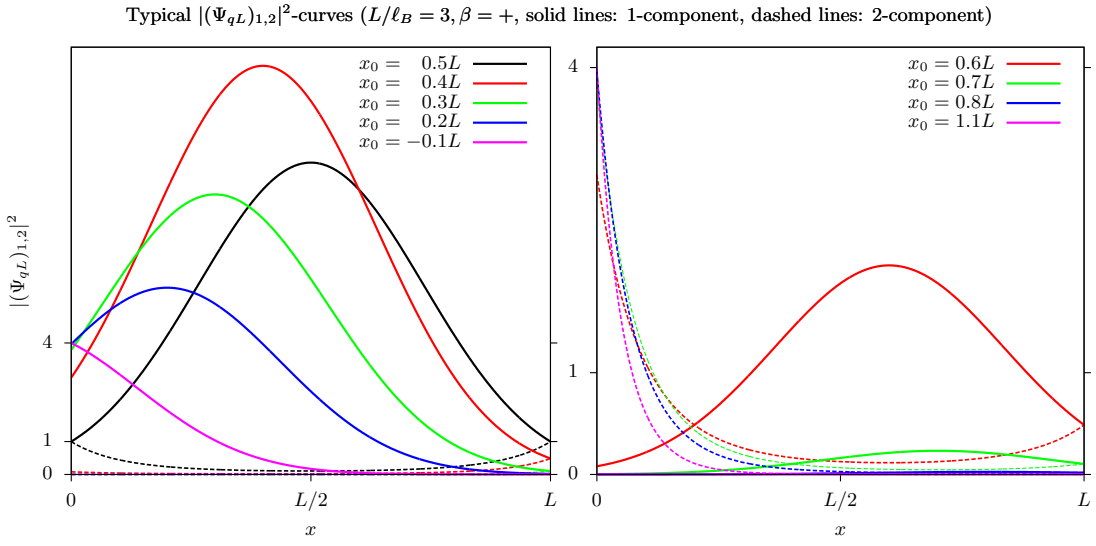

Figure 3.6: Typical states in presence of a magnetic field according to Eq. (3.41a). Note that the amplitudes at $x = L$ are on each sublattice given by the transmission $T(x_0)$ of the this mode.

3.4 The matrix Green's function formalism

In this section we introduce yet another method to determine the transport properties of the standard graphene setup. In this approach, which was proposed by Y. Nazarov in 1994[8], the conductance and higher moments of the transmission probability distribution are extracted from a suitably defined Green's function. This approach will prove particularly useful in randomly disordered systems, where the simple techniques we employed earlier (like the transfer matrix or the mode-matching formalism) become increasingly difficult, while in finding the Green's function, one is supported by a large number of well known exact and approximate solving techniques that can be readily adapted to the Dirac case.
Our starting point will be the observation that for known retarded and advanced Green's functions G^R and G^A, the two-point conductance at zero temperature can be written as

$$\mathrm{G} = \frac{2_s e^2}{h} \int_0^W \mathrm{d}y \int_0^W \mathrm{d}y' \ \mathrm{Tr}\left[\sigma_x G^R(L,y;0,y')\sigma_x G^A(0,y';L,y)\right]; \tag{3.42}$$

one can even show that more generally

$$\mathrm{Tr}\left[\mathbf{t}^\dagger\mathbf{t}\right]^n = \mathrm{Tr}\left[\sigma_x G^R(L;0)\sigma_x G^A(0;R)\right]^n. \tag{3.43}$$

Apart from being convenient on a purely technical level, this way of calculating the conductance also comes with a very intuitive interpretation (see Fig. 3.7). It suggests that in order to understand the conductance we need to consider processes where a Dirac particle propagates from the left to the right sample-lead interface, interacts there with the longitudinal current operator σ_x and then travels back to the left interface to interact with σ_x again.

Nazarov's idea is now to find the $\mathrm{Tr}\left[\mathbf{t}^\dagger\mathbf{t}\right]^n$ for all n simultaneously. To that end he introduces a generating function

$$F(z) = \sum_{n=1}^{\infty} z^{n-1} \mathrm{Tr}\left[\mathbf{t}^\dagger\mathbf{t}\right]^n, \tag{3.44a}$$

such that

$$\mathrm{Tr}\left[\mathbf{t}^\dagger\mathbf{t}\right]^n = \frac{1}{(n-1)!} \frac{\mathrm{d}^{n-1}F(z)}{\mathrm{d}z^{n-1}}\bigg|_{z=0} \tag{3.44b}$$

and shows that it can be extracted from a suitably constructed multi-component Green's function $\mathcal{G}$ in the field of a fictitious potential $\eta = \sqrt{z}$. In the following, the details of this approach are presented: in Sec. 3.4.1 we will prove Eqs. (3.43) and (3.42) by finding the Fisher-Lee relations for a graphene system; Section 3.4.2 will then discuss the generating function (3.44a) as well as one other commonly used generating function; we will then calculate the generating function (3.44a) for the case of undoped, ballistic graphene attached to infinitely doped leads, as this will involve the ballistic matrix Green's function $\mathcal{G}_0$ which will be needed in later chapters; we will conclude by presenting some useful transformations of the matrix Green's function.

3.4.1 Relating the transmission matrix to the Green's function

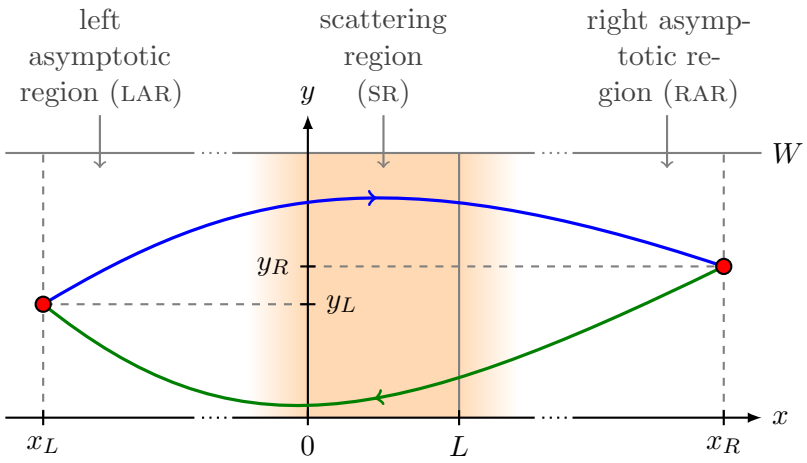

Figure 3.7: The choice of coordinate system for the transport setup to be studied. The figure also visualises a typical contribution to the Landauer conductance as given in Eq. (3.45): $\mathrm{Tr}\,\sigma_x G^R(x_L, y_L; x_R, y_R)\sigma_x G^A(x_R, y_R; x_L, y_L)$. We will later see that one can equally well set $x_L = 0, x_R = L$ due to current conservation in x-direction.

In this section, we will first derive the key equation of this approach,

$$\mathrm{G} = \frac{2_s e^2}{h} \int_0^W \mathrm{d}y_L \int_0^W \mathrm{d}y_R \; \mathrm{Tr}\left[\sigma_x G^R(x_R, y_R; x_L, y_L)\sigma_x G^A(x_L, y_L; x_R, y_R)\right], \tag{3.45}$$

which is the Dirac-equivalent to an earlier result stated in the Schrödinger context, see Ref. [8]. In this equation for the two-point conducance G at zero temperature, we assume that $x_L \in \mathrm{LAR}, x_R \in \mathrm{RAR}$ and $G^R(G^A)$ denotes the retarded (advanced) Green's

function of the disordered system which satisfies the differential equation

$$[E + \mu_{\text{lead}} \pm i0 + i\boldsymbol{\sigma} \cdot \boldsymbol{\nabla} - V(\boldsymbol{r})]\, G^{R(A)} = \delta(\boldsymbol{r} - \boldsymbol{r}'). \tag{3.46}$$

As was first noted by Nazarov in Ref. [8], the actual value of the conductance cannot depend on the choice of x_L and x_R as a consequence of current conservation. In particular it cannot be important whether the cross sections are located deep in the leads or in the disordered region; we will verify in this section, that this statement of Nazarov's indeed holds in the graphene context. Having done this, we can and typically will make the simple choice $x_L = 0, x_R = L$. Using that Eq. (3.45) does not depend on x_L and x_R we can also write the conductance as

$$\mathrm{G} = \frac{2_s e^2}{h} \frac{1}{L^2} \int_{\mathrm{SR}} \mathrm{d}^2 r \int_{\mathrm{SR}} \mathrm{d}^2 r' \ \mathrm{Tr}\ \left[\sigma_x G^R(\boldsymbol{r}; \boldsymbol{r}') \sigma_x G^A(\boldsymbol{r}'; \boldsymbol{r})\right]. \tag{3.47}$$

Proof of Eq. (3.45) To obtain Eq. (3.45), we will derive the more general statement that knowing the full Green's function of the transport setup allows us to compute all traces of the form by using the relation

$$\mathrm{Tr}\ \left[\mathbf{t}^\dagger \mathbf{t}\right]^n = \mathrm{Tr}\ \left[\sigma_x G^R(x_R; x_L) \sigma_x G^A(x_L; x_R)\right]^n, \qquad x_L \in \text{LAR},\ x_R \in \text{RAR}, \tag{3.48}$$

where the trace on the left hand side is over channel space while the trace on the right hand side includes the transversal coordinates as well as sublattice and valley indices. Having established this relation, Eq. (3.45) becomes a mere reexpression of the zero-temperature Landauer formula

$$\mathrm{G} = \frac{2_s e^2}{h} \mathrm{Tr}\, \mathbf{t}^\dagger \mathbf{t}. \tag{3.49}$$

The key to the proof of Eq. (3.48) consists in calculating the eigenstates of the Hamiltonian with disorder by means of the Lippmann-Schwinger equation which relates these eigenstates to the eigenstates without a perturbing potential by using the full Green's function as an input; comparing this result with the expected behaviour in the asymptotic

regions,

$$\Psi_{(L,n)}(\boldsymbol{r}) = \begin{cases} e^{ik_n x}\chi_n(y) + \sum_{m=-M}^{M} r_{mn} e^{-ik_m x}\tilde{\chi}_m(y), & \boldsymbol{r} \in \text{LAR} \\ \sum_{m=-M}^{M} t_{mn} e^{ik_m x}\chi_m(y), & \boldsymbol{r} \in \text{RAR} \end{cases} \tag{3.50a}$$

$$\chi_n(y) = \frac{e^{iq_n y}}{\sqrt{2W}} \begin{pmatrix} \exp[-i\theta_n/2] \\ \exp[i\theta_n/2] \end{pmatrix}, \qquad \tilde{\chi}_n(y) = \frac{e^{iq_n y}}{\sqrt{2W}} \begin{pmatrix} \exp[i\theta_n/2] \\ -\exp[-i\theta_n/2] \end{pmatrix} \tag{3.50b}$$

will then provide the sought-after relation Eq. (3.48) (this strategy was used in [4] to derive the Fisher-Lee relations in the Schrödinger case and works for the Dirac case, as well). In the above, $\Psi_{(L,n)}$ denotes the eigenstate of the disordered Hamiltonian that arises when there is only an incident wave in channel n coming from $x = -\infty$. It obeys the eigenvalue equation

$$[-i\boldsymbol{\sigma} \cdot \boldsymbol{\nabla} + V(\boldsymbol{r})]\, \Psi_{(L,n)}(\boldsymbol{r}) = (E + \mu_{\text{lead}})\Psi_{(L,n)}(\boldsymbol{r}). \tag{3.51}$$

Let us now calculate the state $\Psi_{(L,n)}(\boldsymbol{r})$ using the Lippmann-Schwinger equation

$$\Psi_{(L,n)}(\boldsymbol{r}) = \phi_{(L,n)}(\boldsymbol{r}) + \int \mathrm{d}^2 r'\; G^R(\boldsymbol{r}, \boldsymbol{r}')V(\boldsymbol{r}')\phi_{(L,n)}(\boldsymbol{r}'), \tag{3.52}$$

where

$$\phi_{(L,n)}(\boldsymbol{r}) = e^{ik_n x}\chi_n(y) \tag{3.53}$$

is the eigenstate (due to an incident wave coming from $x = -\infty$ in channel n) to the Hamiltonian without scattering potential:

$$[E + \mu_{\text{lead}} + i\boldsymbol{\sigma} \cdot \boldsymbol{\nabla}]\phi_{(L,n)}(\boldsymbol{r}) = 0. \tag{3.54}$$

To simplify the Lippmann-Schwinger equation, we make use of the differential equation (3.46) defining the full Green's function in the slightly rearranged form

$$G^R(\boldsymbol{r}, \boldsymbol{r}')V(\boldsymbol{r}') = -\delta(\boldsymbol{r} - \boldsymbol{r}') + (E + \mu_{\text{lead}} + i0)G^R(\boldsymbol{r}, \boldsymbol{r}') - i\frac{\partial G^R(\boldsymbol{r}, \boldsymbol{r}')}{\partial \boldsymbol{r}'} \cdot \boldsymbol{\sigma}. \tag{3.55}$$

Plugging this expression into the Lippmann-Schwinger equation (choosing some $\boldsymbol{r}$ in one of the asymptotic regions) and partially integrating to make the spatial derivatives act

on $\phi_{L,n}$, yields

$$\Psi_{(L,n)}(\boldsymbol{r}) = B_{x'} + B_{y'} + \int_{x_1}^{x_2}\mathrm{d}x'\int_0^W \mathrm{d}y'\; G^R(\boldsymbol{r},\boldsymbol{r}')\underbrace{\left(E+\mu_{\text{lead}}+i\boldsymbol{\sigma}\cdot\boldsymbol{\nabla}'\right)\phi_{(L,n)}(\boldsymbol{r}')}_{=0,\text{ Eq. (3.54)}}, \tag{3.56a}$$

where the boundary terms are given by

$$B_{x'} = -i\int_0^W \mathrm{d}y'\; G^R(\boldsymbol{r};x_R,y')\sigma_x\phi_{(L,n)}(x_R,y') + i\int_0^W \mathrm{d}y'\; G^R(\boldsymbol{r};x_1,y')\sigma_x\phi_{(L,n)}(x_1,y'), \tag{3.56b}$$

$$B_{y'} = -i\int_{x_1}^{x_2}\mathrm{d}x'\;\left[G^R(\boldsymbol{r};x',W)\sigma_y\phi_{(L,n)}(x',W) - G^R(\boldsymbol{r};x',0)\sigma_y\phi_{(L,n)}(x',0)\right] = 0 \tag{3.56c}$$

and x_1, x_2 are longitudinal coordinates far in the asymptotic regions such that always $x_2 > x, x_1 < x$. The boundary term $B_{y'}$ vanishes due to the boundary conditions in transversal direction. To simplify the boundary term $B_{x'}$, we use the physical intuition that the Green's function has the following factorisations in the asymptotic regions

$$G^R(\boldsymbol{r}_L;\boldsymbol{r}'_L) = \sum_{m\ell}\left[\chi_m(y_L)G^R_{\substack{\rightarrow\rightarrow\\ m\ell}}(x_L,x'_L)\chi_\ell(y'_L)^\dagger + \tilde{\chi}_m(y_L)G^R_{\substack{\leftarrow\rightarrow\\ m\ell}}(x_L,x'_L)\chi_\ell(y'_L)^\dagger\right], \tag{3.57a}$$

$$G^R(\boldsymbol{r}_R;\boldsymbol{r}'_L) = \sum_{m\ell}\chi_m(y_R)G^R_{\substack{\rightarrow\rightarrow\\ m\ell}}(x_R,x'_L)\chi_\ell(y'_L)^\dagger, \tag{3.57b}$$

$$G^R(\boldsymbol{r}_L;\boldsymbol{r}'_R) = \sum_{m\ell}\tilde{\chi}_m(y_L)G^R_{\substack{\leftarrow\leftarrow\\ m\ell}}(x_L,x'_R)\tilde{\chi}_\ell(y'_R)^\dagger, \tag{3.57c}$$

$$G^R(\boldsymbol{r}_R;\boldsymbol{r}'_R) = \sum_{m\ell}\left[\chi_m(y_R)G^R_{\substack{\rightarrow\leftarrow\\ m\ell}}(x_R,x'_R)\tilde{\chi}_\ell(y'_R)^\dagger + \tilde{\chi}_m(y_R)G^R_{\substack{\leftarrow\leftarrow\\ m\ell}}(x_R,x'_R)\tilde{\chi}_\ell(y'_R)^\dagger\right], \tag{3.57d}$$

where $\boldsymbol{r}_L, \boldsymbol{r}'_L \in$ LAR and $\boldsymbol{r}_R, \boldsymbol{r}'_R \in$ RAR (always assuming that $\boldsymbol{r}_{L(R)}$ is closer to the scattering region than $\boldsymbol{r}'_{L(R)}$ when $\boldsymbol{r}_{L(R)}, \boldsymbol{r}'_{L(R)}$ are in the same lead). From this and the orthogonality conditions

$$\int_0^W \mathrm{d}y'\; \chi_m(y')^\dagger\sigma_x\chi_n(y') = \delta_{mn}, \qquad \int_0^W \mathrm{d}y'\; \tilde{\chi}_m(y')^\dagger\sigma_x\chi_n(y') = 0 \tag{3.58}$$

we immediately see that the first term of Eq. (3.56b) vanishes. Evaluating the y'-integral in the remaining term yields

$$\Psi_{(L,n)}(\boldsymbol{r}_L) = i\sum_m \left[\chi_m(y_L)G^R_{\substack{\rightarrow\\ mn}\rightarrow}(x_L,x_1) + \tilde{\chi}_m(y_L)G^R_{\substack{\leftarrow\\ mn}\rightarrow}(x_L,x_1)\right] e^{ik_n x_1}, \tag{3.59a}$$

$$\Psi_{(L,n)}(\boldsymbol{r}_R) = i\sum_m \chi_m(y_R)G^R_{\substack{\rightarrow\\ mn}\rightarrow}(x_R,x_1)e^{ik_n x_1}. \tag{3.59b}$$

We are now in the position to compare this expressions for $\Psi_{(L,n)}(\boldsymbol{r})$ with that from Eq. (3.50a). This gives us the retarded Green's function in terms of the elements of the scattering matrix (again assuming that $\boldsymbol{r}_{L(R)}$ is closer to the scattering region than $\boldsymbol{r}'_{L(R)}$ when $\boldsymbol{r}_{L(R)}, \boldsymbol{r}'_{L(R)}$ are in the same lead),

$$G^R(\boldsymbol{r}_L;\boldsymbol{r}'_L) = -i\sum_{mn}\left[\begin{array}{l}\delta_{mn}\chi_m(y_L)e^{ik_m(x_L-x'_L)}\chi_m(y'_L)^\dagger \\ \quad + \tilde{\chi}_m(y_L)e^{-i(k_m x_L + k_n x'_L)}r_{mn}\chi_n(y'_L)^\dagger\end{array}\right], \tag{3.60a}$$

$$G^R(\boldsymbol{r}_R;\boldsymbol{r}'_L) = -i\sum_{mn}\chi_m(y_R)e^{ik_m x_R}t_{mn}e^{-ik_n x'_L}\chi_n(y'_L)^\dagger. \tag{3.60b}$$

Relations like these, which connect the elements of the scattering matrix of a system to its Green's function, are often called *Fisher-Lee relations* ([9][10]) because Daniel Fisher and Patrick Lee first established such relations in the early 1980s, see Ref. [11].

After conjugation, Eq. (3.60b) provides us with an analogous result for the advanced Green's function:

$$G^A(\boldsymbol{r}'_L;\boldsymbol{r}_R) = i\sum_{mn}\chi_m(y'_L)e^{ik_m x'_L}t^*_{mn}e^{-ik_n x_R}\chi_n(y_R)^\dagger. \tag{3.61}$$

From the equations (3.60b) and (3.61) as well as the orthogonality conditions, Eq. (3.58), the identity (3.48), immediately follows. □

Proof that Eq. (3.45) does not dependent on the choice of cross sections We need to convince ourselves that the derivative of the conductance with respect to x_L,

$$\frac{\partial G}{\partial x_L} = \frac{2_s e^2}{h}\int_0^W \mathrm{d}y_L \int_0^W \mathrm{d}y_R\ \mathrm{Tr}\left[\sigma_x \frac{\partial G^R(x_R,y_R;x_L,y_L)}{\partial x_L}\sigma_x G^A(x_L,y_L;x_R,y_R)\right.$$
$$\left. + \sigma_x G^R(x_R,y_R;x_L,y_L)\sigma_x \frac{\partial G^A(x_L,y_L;x_R,y_R)}{\partial x_L}\right], \tag{3.62}$$

vanishes. To do this, we insert the identities

$$\frac{\partial G^R(\boldsymbol{r}_R;\boldsymbol{r}_L)}{\partial x_L} = i\delta(\boldsymbol{r}_R-\boldsymbol{r}_L)\sigma_x + i\frac{\partial G^R(\boldsymbol{r}_R;\boldsymbol{r}_L)}{\partial y_L}\sigma_z - i(E+\mu_{\text{lead}}+i0-V(\boldsymbol{r}_L))G^R(\boldsymbol{r}_R;\boldsymbol{r}_L)\sigma_x, \tag{3.63a}$$

$$\frac{\partial G^A(\boldsymbol{r}_L;\boldsymbol{r}_R)}{\partial x_L} = -i\delta(\boldsymbol{r}_R-\boldsymbol{r}_L)\sigma_x - i\sigma_z\frac{\partial G^A(\boldsymbol{r}_L;\boldsymbol{r}_R)}{\partial y_L} + i\sigma_x(E+\mu_{\text{lead}}-i0-V(\boldsymbol{r}_L))G^A(\boldsymbol{r}_L;\boldsymbol{r}_R), \tag{3.63b}$$

which are direct consequences of (3.46) and find that indeed

$$\begin{aligned}\frac{\partial G}{\partial x_L} &= -\frac{2_s e^2}{h}\int_0^W \mathrm{d}y_L \int_0^W \mathrm{d}y_R\ \mathrm{Tr}\left[\sigma_x\frac{\partial G^R(x_R,y_R;x_L,y_L)}{\partial y_L}\sigma_y G^A(x_L,y_L;x_R,y_R)\right.\\ &\qquad\left. +\ \sigma_x G^R(x_R,y_R;x_L,y_L)\sigma_y\frac{\partial G^A(x_L,y_L;x_R,y_R)}{\partial y_L}\right],\\ &= -\frac{2_s e^2}{h}\int_0^W \mathrm{d}y_R\ \mathrm{Tr}\left[\sigma_x G^R(x_R,y_R;x_L,W)\sigma_y G^A(x_L,W;x_R,y_R)\right.\\ &\qquad\left. -\ \sigma_x G^R(x_R,y_R;x_L,0)\sigma_y G^A(x_L,0;x_R,y_R)\right] = 0,\end{aligned} \tag{3.64}$$

because the boundary term (which arises after partial integration with respect to y_L) vanishes due to the boundary conditions in transversal direction[2]. The proof that also $\partial G/\partial x_R = 0$ works analogously. □

3.4.2 Generating functionals

Following Nazarov, we introduce a matrix Green's function $\mathcal{G}$ that we demand to satisfy the differential equation

$$\begin{pmatrix} E+\mu-H+i0 & -\sigma_x\eta\delta(x) \\ -\sigma_x\eta\delta(x-L) & E+\mu-H-i0\end{pmatrix}\mathcal{G}(\boldsymbol{r},\boldsymbol{r}') = \delta(\boldsymbol{r}-\boldsymbol{r}'). \tag{3.65}$$

$\mathcal{G}$ has a 2×2-block structure in what we want to call Keldysh or retarded-advanced space (short: RA space). The latter nomenclature becomes clear when we consider the

[2] Physically this means that there is no current escaping in transversal direction.

case of a vanishing source field η, when above Green's function takes the simple form

$$\mathcal{G}(\boldsymbol{r},\boldsymbol{r}')\big|_{\eta=0} = \begin{pmatrix} G^R(\boldsymbol{r},\boldsymbol{r}') & 0 \\ 0 & G^A(\boldsymbol{r},\boldsymbol{r}') \end{pmatrix}. \tag{3.66}$$

When η is non-vanishing, the retarded and advanced components are mixed and $\mathcal{G}$ can be written in form of the Dyson series

$$\mathcal{G} = \begin{pmatrix} G^R & 0 \\ 0 & G^A \end{pmatrix} \sum_{n=0}^{\infty} \left[\begin{pmatrix} 0 & \eta\sigma_x\delta_0 \\ \eta\sigma_x\delta_L & 0 \end{pmatrix} \begin{pmatrix} G^R & 0 \\ 0 & G^A \end{pmatrix} \right]^n, \tag{3.67}$$

where δ_{x_0} shall denote the operator whith the matrix element $\langle \boldsymbol{r}|\delta_{x_0}|\boldsymbol{r}'\rangle = \delta(\boldsymbol{r}-\boldsymbol{r}')\delta(x-x_0)$. Using this series representation, it is easy to see that

$$\begin{aligned} \mathrm{Tr}\left[\left(\begin{smallmatrix} 0 & \sigma_x\delta_0 \\ 0 & 0 \end{smallmatrix}\right)\mathcal{G}\right] &= \mathrm{Tr}\left\{ \left(\begin{smallmatrix} 0 & \sigma_x\delta_0 \\ 0 & 0 \end{smallmatrix}\right) \left(\begin{smallmatrix} G^R & 0 \\ 0 & G^A \end{smallmatrix}\right) \sum_{n=0}^{\infty} \left[\left(\begin{smallmatrix} 0 & \eta\sigma_x\delta_0 \\ \eta\sigma_x\delta_L & 0 \end{smallmatrix}\right) \left(\begin{smallmatrix} G^R & 0 \\ 0 & G^A \end{smallmatrix}\right) \right]^n \right\} \\ &= \sum_{n=0}^{\infty} \eta^{2n+1} \mathrm{Tr}\left[\sigma_x\delta_0 G^A \sigma_x \delta_L G^R\right]^{n+1} \qquad \text{Even terms in } \eta \text{ are traceless.} \\ &\overset{\text{Eq. (3.48)}}{=} \eta \sum_{n=1}^{\infty} \eta^{2(n-1)} \mathrm{Tr}\,(\mathbf{t}^\dagger\mathbf{t})^n, \end{aligned} \tag{3.68}$$

which is, up to a factor η, the generating function defined in Eq. (3.44a).

Another way to extract the traces $\mathrm{Tr}\left[\mathbf{t}^\dagger\mathbf{t}\right]^n$ from the matrix Green's function $\mathcal{G}$ is the following:

$$\begin{aligned} \mathcal{F} &= \mathrm{Tr}\,\ln\mathcal{G}^{-1} = \ln\det\mathcal{G}^{-1} \\ &= \ln\det\left[\begin{pmatrix} E+\mu-H+i0 & -\sigma_x\eta\delta_0 \\ -\sigma_x\eta\delta_L & E+\mu-H-i0 \end{pmatrix} \begin{pmatrix} G^R & 0 \\ 0 & G^A \end{pmatrix} \right] - \underbrace{\ln\det\begin{pmatrix} G^R & 0 \\ 0 & G^A \end{pmatrix}}_{\text{independent of } \eta} \\ &\doteq \ln\det\begin{pmatrix} \mathbb{1} & -\sigma_x\eta\delta_0 G^R \\ -\sigma_x\eta\delta_L G^A & \mathbb{1} \end{pmatrix} = \mathrm{Tr}\,\ln(\mathbb{1} - \sigma_x\eta\delta_0 G^R \sigma_x\eta\delta_L G^A) \overset{(3.48)}{=} -\sum_{n=1}^{\infty} \frac{\eta^{2n}}{n} \mathrm{Tr}\,(\mathbf{t}^\dagger\mathbf{t})^n \end{aligned} \tag{3.69}$$

where $\doteq$ means equality up to an irrelevant additive term (the term is irrelevant as it does not depend on the source field). It is useful to remark at this point that $\mathcal{F}$ being defined only up to an additive constant is actually quite useful: for instance, multiplying $\mathcal{G}^{-1}$ within the trace of the logarithm by any non-singular, source-field-independent matrix only leads to yet another additive constant but might simplify the calculation of

$\mathcal{F}$ tremendously.

We further see that the generating functions

$$\mathcal{F}(z) = \mathrm{Tr}\,\ln \mathcal{G}^{-1} = -\sum_{n=1}^{\infty} \frac{z^n}{n} \mathrm{Tr}(\hat{t}^\dagger \hat{t})^n \tag{3.70a}$$

$$F(z) = \frac{1}{\eta}\,\mathrm{Tr}\,\left[\left(\begin{smallmatrix} 0 & \sigma_x\delta_0 \\ 0 & 0 \end{smallmatrix}\right)\mathcal{G}\right] = \sum_{n=1}^{\infty} z^{n-1}\,\mathrm{Tr}(\hat{t}^\dagger \hat{t})^n \tag{3.70b}$$

are related by

$$F(z) = -\frac{\mathrm{d}}{\mathrm{d}z}\mathcal{F}(z). \tag{3.71}$$

3.4.3 Application: ballistic graphene at zero doping

As an illustration of the matrix Green's function formalism, we will now use it to calculate the ballistic zero-temperature conductance of undoped graphene attached to infinitely doped leads. While this will provide no new physical results –we have already calculated this conductance earlier (see Eq. (3.33))– it is still worthwhile since we obtain as a byproduct the matrix Green's function for the clean system that will be instrumental in the disordered case.

The matrix Green's function of clean, undoped graphene

In this subsection, we would like to calculate the matrix Green's function $\mathcal{G}_0$ of clean, undoped graphene attached to infinitely doped leads. We will assume the limit of a short and wide graphene sample where the concrete choice the boundary conditions in transversal direction has no significant physical consequences so we can choose such boundary conditions that do not break the translational symmetry in y-direction. In this case the transversal momentum q, is a good quantum number and after Fourier transforming with respect to the y-direction, we find that $\mathcal{G}_0$ has to obey the differential equation

$$\begin{pmatrix} \mu(x) + i0 + i\sigma_x\partial_x - \sigma_y q & -\sigma_x\eta\delta(x) \\ -\sigma_x\eta\delta(x-L) & \mu(x) - i0 + i\sigma_x\partial_x - \sigma_y q \end{pmatrix}_{RA} \mathcal{G}_{0,q}(x,x') = \delta(x-x'), \tag{3.72}$$

where

$$\mu(x) = \begin{cases} 0, & 0 < x < L \\ \infty, & x < 0 \text{ or } x > L \end{cases} \tag{3.73}$$

is the chemical potential, η the source field and the index RA indicates that the matrix acting on $\mathcal{G}_{0,q}$ shall be interpreted as a matrix in retarded-advanced space.

Inside the sample, $x \in (0, L)$, the sub-blocks of the matrix Green's function

$$\mathcal{G}_{0,q} \equiv \begin{pmatrix} \mathcal{G}^R_{0,q} & \mathcal{G}^+_{0,q} \\ \mathcal{G}^-_{0,q} & \mathcal{G}^A_{0,q} \end{pmatrix}_{RA} \tag{3.74}$$

in retarded-advanced space satisfy the differential equations

$$[i0 + i\sigma_x\partial_x - \sigma_y q]\, \mathcal{G}^{R,+}(x, x') = \delta(x - x'), \tag{3.75a}$$

$$[-i0 + i\sigma_x\partial_x - \sigma_y q]\, \mathcal{G}^{A,-}(x, x') = \delta(x - x'), \tag{3.75b}$$

i.e. they differ from the usual retarded and advanced Green's functions merely due to different boundary conditions at the interfaces $x = 0$ and $x = L$. We will now derive these boundary conditions.

Integrating Eq. (3.72) over a small region around $x = 0$ (with x' located outside of that region) yields

$$\mathcal{G}^R_{0,q}(\epsilon, x') - \mathcal{G}^R_{0,q}(-\epsilon, x') = -i\eta\mathcal{G}^-_{0,q}(0, x'), \tag{3.76a}$$

$$\mathcal{G}^+_{0,q}(\epsilon, x') - \mathcal{G}^+_{0,q}(-\epsilon, x') = -i\eta\mathcal{G}^A_{0,q}(0, x'), \tag{3.76b}$$

$$\mathcal{G}^-_{0,q}(\epsilon, x') - \mathcal{G}^-_{0,q}(-\epsilon, x') = 0, \tag{3.76c}$$

$$\mathcal{G}^A_{0,q}(\epsilon, x') - \mathcal{G}^A_{0,q}(-\epsilon, x') = 0, \tag{3.76d}$$

where ϵ is a positive infinitesimal. This means that at the interface $x = 0$, the sub-blocks $\mathcal{G}^A_{0,q}$ and $\mathcal{G}^-_{0,q}$ are continuous, while the sub-blocks $\mathcal{G}^R_{0,q}$ and $\mathcal{G}^+_{0,q}$ have a jump. We can thus write

$$\mathcal{G}_{0,q}(\epsilon, 0) = \begin{pmatrix} \sigma_0 & -i\eta\sigma_0 \\ 0 & \sigma_0 \end{pmatrix} \mathcal{G}_{0,q}(-\epsilon, 0). \tag{3.77}$$

At the other interface, $x = L$, one finds analogously that $\mathcal{G}^R_{0,q}$ and $\mathcal{G}^+_{0,q}$ are continuous, while $\mathcal{G}^A_{0,q}$ and $\mathcal{G}^-_{0,q}$ have a jump; here the equivalent to Eq. (3.77) reads

$$\mathcal{G}_{0,q}(L + \epsilon, 0) = \begin{pmatrix} \sigma_0 & 0 \\ -i\eta\sigma_0 & \sigma_0 \end{pmatrix} \mathcal{G}_{0,q}(L - \epsilon, 0). \tag{3.78}$$

But for $x \leq -\epsilon$ and $x \geq L + \epsilon$ the sub-blocks $\mathcal{G}^{R,+}_{0,q}$ and $\mathcal{G}^{A,-}_{0,q}$ are indistinguishable from the usual retarded and advanced Green's functions, respectively, and therefore have to obey the same boundary conditions at $x = -\epsilon$ and $x = L + \epsilon$. This knowledge, together with relations Eq. (3.77) and (3.78), provides us the boundary conditions we were looking for:

$$\begin{aligned} 0 &= \begin{pmatrix} 1 & 1 & 0 & 0 \\ 0 & 0 & 1 & -1 \end{pmatrix} \mathcal{G}_{0,q}(-\epsilon, x') = \begin{pmatrix} 1 & 1 & 0 & 0 \\ 0 & 0 & 1 & -1 \end{pmatrix} \begin{pmatrix} \sigma_0 & -i\eta\sigma_0 \\ 0 & \sigma_0 \end{pmatrix}^{-1} \mathcal{G}_{0,q}(-\epsilon, x') \\ &= \begin{pmatrix} 1 & 1 & i\eta & i\eta \\ 0 & 0 & 1 & -1 \end{pmatrix} \mathcal{G}_{0,q}(\epsilon, x'), \end{aligned} \tag{3.79a}$$

$$\begin{aligned} 0 &= \begin{pmatrix} 1 & -1 & 0 & 0 \\ 0 & 0 & 1 & 1 \end{pmatrix} \mathcal{G}_{0,q}(L + \epsilon, x') = \begin{pmatrix} 1 & -1 & 0 & 0 \\ 0 & 0 & 1 & 1 \end{pmatrix} \begin{pmatrix} \sigma_0 & 0 \\ -i\eta\sigma_0 & \sigma_0 \end{pmatrix}_{RA} \mathcal{G}_{0,q}(L - \epsilon, x') \\ &= \begin{pmatrix} 1 & -1 & 0 & 0 \\ -i\eta & -i\eta & 1 & 1 \end{pmatrix} \mathcal{G}_{0,q}(L - \epsilon, x'). \end{aligned} \tag{3.79b}$$

We proceed by making the natural ansatz

$$\mathcal{G}^{\Omega}_{0,q} = \begin{cases} \begin{pmatrix} c^{\Omega}_1 e^{q(x+x')} & c^{\Omega}_2 e^{q(x-x')} \\ c^{\Omega}_3 e^{q(-x+x')} & c^{\Omega}_4 e^{-q(x+x')} \end{pmatrix}, & x < x' \\ \begin{pmatrix} \tilde{c}^{\Omega}_1 e^{q(x+x')} & \tilde{c}^{\Omega}_2 e^{q(x-x')} \\ \tilde{c}^{\Omega}_3 e^{q(-x+x')} & \tilde{c}^{\Omega}_4 e^{-q(x+x')} \end{pmatrix}, & x > x' \end{cases}, \tag{3.80}$$

where Ω takes values $R, A, +, -$. The 32 coefficients $c^R_1, \ldots, c^-_4, \tilde{c}^R_1, \ldots, \tilde{c}^-_4$ are determined by the 16 conditions provided by Eq. (3.79) and the 16 conditions provided by the discontinuity condition at $x = x'$,

$$\mathcal{G}_{0,q}(x' + \epsilon, x') - \mathcal{G}_{0,q}(x' - \epsilon, x') = -i\sigma_x, \tag{3.81}$$

which can be derived by integrating Eq. (3.72) in the region close to $x = x'$. After solving

this set of linear equations, one obtains

$$\mathcal{G}^R_{0,q}(x,x') = \frac{-i/2}{\cosh^2 qL-\eta^2}\begin{cases}\begin{pmatrix} e^{q(x+x'-L)}\cosh qL & (2\eta^2-e^{qL}\cosh qL)e^{q(x-x')} \\ (2\eta^2-e^{-qL}\cosh qL)e^{q(x'-x)} & e^{q(L-x-x')}\cosh qL\end{pmatrix}, & x<x' \\ \begin{pmatrix} e^{q(x+x'-L)}\cosh qL & e^{q(x-x'-L)}\cosh qL \\ e^{q(L-x+x')}\cosh qL & e^{q(L-x-x')}\cosh qL\end{pmatrix}, & x>x'\end{cases}, \tag{3.82a}$$

$$\mathcal{G}^A_{0,q}(x,x') = \frac{i/2}{\cosh^2 qL-\eta^2}\begin{cases}\begin{pmatrix} e^{q(x+x'-L)}\cosh qL & e^{q(L+x-x')}\cosh qL \\ e^{q(x'-x-L)}\cosh qL & e^{q(L-x-x')}\cosh qL\end{pmatrix}, & x<x' \\ \begin{pmatrix} e^{q(x+x'-L)}\cosh qL & (2\eta^2-e^{-qL}\cosh qL)e^{q(x-x')} \\ (2\eta^2-e^{qL}\cosh qL)e^{q(x'-x)} & e^{q(L-x-x')}\cosh qL\end{pmatrix}, & x>x'\end{cases}, \tag{3.82b}$$

$$\mathcal{G}^{\pm}_{0,q}(x,x') = \frac{\eta}{2(\cosh^2 qL-\eta^2)}\begin{pmatrix} e^{\mp qL-q(L-x-x')} & e^{q(x-x')} \\ e^{q(x'-x)} & e^{\pm qL+q(L-x-x')}\end{pmatrix}, \tag{3.82c}$$

Finding the Mellin transform of $f(z) = (a_0 + a_1 z)/(z - z_1)(z - z_2)$:

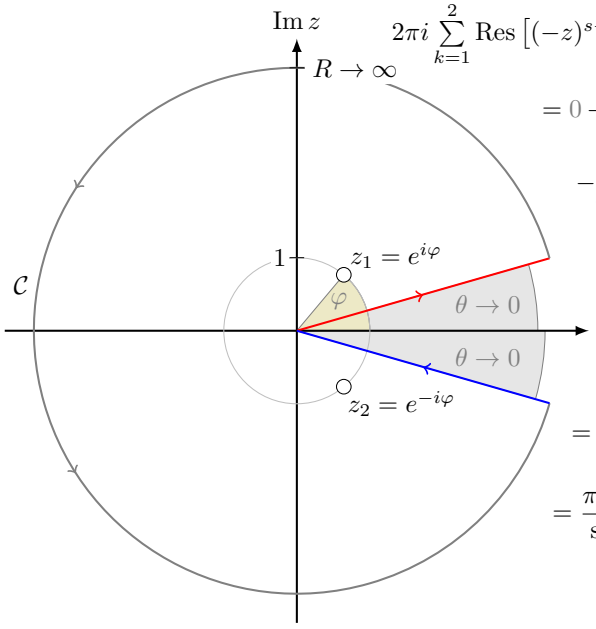

$$2\pi i \sum_{k=1}^{2} \operatorname{Res}\left[(-z)^{s-1}f(z);z_k\right] = \lim_{\substack{\theta\to 0\\ R\to\infty}} \int_{\mathcal{C}} \mathrm{d}z\ (-z)^{s-1}f(z)$$

$$= 0 + \lim_{\theta\to 0}(e^{i(-\pi+\theta)})^{s-1}\int_0^\infty \frac{\mathrm{d}x}{x}x^s f(x)$$

$$-\lim_{\theta\to 0}(e^{i(\pi+\theta)})^{s-1}\int_0^\infty \frac{\mathrm{d}x}{x}x^s f(x)$$

$$= 2i\sin\pi s\int_0^\infty \frac{\mathrm{d}x}{x}x^s f(x)$$

$$\Rightarrow \int_0^\infty \frac{\mathrm{d}x}{x}x^s f(x)$$

$$= \frac{\pi}{\sin\pi s}\sum_{k=1}^{2}\operatorname{Res}\left[(-z)^{s-1}f(z);z_k\right]$$

$$= \frac{\pi(-1)^s}{\sin\pi s}\frac{a_1\sin\varphi s - a_0\sin\varphi(s-1)}{\sin\varphi}$$

Figure 3.8: Derivation of the Mellin transformation needed to Fourier transform the matrix Green's function Eq. (3.82). Above result is consistent with integrals 12 and 13 of table 17.43 in [12] (but only up to a typographical error: in the left column of the table, the denominators should read $1+2\cos\phi+x^2$ instead of $1-2\cos\phi+x^2$, as can be checked numerically).

To get the matrix Green's function as a function of the transversal coordinates, we need to Fourier transform with respect q. We can see that the relevant integrals are all of the form

$$\int_{-\infty}^{\infty} \mathrm{d}q \; \frac{e^{q\lambda}}{\cosh^2 q - \eta^2} \overset{x=e^{2q}}{=} 2\int_0^{\infty} \frac{\mathrm{d}x}{x} \; \frac{x^{\lambda/2+1}}{x^2 + 2(1-2\eta^2)x + 1}, \tag{3.83}$$

what suggests to reparametrise the counting field by $\eta = \sin\varphi/2$ such that $(1-2\eta^2) = \cos\varphi$ and the poles of the integrand are located at $\exp[\pm i\varphi]$ (as long as φ remains real)[3]. Integrals of this type are called Mellin transforms[12] and can often be solved analytically. This is indeed the case here, see Fig. 3.8, and one obtains for the matrix Green's function

$$\mathcal{G}^{R,A}_{0,q}(\boldsymbol{r};\boldsymbol{r}') = -\frac{i}{4L\cos\frac{\varphi}{2}} \begin{pmatrix} \pm\frac{\cos\frac{\varphi}{2}[L-x-x'-i(y-y')]}{\sin\frac{\pi}{2}[x+x'+i(y-y')]} & \frac{\cos\frac{\varphi}{2}[\pm L-x+x'-i(y-y')]}{\sin\frac{\pi}{2}[x-x'+i(y-y')]} \\ \frac{\cos\frac{\varphi}{2}[\pm L-x+x'+i(y-y')]}{\sin\frac{\pi}{2}[x-x'-i(y-y')]} & \pm\frac{\cos\frac{\varphi}{2}[L-x-x'+i(y-y')]}{\sin\frac{\pi}{2}[x+x'-i(y-y')]} \end{pmatrix}, \tag{3.84a}$$

$$\mathcal{G}^{\pm}_{0,q}(\boldsymbol{r};\boldsymbol{r}') = \frac{1}{4L\cos\frac{\varphi}{2}} \begin{pmatrix} \pm\frac{\sin\frac{\varphi}{2}[\pm L+L-x-x'-i(y-y')]}{\sin\frac{\pi}{2}[x+x'+i(y-y')]} & \frac{\sin\frac{\varphi}{2}[x-x'+i(y-y')]}{\sin\frac{\pi}{2}[x-x'+i(y-y')]} \\ \frac{\sin\frac{\varphi}{2}[x-x'-i(y-y')]}{\sin\frac{\pi}{2}[x-x'-i(y-y')]} & \pm\frac{\sin\frac{\varphi}{2}[\pm L+L-x-x'+i(y-y')]}{\cos\frac{\pi}{2}[x+x'-i(y-y')]} \end{pmatrix}. \tag{3.84b}$$

Evaluating the Generating Function

We are now in the position to evaluate the generating Function $F_0(z) = F_0(\sin^2\varphi/2)$ for the clean system using Eq. (3.70b):

$$F_0(\sin^2\varphi/2) = \frac{2_s 2_v}{\sin\varphi/2}\int_0^W \mathrm{d}y \; \mathrm{Tr}\,\sigma_x G^-(0,y;0,y) = \frac{2_s 2_v W}{\pi L}\frac{\varphi}{\sin\varphi}. \tag{3.85}$$

This result indeed reproduces the familiar expression for the zero-temperature conductance of undoped graphene

$$\mathrm{G} = \frac{e^2}{h}F_0(\varphi=0) = \frac{4e^2}{\pi h}\frac{W}{L}. \tag{3.86}$$

[3] We can and at some point also will use the reparametrisation $\eta = i\sinh\phi/2, \varphi = i\phi$, when the poles are on the real axis at $-\cosh\phi \pm \sinh\phi$.

It will be useful for later chapters to also write down the generating function as a function of $\phi = -i\varphi$, that is $F_0(\phi)$, as well as calculating its potential $\mathcal{F}_0(\phi)$. We find

$$F_0(\phi) = \frac{2_s 2_v W}{\pi L} \frac{\phi}{\sinh \phi} \tag{3.87a}$$

$$\mathcal{F}_0(\phi) = \frac{W\phi^2}{\pi L}, \tag{3.87b}$$

as can be easily checked by means of Eq. (3.71), i.e. the relation $F(z) = -(\mathrm{d}/\mathrm{d}z)\mathcal{F}(z)$, while employing that $\mathrm{d}/\mathrm{d}z = (\mathrm{d}z/\mathrm{d}\phi)^{-1}\mathrm{d}/\mathrm{d}\phi = (-2/\sinh\phi)\mathrm{d}/\mathrm{d}\phi$.

3.4.4 Some useful transformations of the matrix Green's function

The way one introduces the fictitious source field η (or the related fields ϕ and φ satisfying $\eta = i\sinh\phi/2$ and $\varphi = i\phi$) within the definition of the matrix Green's function is not unique. Other choices than the one previously used may prove more practical for computations or may allow for more straightforward physical interpretations. In this section, we will justify that the field ϕ can also be inserted as an additional vector potential when the Hamiltonian satisfies the chiral symmetry $\sigma_z H = -H\sigma_z$. This approach is particularly useful as at the Dirac point where one can deal with such vector potentials very efficiently using a gauge transform proposed by Aharonov and Casher [13].

To this end, we follow [14], and make the ansatz

$$\mathcal{G}(\boldsymbol{r};\boldsymbol{r}') = V_\phi(x)\Lambda_K \tilde{\mathcal{G}}(\boldsymbol{r};\boldsymbol{r}')\Lambda_K^{-1} V_\phi^{-1}(x), \tag{3.88a}$$

for the matrix Green's function $\mathcal{G}$, where

$$V_\phi(x) = \frac{1}{\sqrt{2\cosh\phi/2}} \begin{pmatrix} e^{\frac{\phi(L-x)}{2L}} & -e^{-\frac{\phi(L-x)}{2L}} \\ e^{-\frac{\phi x}{2L}} & e^{\frac{\phi x}{2L}} \end{pmatrix} \tag{3.88b}$$

$$\Lambda_K = \frac{1}{\sqrt{2}} \begin{pmatrix} 1 & 1 \\ -1 & 1 \end{pmatrix}. \tag{3.88c}$$

As V_ϕ and Λ_K commute with any possible potential within H (even if the potential is matrix valued in spin, pseudo-spin or valley space as V_ϕ and Λ_K are proportional to the

unit matrices of these spaces), one can easily check the identity

$$\left[\begin{pmatrix} \varepsilon + i0 - H & 0 \\ 0 & \varepsilon - i0 - H \end{pmatrix}, V_\phi(x)\Lambda_K\right] = V_\phi(x)\Lambda_K \begin{pmatrix} 0 & -i\sigma_x \frac{\phi}{2L} \\ -i\sigma_x \frac{\phi}{2L} & 0 \end{pmatrix}. \tag{3.89}$$

This implies that $\tilde{\mathcal{G}}$ satisfies the differential equation

$$\begin{pmatrix} \varepsilon + i0 - H & -i\sigma_x \frac{\phi}{2L} \\ -i\sigma_x \frac{\phi}{2L} & \varepsilon - i0 - H \end{pmatrix} \tilde{\mathcal{G}}(\boldsymbol{r}, \boldsymbol{r}') = \delta(\boldsymbol{r} - \boldsymbol{r}') \tag{3.90a}$$

and has to fulfil the boundary conditions

$$\left(\begin{smallmatrix} 1 & 1 & 0 & 0 \\ 0 & 0 & 1 & -1 \end{smallmatrix}\right) \tilde{\mathcal{G}}(0, y; \boldsymbol{r}') = 0, \qquad \left(\begin{smallmatrix} 1 & -1 & 0 & 0 \\ 0 & 0 & 1 & 1 \end{smallmatrix}\right) \tilde{\mathcal{G}}(L, y; \boldsymbol{r}') = 0. \tag{3.90b}$$

It is instructive to see what consequences this transformation has for the generating function $\mathcal{F}$. To that end we first note that the transformation matrices cancel upon cyclic permutation under the trace, $\mathcal{F} = \operatorname{Tr} \ln \tilde{\mathcal{G}}^{-1}$. Repeating the very same steps that were made in Eq. (3.69), one finds that

$$\operatorname{Tr} \mathbf{t}^\dagger \mathbf{t} = 4 \frac{\mathrm{d}^2 \mathcal{F}}{\mathrm{d}\phi^2}\bigg|_{\phi=0} = \int_{\mathrm{SR}} \frac{\mathrm{d}^2 r}{L} \int_{\mathrm{SR}} \frac{\mathrm{d}^2 r'}{L} \operatorname{Tr} \left[\sigma_x G^A(\boldsymbol{r}; \boldsymbol{r}') \sigma_x G^R(\boldsymbol{r}'; \boldsymbol{r})\right], \tag{3.91}$$

which is equivalent to Eq. (3.47), suggesting that the physical principle that makes transformation (3.88) work is current conservation.

The calculation of the generating function can even be further simplified when the Hamiltonian satisfies the chiral symmetry $\sigma_z H = -H\sigma_z$, as it does in the case of clean graphene at zero doping. For the matrix Green's function (transformed according to Eq. (3.88)) of clean undoped graphene, the following ansatz therefore suggests itself,

$$\tilde{\mathcal{G}}_0(\boldsymbol{r}; \boldsymbol{r}') = \Lambda \mathcal{L} \check{\mathcal{G}}_0(\boldsymbol{r}; \boldsymbol{r}') \mathcal{L}^{-1} \Lambda, \tag{3.92a}$$

where

$$\mathcal{L} = \frac{1}{\sqrt{2}}(\Sigma_z + \Sigma_y), \qquad \Lambda = \begin{pmatrix} 1 & 0 \\ 0 & i\sigma_z \end{pmatrix}, \tag{3.92b}$$

such that $\check{\mathcal{G}}_0$ satisfies

$$\begin{pmatrix} i0 - H_0 + \frac{\phi}{2L}\sigma_y & 0 \\ 0 & i0 - H_0 - \frac{\phi}{2L}\sigma_y \end{pmatrix} \check{\mathcal{G}}_0(\boldsymbol{r};\boldsymbol{r}') = \delta(\boldsymbol{r}-\boldsymbol{r}'). \tag{3.92c}$$

We recognise that $\check{\mathcal{G}}_0$ has the simple structure

$$\check{\mathcal{G}}_0(\boldsymbol{r};\boldsymbol{r}') = \begin{pmatrix} \check{G}^R_{0,\phi}(\boldsymbol{r};\boldsymbol{r}') & 0 \\ 0 & \check{G}^R_{0,-\phi}(\boldsymbol{r};\boldsymbol{r}'), \end{pmatrix} \tag{3.93}$$

where $\check{G}^R_{0,\phi}$ is the retarded Green's function of a clean graphene system exposed to a vector potential $\boldsymbol{A}_\phi = (0, \phi/2L)^T$,

$$\left(i0 - H_0 + \frac{\phi}{2L}\sigma_y\right) \check{G}^R_{0,\phi}(\boldsymbol{r};\boldsymbol{r}') = \delta(\boldsymbol{r}-\boldsymbol{r}'), \tag{3.94}$$

complemented by the boundary conditions

$$\begin{pmatrix} 1 & 1 \end{pmatrix} \check{G}^R_{0,\phi}(0,y;\boldsymbol{r}') = 0, \qquad \begin{pmatrix} 1 & -1 \end{pmatrix} \check{G}^R_{0,\phi}(L,y;\boldsymbol{r}') = 0. \tag{3.95}$$

3.5 The unfolded scattering formalism

Nay, answer me. Stand and unfold yourself!

The second line of Shakespeare's Hamlet; 'unfold yourself' means 'identify yourself', here.

In this section we introduce the *unfolded scattering formalism* as proposed in References [15, 16] which is a very effective tool to study the transport properties of graphene with *finite-range* disorder.

In particular we will show that the conductance correction $\delta G = G - 4e^2/\pi h$ at zero doping due to N_{imp} short-range impurities can be written as

$$\delta \mathrm{G} = \frac{4e^2}{h} \frac{\partial^2 \delta \mathcal{F}}{\partial \phi^2}\bigg|_{\phi=0}, \tag{3.96a}$$

where $\delta\mathcal{F}$, the deviation of the generating function, can be obtained from a matrix determinant of the form

$$\delta\mathcal{F} = \mathrm{Tr}\ln(1 - \hat{T}\hat{\mathcal{G}}_{\mathrm{reg}}) \tag{3.96b}$$

and the $8N_{\mathrm{imp}} \times 8N_{\mathrm{imp}}$-dimensional matrices $\hat{T}$ and $\hat{\mathcal{G}}_{\mathrm{reg}}$ acting in the unfolded impurity $\otimes$ sub-lattice $\otimes$ valley $\otimes$ Keldysh space will be defined below.

To model the finite-ranged impurities, we consider a potential

$$V(\boldsymbol{r}) = \sum_{n=1}^{N_{\mathrm{imp}}} V_n(\boldsymbol{r}), \tag{3.97}$$

where the $V_n(\boldsymbol{r})$ are assumed to have finite support around the impurity position $\boldsymbol{r}_n$; we allow the $V_n(\boldsymbol{r})$ to be operators in pseudo-spin and/or valley space but assume that there is no dependence on the ordinary spin.

To obtain the conductance correction, we will employ the matrix Green's function formalism discussed in Section 3.4. We start by writing the generating function of the disordered system, $\mathcal{F}$, as a sum consisting of a clean part $\mathcal{F}_0$ and a deviation $\delta\mathcal{F}$, i.e.

$$\mathcal{F} = \mathrm{Tr}\ \ln \mathcal{G}^{-1} \equiv \mathcal{F}_0 + \delta\mathcal{F} \tag{3.98a}$$

$$\mathcal{F}_0 \equiv \mathrm{Tr}\ \ln \mathcal{G}_0^{-1} = \frac{W\phi^2}{\pi L} \tag{3.98b}$$

$$\delta\mathcal{F} \equiv \mathcal{F} - \mathcal{F}_0. \tag{3.98c}$$

To evaluate Eq. (3.98c) we use the identity $\mathcal{G}^{-1} = \mathcal{G}_0^{-1} - V$ (which is a direct consequence of the Dyson equation $\mathcal{G} = \mathcal{G}_0 + \mathcal{G}_0 V \mathcal{G}$). This yields

$$\begin{aligned}
\delta\mathcal{F} &= \mathrm{Tr}\ \ln \mathcal{G}^{-1} - \mathrm{Tr}\ \ln \mathcal{G}_0^{-1} \\
&= \mathrm{Tr}\ \ln \mathcal{G}^{-1}\mathcal{G}_0 \\
&= \mathrm{Tr}\ \ln(\mathcal{G}_0^{-1} - V)\mathcal{G}_0 \\
&= \mathrm{Tr}\ \ln(\mathbb{1} - \mathcal{G}_0 V) = \mathrm{Tr}\ \ln(\mathbb{1} - V\mathcal{G}_0).
\end{aligned} \tag{3.99}$$

So far we have not utilised the fact that the impurities are short-ranged. To facilitate

this, we will first introduce some notation that allows us to rewrite Eq. (3.99) as

$$\mathrm{Tr}\ \ln(\mathbb{1} - \mathcal{G}_0 V) = \mathrm{Tr}\ \ln(\hat{\mathbb{1}} + \hat{\mathcal{G}}_0 \hat{V}), \tag{3.100a}$$

where $\hat{V}$ and $\hat{\mathcal{G}}_0$, having components

$$(\hat{V})_{mn} = \delta_{mn} V_n, \tag{3.100b}$$

$$(\hat{\mathcal{G}}_0)_{mn} = \mathcal{G}_0, \tag{3.100c}$$

are matrices acting on a N_{imp}-dimensional vector space called *impurity space* and the trace on the right hand side of Eq. (3.100a) extends over this space as well. The introduction of impurity space fulfils an important bookkeeping task in the evaluation of Eq. (3.100a) in so far the (mn)-component of $\hat{\mathcal{G}}_0$ will only ever meet the potentials V_m and V_n from the left and right, respectively, what can be used to our advantage when the V_n are short-ranged. To see this, consider a typical convolution appearing on the RHS of Eq. (3.100a) such as

$$C_{mn\ell}(\boldsymbol{r};\boldsymbol{r}') = \int \mathrm{d}^2 r''\ [\hat{\mathcal{G}}_0(\boldsymbol{r};\boldsymbol{r}'')]_{mn} [\hat{V}(\boldsymbol{r}'')]_n [\hat{\mathcal{G}}_0(\boldsymbol{r}'';\boldsymbol{r}')]_{n\ell} \tag{3.101}$$

and imagine that we want to evaluate it at $\boldsymbol{r} = \boldsymbol{r}_{(m)} \in \mathrm{Support}_{V_m}$, $\boldsymbol{r}' = \boldsymbol{r}_{(\ell)} \in \mathrm{Support}_{V_m}$. If the potential $V_n(\boldsymbol{r}'')$ is short-ranged, such that the Green's functions in the integrand do not change significantly as a function of $\boldsymbol{r}''$ within the support of V_n (let us give this requirement the symbol $*$), we can truncate their Taylor expansion around $\boldsymbol{r}'' = \boldsymbol{r}_n$ after the zero-th order[4] and make the approximation

$$C_{mn\ell}(\boldsymbol{r}_{(m)};\boldsymbol{r}_{(\ell)}) \approx [\hat{\mathcal{G}}_0(\boldsymbol{r}_{(m)};\boldsymbol{r}_n)]_{mn} \left(\int \mathrm{d}^2 r''\ V_n(\boldsymbol{r}'') \right) [\hat{\mathcal{G}}_0(\boldsymbol{r}_n;\boldsymbol{r}_{(\ell)})]_{n\ell}, \tag{3.102}$$

what would mean that we have succeeded in replacing the convolution by a (typically matrix) multiplication. This approximation is usually referred to as s-wave approximation.

Let us now discuss how we can ensure that condition $*$ is indeed fulfilled. It is important to note that this is not just a matter of demanding the effective range of V_n to be small enough (or including a sufficient number of orders in the Taylor expansion of the Green's functions) as it is the defining property of Green's functions to have a discontinuity at coinciding spatial arguments; such a discontinuity would make the proposed approximation insufficient however short-ranged V_n is. Trying to understand how to fix this issue, we first observe that when both $\boldsymbol{r}_{(m)}$ and $\boldsymbol{r}_{(\ell)}$ are outside the support

[4] It is possible to include also higher orders as is demonstrated in Ref. [15].

of $V_n(\boldsymbol{r})$, the first and second argument of each Green's function never become close to each other when we evaluate the convolution. In particular, these arguments are never close to each other when we assume that two potentials V_j and V_k have non-overlapping support for all $j \neq k$ and demand that $m \neq n \neq \ell$. In this case we only need to pay special attention to cases where either $n = m$ or $n = \ell$ (or both) which means that it is sufficient to tweak the diagonal elements of the impurity space matrix $\hat{\mathcal{G}}_0$ to make the approximation work.

To implement this idea, we would like to partition the Green's function $\hat{\mathcal{G}}_0$ into a part that is everywhere continuous and a part that captures the singular behaviour of the Green's function for almost coinciding arguments: $\hat{\mathcal{G}}_0 = \hat{\mathcal{G}}_{\text{reg}} + \hat{g}$. This partition is not unique but there is the obvious choice

$$[\hat{g}(\boldsymbol{r};\boldsymbol{r}')]_{mn} = \frac{\delta_{mn}}{2\pi i}\frac{\boldsymbol{\sigma}\cdot(\boldsymbol{r}-\boldsymbol{r}')}{(\boldsymbol{r}-\boldsymbol{r}')^2} \tag{3.103}$$

for the singular part, where the diagonal elements are given by the Green's function of clean, infinitely extended graphene doped to the Dirac point (see Appendix 3.A.2 for its derivation). This choice for $\hat{g}$ has a couple advantages, most notably that it does not depend on the source field and that it is diagonal in RA space.

Using this partition, the deviation of the generating function takes the form

$$\begin{aligned}\delta\mathcal{F} &= \text{Tr ln}(1-\hat{V}\hat{g}-\hat{V}\hat{\mathcal{G}}_{\text{reg}})\\ &= \text{Tr ln}\left[\left(1-\hat{V}\hat{g}\right)\left(1-\frac{1}{1-\hat{V}\hat{g}}\hat{V}\hat{\mathcal{G}}_{\text{reg}}\right)\right]\\ &= \text{Tr ln}\left(1-\frac{1}{1-\hat{V}\hat{g}}\hat{V}\hat{\mathcal{G}}_{\text{reg}}\right)+\text{Tr ln}\left(1-\hat{V}\hat{g}\right).\end{aligned} \tag{3.104}$$

We see that the term $\text{Tr ln}(1-\hat{V}\hat{g})$ (that would be a problem for the aspired approximation) does not depend on the source field and can therefore be omitted. For the remaining term

$$\delta\mathcal{F} = \text{Tr ln}\left(1-\hat{T}\hat{\mathcal{G}}_{\text{reg}}\right), \tag{3.105}$$

however, the aspired approximation is possible for sufficiently short ranged potentials V_n. In the previous equation, the so-called *T-matrix*

$$[\hat{T}]_{mn} = \frac{\delta_{mn}}{1-V_n g}V_n \equiv \delta_{mn}T_n \tag{3.106}$$

was introduced whose interpretation becomes apparent when the operator $(1-V_n g)^{-1}$ is

expanded in powers of $V_n g$,

$$T_n = V_n + V_n g V_n + V_n g V_n g V_n + \dots \ . \tag{3.107}$$

This matrix sums up all the interactions with the potential involving $0, 1, 2 \dots$ many returns to the individual scattering site n.

After having regularised our expression for $\delta\mathcal{F}$ in this way, we can eventually make the approximation described in Eq. (3.103). This means that we replace the function-valued entries of $\hat{\mathcal{G}}_{\mathrm{reg}}$ by

$$\left[\hat{\mathcal{G}}_{\mathrm{reg}}\right]_{mn} \mapsto \mathcal{G}_{\mathrm{reg}}(\boldsymbol{r}_m; \boldsymbol{r}_n) = \begin{cases} \mathcal{G}_0(\boldsymbol{r}_m; \boldsymbol{r}_n), & m \neq n \\ \lim\limits_{\boldsymbol{r} \to \boldsymbol{r}_m} \left[\mathcal{G}_0(\boldsymbol{r}_m; \boldsymbol{r}) - g(\boldsymbol{r}_m; \boldsymbol{r})\right], & m = n \end{cases} , \tag{3.108}$$

while the function-valued elements of $\hat{T}$ are replaced by integrated scattering matrices

$$\begin{aligned} \left[\hat{T}\right]_{mn} &\mapsto \delta_{mn} \int \mathrm{d}^2 r \int \mathrm{d}^2 r' \ T_n(\boldsymbol{r}, \boldsymbol{r}') \\ &= \delta_{mn} \sum_{a=1}^{\infty} \int \mathrm{d}^2 r_1 \cdots \mathrm{d}^2 r_a \ V_n(\boldsymbol{r}_1) g(\boldsymbol{r}_1 - \boldsymbol{r}_2) V_n(\boldsymbol{r}_2) \cdots g(\boldsymbol{r}_{a-1} - \boldsymbol{r}_a) V_n(\boldsymbol{r}_a), \end{aligned} \tag{3.109}$$

and convolutions are replaced by ordinary (matrix) products.

In the following, we will speak of matrices acting on an *unfolded* impurity space when we want to indicate that above steps were performed to remove all convolutions within an impurity space matrix product.

This concludes the derivation of Eq. (3.96). □

Appendices to Chapter 3

3.A The Green's functions of clean, infinitely extended graphene

3.A.1 The Green's function for the tight-binding description

We begin by deriving the Green's function of clean, infinitely extended graphene on the level of the tight-binding description. This was already done, for instance, in Ref. [17], but is repeated here because some of the details of this calculation are essential to understand which divergencies encountered in studying the problem of graphene with vacancies have a physical meaning and which divergencies are merely a consequence of the employed approximations. A problem of this type was already noted in the very early papers looking at the zero energy solution in graphene with a vacancy. In Ref. [18], for instance, the authors mention that 'this solution, although decaying away from the impurity, is not normalisable.' without further explaining what this actually means. In this section we will see that this problem is merely an artefact of the effective-mass approximation (it would also occur in any other description implying the limit of a vanishing lattice constant), while the vacancy-induced state at zero energy is perfectly normalisable when the lattice constant is considered to be finite.

To calculate the Green's function, we first note that in reciprocal space, the tight-binding Hamiltonian, acting on a two-component wave function $\Psi_{\boldsymbol{k}} = (\Psi_{A,\boldsymbol{k}}, \Psi_{B,\boldsymbol{k}})^T$, has the simple form

$$H\Psi_{\boldsymbol{k}} = \begin{pmatrix} -\mu & -t_{\boldsymbol{k}} \\ -t_{\boldsymbol{k}}^* & -\mu \end{pmatrix} \Psi_{\boldsymbol{k}}, \tag{3.110}$$

where $t_{\boldsymbol{k}} = t(1 + e^{-i\boldsymbol{k}\boldsymbol{a}_1} + e^{-i\boldsymbol{k}\boldsymbol{a}_2})$. The spatial components of the zero energy Green's

function $g^R = [i0 - H]^{-1}$ are therefore given by the Fourier integral

$$\mathrm{g}^R(\boldsymbol{R};\mu) = \int_{\mathrm{BZ}} \frac{\mathrm{d}^2k}{A_{\mathrm{BZ}}} \, \frac{e^{i\boldsymbol{k}\boldsymbol{R}}}{(\mu+i0)^2 - |t_{\boldsymbol{k}}|^2} \begin{pmatrix} \mu+i0 & -t_{\boldsymbol{k}} \\ -t_{\boldsymbol{k}}^* & \mu+i0 \end{pmatrix}. \tag{3.111}$$

The main contribution to this integral comes from regions very close to the Dirac points where $t_{\boldsymbol{k}}$ vanishes and the denominator becomes small. It is therefore sensible to use the approximation $t_{\pm\boldsymbol{K}+\boldsymbol{p}} \approx ie^{\pm i\alpha}(p_x \mp ip_y)$ and replace the integrals over the first Brillouin zone by integrals over the whole $\boldsymbol{p}$-plane (we will see that the latter step causes no problems unless $\boldsymbol{R} = 0$, a case that we will need to study separately):

$$\begin{aligned}\mathrm{g}^R(\boldsymbol{R};\mu) \approx e^{i\boldsymbol{K}\boldsymbol{R}} \int \frac{\mathrm{d}^2p}{A_{\mathrm{BZ}}} \, \frac{e^{i\boldsymbol{p}\boldsymbol{R}}}{(\mu+i0)^2 - p^2} \begin{pmatrix} \mu+i0 & -ie^{i\alpha}(p_x - ip_y) \\ ie^{-i\alpha}(p_x + ip_y) & \mu+i0 \end{pmatrix} \\ + e^{-i\boldsymbol{K}\boldsymbol{R}} \int \frac{\mathrm{d}^2p}{A_{\mathrm{BZ}}} \, \frac{e^{i\boldsymbol{p}\boldsymbol{R}}}{(\mu+i0)^2 - p^2} \begin{pmatrix} \mu+i0 & -ie^{-i\alpha}(p_x + ip_y) \\ ie^{i\alpha}(p_x - ip_y) & \mu+i0 \end{pmatrix}.\end{aligned} \tag{3.112}$$

To evaluate this integral, we employ integrals of the form

$$I_1(\boldsymbol{r},\mu) \equiv \int_0^\infty \mathrm{d}p \int_0^{2\pi} \mathrm{d}\theta_p \, \frac{p e^{ipr\cos\theta_p}}{(\mu+i0)^2 - p^2} = -i\pi^2 \mathrm{sign}(\mu) H_0^{\left(\frac{3-\mathrm{sign}(\mu)}{2}\right)}(|\mu| r) \tag{3.113a}$$

$$I_2(\boldsymbol{r},\mu) \equiv \int_0^\infty \mathrm{d}p \int_0^{2\pi} \mathrm{d}\theta_p \, \frac{p^2\cos\theta_p e^{ipr\cos\theta_p}}{(\mu+i0)^2 - p^2} = \pi^2 \mu H_1^{\left(\frac{3-\mathrm{sign}(\mu)}{2}\right)}(|\mu| r) \tag{3.113b}$$

$$I_3(\boldsymbol{r}, c_1, c_2) \equiv \int \mathrm{d}^2p \, \frac{(c_1 p_x + c_2 p_y) e^{i\boldsymbol{p}\boldsymbol{r}}}{p_x^2 + p_y^2} = \frac{2\pi i (c_1 x + c_2 y)}{x^2 + y^2}, \tag{3.113c}$$

where $H_n^{(1)}$ denotes the n-th Hankel function of the first kind and $H_n^{(2)}$ the n-th Hankel function of the second kind (for completeness, above integrals are evaluated at the end of this appendix). Using these integrals, we obtain the following expressions for the retarded Green's function at zero doping

$$\mathrm{g}^R_{AA}(\boldsymbol{R};0) = \mathrm{g}^R_{BB}(\boldsymbol{R};0) = 0 \tag{3.114a}$$

$$\mathrm{g}^R_{BA}(\boldsymbol{R};0) = \mathrm{g}^R_{AB}(\boldsymbol{R};0) = \frac{A_{\mathrm{UC}}}{2\pi R} \left[e^{i\boldsymbol{K}\boldsymbol{R} + i(\theta-\alpha)} + e^{-i\boldsymbol{K}\boldsymbol{R} - i(\theta-\alpha)} \right], \tag{3.114b}$$

while for finite doping we get

$$\mathrm{g}^R_{AA}(\boldsymbol{R};\mu) = \frac{A_{\mathrm{UC}}|\mu|\,(e^{i\boldsymbol{K}\boldsymbol{R}} + e^{-i\boldsymbol{K}\boldsymbol{R}})}{4i} H_0^{\left(\frac{3-\mathrm{sign}(\mu)}{2}\right)}(|\mu|R) = \mathrm{g}^R_{BB}(\boldsymbol{R};\mu) \tag{3.115a}$$

$$\mathrm{g}^R_{BA}(\boldsymbol{R};\mu) = \frac{iA_{\mathrm{UC}}\,\mu}{4}\left[e^{i\boldsymbol{K}\boldsymbol{R}+i(\theta-\alpha)} + e^{-i\boldsymbol{K}\boldsymbol{R}-i(\theta-\alpha)}\right] H_1^{\left(\frac{3-\mathrm{sign}(\mu)}{2}\right)}(|\mu|R) = \mathrm{g}^R_{AB}(\boldsymbol{R};\mu)^*. \tag{3.115b}$$

We are particularly interested in the asymptotic behaviour of the Green's function for large values of R. Using that

$$H_m^{(1)}(x) \overset{x\gg|m^2-1/4|}{\simeq} \sqrt{\frac{2}{\pi x}} e^{ix-im\pi/2-i\pi/4}, \tag{3.116}$$

we find

$$\mathrm{g}^R_{AA}(\boldsymbol{R};\mu) \simeq \frac{e^{i\boldsymbol{K}\boldsymbol{R}} + e^{-i\boldsymbol{K}\boldsymbol{R}}}{i}\sqrt{\frac{|\mu|A_{\mathrm{UC}}^2}{8\pi R}} e^{i\mu R - i\,\mathrm{sign}(\mu)\pi/4} \tag{3.117}$$

$$\mathrm{g}^R_{BA}(\boldsymbol{R};\mu) \simeq \left(e^{i\boldsymbol{K}\boldsymbol{R}+i(\theta-\alpha)} + e^{-i\boldsymbol{K}\boldsymbol{R}-i(\theta-\alpha)}\right)\sqrt{\frac{|\mu|A_{\mathrm{UC}}^2}{8\pi R}} e^{i\mu R - i\,\mathrm{sign}(\mu)\pi/4}. \tag{3.118}$$

It remains to determine the behaviour of $\mathrm{g}^R(\boldsymbol{R};\mu)$ at coinciding points, i.e. when $\boldsymbol{R} = 0$. Naively setting $\boldsymbol{R} = 0$ in Eqs. (3.114) and (3.115) does lead to an (ultraviolet) divergence as we obtained these expressions by integrating up to arbitrarily large values of p (which is in an unjustified simplification when $\boldsymbol{R} = 0$). Instead, we will evaluate the integral (3.111) numerically. We first consider the diagonal element $\mathrm{g}^R_{AA}(0;\mu)$. Its imaginary part is unproblematic as the zeroth Bessel function of the first kind, $J_0(x) = \mathrm{Re}\,H_0^{(1,2)}(x)$, is regular and equal to one at $x = 0$. The zeroth Bessel function of the second kind, $Y_0(x) = \pm\mathrm{Im}H_0^{(1,2)}(x)$, has the asymptotic behaviour $Y_0(x) \simeq \frac{2}{\pi}\left(\ln\frac{x}{2} + \gamma\right)$ for small arguments and it is sensible to use this asymptotic expression with a suitable cuttoff length as an ansatz to fit the numerical result. Indeed, one finds that the diagonal part of Green's function at coinciding points is well approximated by

$$\mathrm{g}^R_{AA}(\boldsymbol{0};\mu) \approx -\frac{A_{\mathrm{UC}}\mu}{\pi}\left[\ln\frac{2}{|\mu|r_0} - \gamma + \mathrm{sign}(\mu)\frac{i\pi}{2}\right], \qquad r_0 \approx 0.56a, \tag{3.119}$$

as is confirmed by Fig. 3.A.1.

Numerical integration of the off-diagonal components of the Green's function suggests that

$$\mathrm{g}^R_{BA}(\boldsymbol{0};\mu) \approx \frac{a}{2}. \tag{3.120}$$

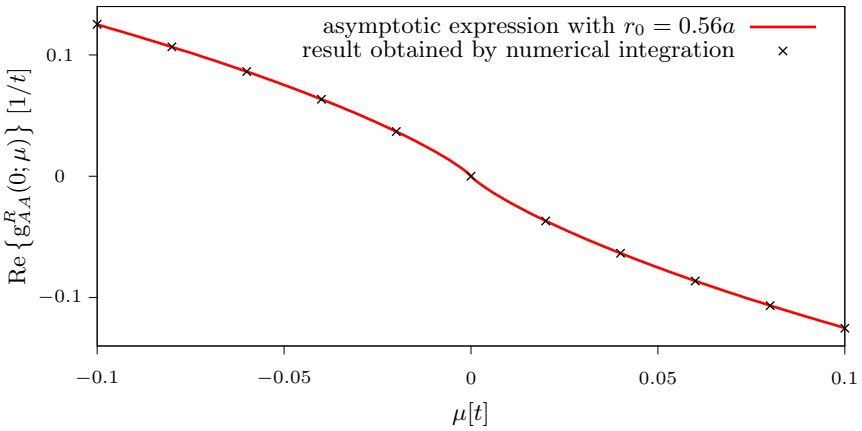

Figure 3.A.1: The plot shows that the real part of the retarded Green's function at coinciding points (as obtained by numerical integration of Eq. (3.111)) is well approximated by the asymptotic expression $-(A_{\mathrm{UC}}\mu/\pi)\ln[2/|\mu|r_0]$ where the cutoff length was fitted to $r_0 = 0.56a$.

3.A.2 The Green's function for the effective-mass description

We start by writing down the Green's function in momentum space (the inversion of $\mu + i0 - H$ is straightforward here) finding that $g^R(\boldsymbol{k}, \boldsymbol{k}'; \mu) = \delta(\boldsymbol{k} - \boldsymbol{k}')g^R(\boldsymbol{k}; \mu)$ with

$$g(\boldsymbol{k}; \mu) = \frac{(\mu + i0) + \boldsymbol{\sigma} \cdot \boldsymbol{k}}{(\mu + i0)^2 - \boldsymbol{k}^2}. \tag{3.121}$$

To get the Green's function in coordinate space we have to calculate the Fourier integral

$$g^R(\boldsymbol{r}; \mu) = \int \frac{\mathrm{d}^2 k}{(2\pi)^2} \, \frac{(\mu + i0) + \boldsymbol{\sigma} \cdot \boldsymbol{k}}{(\mu + i0)^2 - \boldsymbol{k}^2} e^{i\boldsymbol{k}\boldsymbol{r}}, \tag{3.122}$$

that can readily be reduced to the integrals I_1 to I_3 of Eq. (3.113) and one obtains

$$g(\boldsymbol{r}; 0) = \frac{1}{2\pi i} \frac{\boldsymbol{\sigma} \cdot \boldsymbol{r}}{r^2}, \tag{3.123a}$$

$$g^R(\boldsymbol{r}; \mu) = \frac{|\mu|}{4i} \left[H_0^{\left(\frac{3-\mathrm{sign}(\mu)}{2}\right)}(|\mu|r) + i\,\mathrm{sign}(\mu) \left(\boldsymbol{\sigma} \cdot \frac{\boldsymbol{r}}{r}\right) H_1^{\left(\frac{3-\mathrm{sign}(\mu)}{2}\right)}(|\mu|r) \right], \tag{3.123b}$$

Note that the retarded and advanced Green's function coincide at zero doping (as it was the case in the tight-binding Green's function), and the superscript could therefore be

dropped. For large values of $|\boldsymbol{r}|$, the Green's function at finite doping has the asymptotic behaviour

$$g^R(\boldsymbol{r};\mu) \simeq -i\sqrt{\frac{|\mu|}{8\pi r}}e^{i\mu r - i\,\mathrm{sign}(\mu)\,\pi/4}\left(1+\boldsymbol{\sigma}\cdot\frac{\boldsymbol{r}}{r}\right). \tag{3.124}$$

Some technical details

The integral I_1

$$\begin{aligned}
\int_0^\infty \mathrm{d}p \int_0^{2\pi} \mathrm{d}\theta_p \, \frac{p e^{ipr\cos\theta_p}}{(\mu+i0)^2-p^2} &= 2\pi \int_0^\infty \mathrm{d}p \, \frac{p\, J_0(pr)}{(\mu+i0)^2-p^2} \\
= 2\pi \int_0^\infty \mathrm{d}p \, \frac{p\left[H_0^{(1)}(pr) - H_0^{(1)}(e^{i\pi}pr)\right]/2}{(\mu+i0)^2-p^2} &= \pi \int_{-\infty}^\infty \mathrm{d}p \, \frac{pH_0^{(1)}(pr)}{(\mu+i0)^2-p^2} \\
= \pi \int_{-\infty}^\infty \mathrm{d}p \, H_0^{(1)}(pr)\left[\frac{-1/2}{p-(\mu+i0)} + \frac{-1/2}{p+(\mu+i0)}\right] &= -i\pi^2 H_0^{(1)}\left[(\mu+i0)r\right] \\
= -i\pi^2 \,\mathrm{sign}(\mu) H_0^{\left(\frac{3-\mathrm{sign}(\mu)}{2}\right)}(|\mu|r)&
\end{aligned} \tag{3.125}$$

Remarks: The first equality uses the standard integral representation of the zeroth Bessel function of the first kind,

$$\int_0^{2\pi} \mathrm{d}\theta \; e^{ix\cos\theta} = 2\pi J_0(x). \tag{3.126}$$

To justify the second equality, we refer to equation 5 on page 75 of [19] according to which

$$H_\nu^{(1)}(ze^{m\pi i}) = \frac{\sin(1-m)\nu\pi}{\sin\nu\pi}H_\nu^{(1)}(z) - e^{-\nu\pi i}\frac{\sin m\nu\pi}{\sin\nu\pi}H_\nu^{(2)}(z) \tag{3.127}$$

i.e.

$$H_0^{(1)}(ze^{i\pi}) = -H_0^{(2)}(z). \tag{3.128}$$

This assumes the standard convention where the Hankel functions are defined with a branch cut along the negative real numbers with a discontinuity when going from $z = e^{i(\pi-0)}$ to $z = e^{i(\pi+0)}$. For the fifth equality the residue theorem was used (the

contour can be closed by an infinitely large semi-circle in the upper half of the complex plain where the Hankel function goes to zero sufficiently fast). The last equality uses (3.128) again (here seems to be an error in Ref. [17] in the case of $\mu < 0$). □

The integral I_2

The expression for I_2 directly follows from $I_2 = -i(\partial/\partial_r)I_1$ and the recursion relation

$$\frac{\mathrm{d}}{\mathrm{d}z}H_0^{(1,2)}(z) = -H_1^{(1,2)}(z). \tag{3.129}$$

The integral I_3

$$\begin{aligned}
\int \mathrm{d}^2p\ \frac{p_y e^{i\boldsymbol{pr}}}{p_x^2+p_y^2} &= \int_{-\infty}^{\infty}\mathrm{d}p_x \int_{-\infty}^{\infty}\mathrm{d}p_y\ \frac{p_y e^{ip_x x+ip_y y}}{p_x^2+p_y^2} \\
&= \int_{-\infty}^{\infty}\mathrm{d}p_x\ e^{ip_x x}\int_{-\infty}^{\infty}\mathrm{d}p_y \left[\frac{1/2}{p_y - i|p_x|} + \frac{1/2}{p_y + i|p_x|}\right] e^{ip_y y} \\
&= i\pi \int_{-\infty}^{\infty}\mathrm{d}p_x\ \mathrm{sign}(y) e^{ip_x x - |p_x y|} \\
&= i\pi\,\mathrm{sign}(y)\left[\int_{-\infty}^{0}\mathrm{d}p_x\ e^{ip_x x + p_x|y|} + \int_{0}^{\infty}\mathrm{d}p_x\ e^{ip_x x - p_x|y|}\right] \\
&= i\pi\,\mathrm{sign}(y)\left[\frac{1}{ix+|y|} - \frac{1}{ix-|y|}\right] = \frac{2\pi i y}{x^2+y^2}
\end{aligned} \tag{3.130}$$

Remarks: The integral is well-defined despite the singularity at $p_x = p_y = 0$ because the p_y in the numerator makes the diverging contributions infinitesimally below and above the singularity cancel. In the third equality, the residue theorem was used. For positive y, one closes the contour by a semi-circle in the upper half of the complex plane, for negative y by a semi-circle in the lower half of the complex plane (the sign y is due to the fact, that in the latter case, one encircles the pole with mathematically negative orientation). One can get the integral involving p_x in the numerator by replacing $x \leftrightarrow y$ in above calculation.

References of Chapter 3

[1] Feynman, R. P. The development of the space-time view of quantum electrodynamics. *Nobel lecture, Stockholm* (1966).

[2] Titov, M. Impurity-assisted tunneling in graphene. *EPL (Europhysics Letters)* **79**, 17004 (2007).

[3] Landauer, R. Spatial Variation of Currents and Fields Due to Localized Scatterers in Metallic Conduction. *IBM journal of research and development* **1**, 223–231 (1957).

[4] Stone, A. & Szafer, A. What is measured when you measure a resistance?—The Landauer formula revisited. *IBM journal of research and development* **32**, 384–413 (1988).

[5] Pichard, J.-L., Sanquer, M., Slevin, K. & Debray, P. Broken symmetries and localization lengths in Anderson insulators: Theory and experiment. *Physical Review Letters* **65**, 1812 (1990).

[6] Groth, C. W., Wimmer, M., Akhmerov, A. R. & Waintal, X. Kwant: a software package for quantum transport. *New Journal of Physics* **16**, 063065 (2014).

[7] Tworzydło, J., Trauzettel, B., Titov, M., Rycerz, A. & Beenakker, C. W. J. Sub-Poissonian Shot Noise in Graphene. *Physical Review Letters* **96** (2006).

[8] Nazarov, Y. Limits of universality in disordered conductors. *Physical Review Letters* **73**, 134–137 (1994).

[9] Datta, S. *Electronic Transport in Mesoscopic Systems* (Cambridge University Press, Cambridge, 1997).

[10] Di Ventra, M. *Electrical Transport in Nanoscale Systems* (Cambridge University Press, Cambridge, 2008).

[11] Fisher, D. S. & Lee, P. A. Relation between conductivity and transmission matrix. *Physical Review* **B23**, 6851–6854 (1981).

[12] Gradshtein, I. S., Ryzhik, I. M., Jeffrey, A. & Zwillinger, D. *Table of Integrals, Series, and Products* (Academic Press, New York, 2000).

[13] Aharonov, Y. & Casher, A. Ground state of a spin-1/2 charged particle in a two-dimensional magnetic field. *Physical Review A* **19**, 2461–2462 (1979).

[14] Gattenlöhner, S. *et al.* Quantum Hall Criticality and Localization in Graphene with Short-Range Impurities at the Dirac Point. *Physical Review Letters* **112**, 026802 (2014).

[15] Titov, M., Ostrovsky, P., Gornyi, I. V., Schuessler, A. & Mirlin, A. D. Charge Transport in Graphene with Resonant Scatterers. *Physical Review Letters* **104** (2010).

[16] Ostrovsky, P., Titov, M., Bera, S., Gornyi, I. V. & Mirlin, A. D. Diffusion and Criticality in Undoped Graphene with Resonant Scatterers. *Physical Review Letters* **105**, 266803 (2010).

[17] Basko, D. M. Resonant low-energy electron scattering on short-range impurities in graphene. *Physical Review B* **78**, 115432 (2008).

[18] Pereira, V., Guinea, F., Lopes dos Santos, J., Peres, N. & Castro Neto, A. Disorder Induced Localized States in Graphene. *Physical Review Letters* **96**, 036801 (2006).

[19] Watson, G. N. *A Treatise on the Theory of Bessel Functions* (Cambridge University Press, Cambridge, 1996), 2 edn.

4 The Dirac-Kronig-Penney model of strain-engineered graphene

4.1 Introduction

The peculiar bandstructure of graphene, as discussed in Chapter 2, leads to interesting analogies with relativistic quantum electrodynamics [1], but the absence of energy band-gaps prevents the direct use of graphene in field-effect transistors [2, 3]. One promising suggestion to circumvent this problem is to modify the band structure of graphene by means of strain-engineering [4, 5]. On the level of the effective-mass-description of graphene, as discussed in Section 2.2, a strain gradient introduces a pseudo-magnetic field, which can be manipulated to induce a zero-field quantum Hall effect [6]. The variation of strain may also cause changes in the on-site energies of the electrons, but this effect is reduced by screening [7].

Following the above proposal, we analyse the phase-coherent charge transport in periodically strained graphene samples and suggest a way to characterise the quality of graphene superstructures on the basis of their transport properties. To do so, we use the exact solution of the Dirac-Kronig-Penney model to calculate density of states, conductance, and shot noise in transport through finite size graphene samples with periodic potentials. The scattering off the metal leads is taken into account in all quantities. The position, the width, and the shape of the conductance minimum as well as the shot noise maximum associated with the periodic superstructure are studied in detail.

The contents of this chapter were published in Reference [8] (parts have originally been written by M. Titov and W. Belzig) and are organised as follows. The effective Dirac Hamiltonian for deformed graphene is described in Section 4.2. The transfer matrix approach to transport is briefly recapitulated in Section 4.3. Section 4.4 is devoted to the exact solution of the Dirac-Kronig-Penney model for graphene with one-dimensional modulations of strain in transport direction. The generalization of this model is discussed

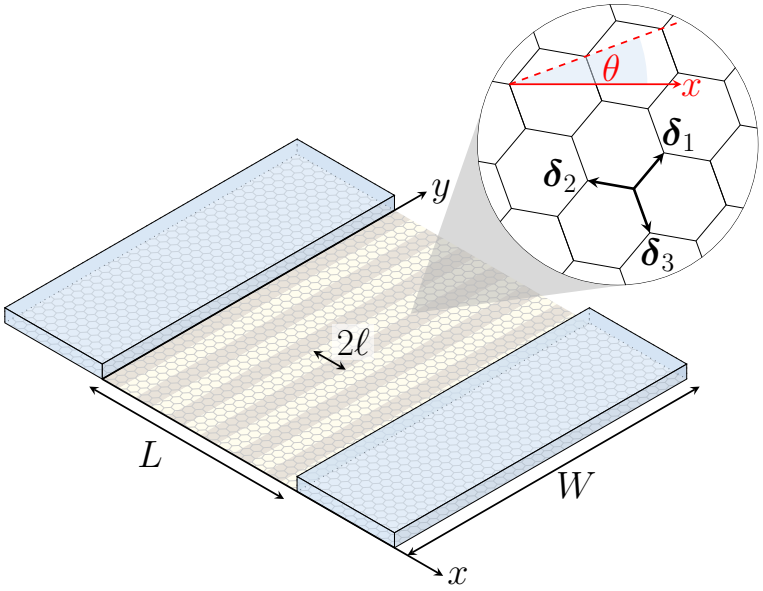

Figure 4.1: Schematic illustration of the graphene setup with metal leads for $x < 0$ and $x > L$. The angle θ specifies the orientation of the honeycomb lattice with respect to the transport direction x.

in Section 4.5. The results for conductance, shot-noise, and the density of states can be qualitatively understood on the basis of a band structure analysis, which is presented in Appendix 4.A. In Section 4.4.1 we discuss transport in the direction perpendicular to the strain modulation.

4.2 Strain induced potentials

The electromechanical coupling in deformed graphene membranes has been investigated theoretically by many authors [9, 10, 11, 12] following earlier publications on carbon nanotubes [13, 14, 15, 16]. The deformations affect the hopping integrals in the tight-binding description of graphene in two distinct ways: by changing the distance between carbon atoms and by tilting the electronic p_z-orbitals, which are responsible for conduction. However, for most cases of interest, the in-plane strains play the major role in determining the electronic properties of deformed graphene, while the tilting can be neglected.

The effects of in-plane strain are well captured by the tight-binding hamiltonian

$$\mathcal{H} = -\sum_{\boldsymbol{R}} \sum_{\alpha=1}^{3} [t + \delta t_\alpha(\boldsymbol{R})] \left(a^\dagger_{\boldsymbol{R}+\boldsymbol{\delta}_\alpha} b_{\boldsymbol{R}} + \text{h.c.} \right), \tag{4.1}$$

where the summation runs over the atomic positions, $\boldsymbol{R}$, of a honeycomb lattice, the annihilation operators $a_{\boldsymbol{R}}$ and $b_{\boldsymbol{R}}$ refer to the occupation of p_z-orbitals at the two non-equivalent positions, A and B, of the unit cell, and the three vectors $\boldsymbol{\delta}_\alpha$ shown in Fig. 4.1 are directed from a B-atom to its three nearest neighbors.

If the strain varies smoothly on atomic distances, the deviation of the hopping integral from its unperturbed value $t \approx 2.7\,\text{eV}$ in a perfect crystal can be parameterized as

$$\delta t_\alpha(\boldsymbol{R}) = (\beta t/a^2) \boldsymbol{\delta}_\alpha^{\mathrm{T}} \hat{u}(\boldsymbol{R}) \boldsymbol{\delta}_\alpha, \tag{4.2}$$

where $\beta = -\partial \ln t / \partial \ln a \approx 2$ and $\hat{u}(\boldsymbol{R})$ is the strain tensor of the graphene membrane.

The dimensionless strain tensor $\hat{u}$ describes a change in a metric that can be expressed as

$$d\ell^2 = d\ell_0^2 + 2u_{ij} \mathrm{d}s^i \mathrm{d}s^j, \tag{4.3}$$

where the summation over the spatial indices $i, j = x, y$ is assumed and the s_i are the vector components in the undeformed reference system (see [17] §1 for further technical details). The length elements $\mathrm{d}\ell_0^2 = \delta_{ij} \mathrm{d}s^i \mathrm{d}s^j$ and $\mathrm{d}\ell^2 = g_{ij} \mathrm{d}s^i \mathrm{d}s^j$ correspond to the metric δ_{ij} in the flat space and to the local metric g_{ij} in the membrane, respectively. In subsequent formulas we let conventionally $s^x = x$ and $s^y = y$. The graphene crystal withstands very large internal strains so that the values of the strain tensor elements may reach 20% [18].

Even though the strain tensor makes no reference to the crystal structure of graphene, the lattice symmetry is entering the hopping integral in Eq. (4.2) due to the vectors $\boldsymbol{\delta}_\alpha$, $\alpha = 1, 2, 3$. The slow variation of $\hat{u}(\boldsymbol{R})$ on the scale of the lattice spacing justifies the effective mass approximation, which is formulated in a generic reference frame shown in Fig. 4.1. In this frame we find

$$\boldsymbol{\delta}_\alpha = a \begin{pmatrix} \sin(\theta + \theta_\alpha) \\ -\cos(\theta + \theta_\alpha) \end{pmatrix}, \qquad \theta_\alpha = 2\pi\alpha/3, \tag{4.4}$$

while the positions of the two non-equivalent Dirac points in the reciprocal space are

given by

$$\boldsymbol{K}_{1,2} = \pm\frac{4\pi}{3a\sqrt{3}}\begin{pmatrix}\cos\theta\\ \sin\theta\end{pmatrix}. \tag{4.5}$$

Using the Fourier ansatz

$$a_{\boldsymbol{R}} = \sum_{s=1}^{2} e^{i\boldsymbol{K}_s\boldsymbol{R}} a_s(\boldsymbol{R}), \quad b_{\boldsymbol{R}} = \sum_{s=1}^{2} e^{i\boldsymbol{K}_s\boldsymbol{R}} b_s(\boldsymbol{R}), \tag{4.6}$$

we obtain, to the leading order in spatial gradients, the effective model

$$\mathcal{H} = \int d^2\boldsymbol{R}\ \Psi^\dagger_{\boldsymbol{R}}\left[-i\hbar v\boldsymbol{\sigma}\boldsymbol{\nabla} + \tau_z\boldsymbol{\sigma}\boldsymbol{A}_\theta(\boldsymbol{R})\right]\Psi_{\boldsymbol{R}}, \tag{4.7}$$

where $\hbar v = 3ta/2$, τ_z is the Pauli matrix in the valley space and the operators are arranged into the four-spinor

$$\Psi_R = \left(a_1, \quad e^{i\theta}b_1, \quad -e^{-i\theta}b_2, \quad a_2\right). \tag{4.8}$$

The vector field $\boldsymbol{A}_\theta = (A_{\theta x}, A_{\theta y})$ is real and its components are related to the strain tensor in a simple way,

$$A_{\theta x} - iA_{\theta y} = (\hbar v\beta/a)e^{3i\theta}(u_{xx} + 2iu_{xy} - u_{yy}). \tag{4.9}$$

In the derivation of the effective Hamiltonian (4.7) we neglected the velocity renormalization, which would appear as a correction of the order δt_α to the prefactor of the spatial gradients [19].

Unlike the usual vector potential, the vector field $\boldsymbol{A}_\theta$ preserves the time reversal symmetry of the Hamiltonian (4.7). It also exhibits the discrete rotational invariance of the honeycomb lattice. Indeed, the Hamiltonian (4.7) remains invariant under the rotation through the angle , $\theta = 2\pi/3$ while the rotation through the angle $\theta = \pi/3$ is equivalent to an interchange of valleys.

The effect of a constant uniaxial strain has been studied both theoretically [20, 21] and experimentally [22, 23] and falls beyond the scope of our consideration. If the constant uniaxial strain (in x direction) exceeds a certain critical value, the Dirac points merge and a band gap opens. It is predicted [20] that, for a crystal expanded uniformly in the zigzag direction ($\theta = 0$), the critical expansion takes on its minimal value ($\approx 23\%$), while uniaxial strain in armchair direction, $\theta = \pi/2$, never generates a gap. These predictions

await experimental verification.

The strain also induces an electrostatic potential due to a change of the on-site energies of the tight-binding model. This effect leads to the appearance of a scalar electrostatic potential, which has to be added to the effective Hamiltonian (4.7).

4.3 The transfer matrix approach

In this Section we adapt the transfer matrix approach introduced in Sec. 3.2 to transport through a deformed graphene sample with metallic leads. We take advantage of the effective single-particle Hamiltonian

$$H = -i\boldsymbol{\sigma}\boldsymbol{\nabla} + \tau_z \boldsymbol{\sigma}\boldsymbol{A}_\theta + V, \tag{4.10}$$

where the fictitious vector potential $\boldsymbol{A}_\theta$ is related to the strain tensor, $\hat{u}(\boldsymbol{R})$, by means of the relation (4.9), and the scalar field $V(\boldsymbol{R})$ describes strain-induced and external electrostatic potentials. In most of the intermediate expressions we let $\hbar v = 1$ for simplicity.

The metal leads are modeled by letting $V = -U_{\text{lead}}$ for $x < 0$ and $x > L$,[24] in Eq. (4.10). The vector potential is assumed to be zero in the leads. The width of the sample in y direction is denoted as W. The scattering off the metal leads are fully taken into account in the subsequent analysis.

The rectangular sample geometry makes it convenient to employ the Fourier transform in y,

$$\Psi_{\boldsymbol{R}} = \sum_q e^{iqy} \Psi_q(x), \tag{4.11}$$

where q is the quasiparticle momentum component parallel to the graphene-metal interface. The momentum takes on the quantized values, $q = q_n$, which depend on the boundary conditions in y direction, for example, $q_n = 2\pi n/W$ with integer n for periodic boundary conditions. In the limit $W \gg L$, which we assume below, the particular type of the boundary conditions is not important.

We also restrict our consideration to small energies, $|\varepsilon| \ll U_{\text{lead}}$, where the energy ε is measured with respect to the Dirac point. In this approximation we derive the equation

on the transfer matrix in the form [25]

$$\frac{\partial \mathcal{M}}{\partial x} = \left[\sigma_x(\hat{q} + \tau_z \hat{A}_{\theta y}) + i\sigma_z(\hat{V} - \varepsilon) + i\tau_z \hat{A}_{\theta x}\right] \mathcal{M}, \tag{4.12}$$

where we introduced matrix notation in Fourier (channel) space[1], e.g.

$$\hat{V}_{nm}(x) = \frac{1}{W} \int_0^W dy\, e^{i(q_n - q_m)y}\, V(x, y), \tag{4.13}$$

and $\hat{q}_{nm} = \delta_{nm} q_n$. The transfer matrix has the following structure in σ-space

$$\mathcal{M} = \begin{pmatrix} 1/\hat{t}'^{\dagger} & \hat{r}\hat{t}^{-1} \\ -\hat{t}^{-1}\hat{r}' & 1/\hat{t} \end{pmatrix}, \tag{4.14}$$

where $\hat{r}(\hat{r}')$ for $x = L$ is the matrix of reflection amplitudes for quasiparticles entering the sample from the left(right) lead. The matrices $\hat{t}$ and $\hat{t}'$ contain the corresponding transmission amplitudes. Then, the Landauer formula for the conductance can be cast in the following form

$$G = \frac{2e^2}{h} \mathrm{Tr}\, \hat{t}\hat{t}^{\dagger} = \frac{2e^2}{h} \mathrm{Tr}\, \left[\hat{\mathcal{M}}_{11}\hat{\mathcal{M}}_{11}^{\dagger}\right]^{-1}, \tag{4.15}$$

where the trace is referred to the valley and channel space and the symbol $\hat{\mathcal{M}}_{11}$ stands for the 11 block of the transfer matrix in σ-space.

The Hamiltonian (4.10) with vanishing electrostatic potential, $V = 0$, obeys the chiral symmetry $\sigma_z H \sigma_z = -H$, which is responsible for a non-Abelian Aharonov-Casher gauge invariance at zero energy [26],

$$\Psi_0' = e^{i\phi + \tau_z \sigma_z \chi} \Psi_0. \tag{4.16}$$

The spatially dependent phases ϕ and χ can be chosen in such a way that the zero-energy spectral equation $H\Psi_0 = 0$ is reduced to the Dirac equation, $-i\boldsymbol{\sigma}\boldsymbol{\nabla}\Psi_0' = 0$, with zero vector potential. This gauge transformation can be applied in the scattering approach in order to demonstrate that the presence of arbitrary vector potential has no effect on charge transport at the Dirac point as far as the contribution from edge states can be disregarded [27, 28].

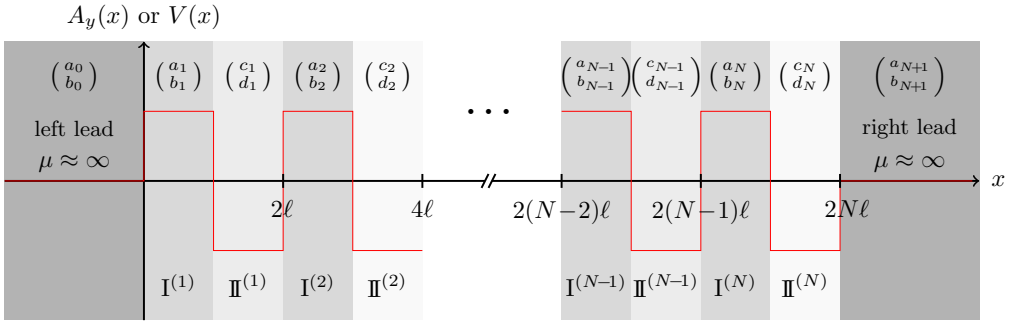

Figure 4.2: Sketch of the type of periodic potentials we consider in this section.

4.4 The Dirac-Kronig-Penney model

One-dimensional modulations of strain were realised experimentally in suspended graphene films using the remarkably large and negative thermal expansion of graphene[29]. Motivated by these experiments, we calculate the transport properties of the one-dimensional Dirac-Kronig-Penney model, which has been introduced earlier by several authors [30, 31, 32, 33]. Below we consider a general form of the model, where the variation of both electrostatic as well as vector potentials is included. Using the scattering approach formulated in the Section 4.3 we provide simple analytical solutions for transport and density of states in this model, which complement previous theoretical studies of Dirac Fermions in periodic potentials [34, 35, 36, 37, 38, 39, 40, 41, 42, 43, 44, 45].

A graphene sample with one-dimensional modulation of strain is characterized only by the component $u_{xx}(x)$ of the strain tensor, which depends solely on the x-coordinate. From Eq. (4.9), the components of the pseudo-vector potential take the form

$$A_{\theta x} = \frac{\beta u_{xx}}{a} \cos 3\theta, \qquad A_{\theta y} = -\frac{\beta u_{xx}}{a} \sin 3\theta\,. \tag{4.17}$$

In addition, the strain induces a spatial variation of the electrostatic potential, $V = V(x)$. Its relation to the strain tensor is, however, complicated by screening effects.

Since the potentials depend only on x, the transverse momentum q is conserved. In this case the matrices $\hat{V}$, $\hat{A}_{\theta x}$ and $\hat{A}_{\theta y}$ in Eq. (4.12) are diagonal in channel space. Since the considered potentials also do not couple the valleys, the scattering problem is reduced to

[1] Note that in this chapter we use symbols with a hat ($\hat{}$) to denote quantities in channel space (instead of the upright bold symbols used in the previous chapter).

the solution of 2×2 matrix equation,

$$\frac{\partial \mathcal{M}}{\partial x} = [\sigma_x(q + A_{\theta y}) - i\sigma_z(\varepsilon - V) + iA_{\theta x}]\,\mathcal{M}. \tag{4.18}$$

The x-component of the vector potential, $A_{\theta x}$, enters the equation in a trivial way and can be excluded by the gauge transformation , $\mathcal{M} \to \mathcal{M}\exp(i\int_0^x A_{\theta x}dx')$ which does not affect any observable. The first and the most trivial consequence of this transformation is that the one-dimensional strain modulations in the x-direction have no effect on transport in the zigzag direction ($\theta = 2\pi n/3$ with integer n) provided the effect of V is ignored.

For other angles the one-dimensional strain modulations lead to the appearance of new minima in the gate voltage dependence of the conductivity of the graphene sample. The numerical solution of Eq. (4.18) suggests that a periodic vector potential induces much more pronounced minima than a periodic scalar potential of equivalent amplitude. The weaker effect of V can be associated with Klein tunnelling, which leads to the suppression of pseudo-gaps in the spectrum of the superstructure.

In order to describe the effect of periodic potentials analytically we introduce the one-dimensional Dirac-Kronig-Penney model, which is characterized by the vector potential $\boldsymbol{A}$ given by Eq. (4.17) with

$$u_{xx}(x) = -u_0/2 + u_0 \sum_j \Theta(x - 2\ell j)\,\Theta((2j+1)\ell - x), \tag{4.19}$$

where the scale ℓ stands for half the period of the superlattice, $\Theta(x)$ is the Heaviside step function, and the dimensionless parameter u_0 specifies the amplitude of the strain modulation. The vector potential introduced by Eqs. (4.17,4.19) corresponds to a strain field which is smooth on atomic scale but changes abruptly on distances smaller than the Dirac quasiparticle wave length, $\hbar v/\varepsilon$. The periodic electrostatic potential is introduced in a similar manner,

$$V(x) = -V_0/2 + V_0 \sum_j \Theta(x - 2\ell j)\,\Theta((2j+1)\ell - x), \tag{4.20}$$

where V_0 is the amplitude of the modulation.

4.4.1 Transport properties

For the sake of simplicity, we consider a sample of length $L = 2\ell N$ with N being an integer. In this case, the solution to Eq. (4.18) satisfies $\mathcal{M}(L) = \mathcal{M}_0^N$, where $\mathcal{M}_0$ is the transfer matrix corresponding to the size of the supercell, 2ℓ. Disregarding the x-component of the vector potential, $A_{\theta x}$, which has been argued above to have no effect on transport, we write

$$\mathcal{M}_0 = \mathcal{M}_+\mathcal{M}_-, \qquad \mathcal{M}_\pm = e^{(q_\pm\sigma_x - i\varepsilon_\pm\sigma_z)\ell}, \tag{4.21}$$

where we take advantage of the definitions

$$q_\pm = q \pm (\beta u_0/2a)\sin 3\theta, \qquad \varepsilon_\pm = \varepsilon \pm V_0/2. \tag{4.22}$$

The eigenvalues of the transfer matrix, $\mathcal{M}_0$, are conveniently parameterized as

$$e^{\pm 2ik_0\ell} = \lambda \pm i\sqrt{1-\lambda^2}, \tag{4.23}$$

where we introduced the real function

$$\lambda = \cos k_+\ell\, \cos k_-\ell + \frac{q_+q_- - \varepsilon_+\varepsilon_-}{k_+k_-}\sin k_+\ell\, \sin k_-\ell, \tag{4.24}$$

with $k_\pm = (\varepsilon_\pm^2 - q_\pm^2)^{1/2}$ the x-component of the momenta. The wave number k_0 becomes imaginary for some values of q and ε indicating the appearance of pseudo-gaps in the superstructure. In the considered Dirac-Kronig-Penney model the value of k_0 is nothing but the x-component of the quasi-momentum in the reciprocal space associated with the superstructure.

In order to calculate the element $\mathcal{M}_{11}$ of the full transfer-matrix $\mathcal{M}(L)$ we use the Chebyshev identity to calculate the N-th power of an unimodular matrix [46]

$$\mathcal{M}_0^N = \frac{\mathcal{M}_0 \sin k_0 L - \sin k_0(L-2\ell)}{\sin 2k_0\ell}. \tag{4.25}$$

The matrix element $(\mathcal{M}_0)_{11} = \lambda - i\eta$ is readily determined from Eqs. (4.21,4.25) with

$$\eta = \frac{\varepsilon_-}{k_-}\sin k_-\ell\, \cos k_+\ell + \frac{\varepsilon_+}{k_+}\sin k_+\ell\, \cos k_-\ell. \tag{4.26}$$

Using the fact that both λ and η are real functions of the energy ε, and the conserved mo-

mentum component q, we obtain from Eqs. (4.14,4.25) the exact transmission probabilities for each value of q,

$$T_q = \left[\cos^2 k_0 L + \frac{\eta^2}{1-\lambda^2}\sin^2 k_0 L\right]^{-1}. \tag{4.27}$$

This expression is reduced to the well-known result for a purely ballistic system [24], i.e. for $u_0 = V_0 = 0$, by the substitution $\eta = (\varepsilon/k)\sin 2k\ell$ and $\lambda = \cos 2k\ell$. The transmission probabilities (4.27) determine the energy-dependent transport quantities

$$G = \frac{4e^2}{h}\sum_q T_q, \qquad F = \frac{\sum_q T_q(1-T_q)}{\sum_q T_q}, \tag{4.28}$$

where G is the Landauer conductance and F is the Fano factor for the shot noise. In the limit $W \gg L$ the summation over the scattering channels can be replaced by the integration, $\sum_q \to (W/2\pi)\int dq$.

More generally one can define the cumulant generating function for the transport,

$$\mathcal{F}(\chi) = \sum_q \ln(1 - T_q + e^{\chi}T_q). \tag{4.29}$$

The dimensionless cumulants $c_n = \lim_{\chi\to 0}\partial^n\mathcal{F}/\partial\chi^n$ determine the so-called full counting statistics of the charge transport. The conductance and the Fano factor are given by $G = (4e^2/h)c_1$ and $F = c_2/c_1$, respectively.

The strength of strain-induced and electrostatic potentials in the Dirac-Kronig-Penney model (4.19,4.20) is characterized by the dimensionless parameters

$$r_{\theta x} = (2u_0\ell/a)\sin 3\theta, \qquad r_0 = \ell V_0/\hbar v, \tag{4.30}$$

respectively. In Fig. 4.3, the conductance and the Fano factor in graphene with periodic modulations of strain calculated from Eq. (4.28) are plotted for systems with finite lengths $L = 20\ell$ and $L = 100\ell$ for $r_{\theta x} = 1$.

The energy dependence of conductance and Fano-factor (4.28) reveal fast Fabry-Pérot oscillations on the scale $\hbar v/L$. From a physics point of view, these oscillations originate from multiple reflections of propagating modes (real k_0) at the metal-graphene interfaces.

The channels with imaginary values of k_0 (evanescent modes or metal-induced states) also contribute to transport. Even though the individual contribution of each evanescent mode is exponentially small, $T_q \sim \exp(-2L\mathrm{Im}\, k_0)$, their combined effect becomes essential for

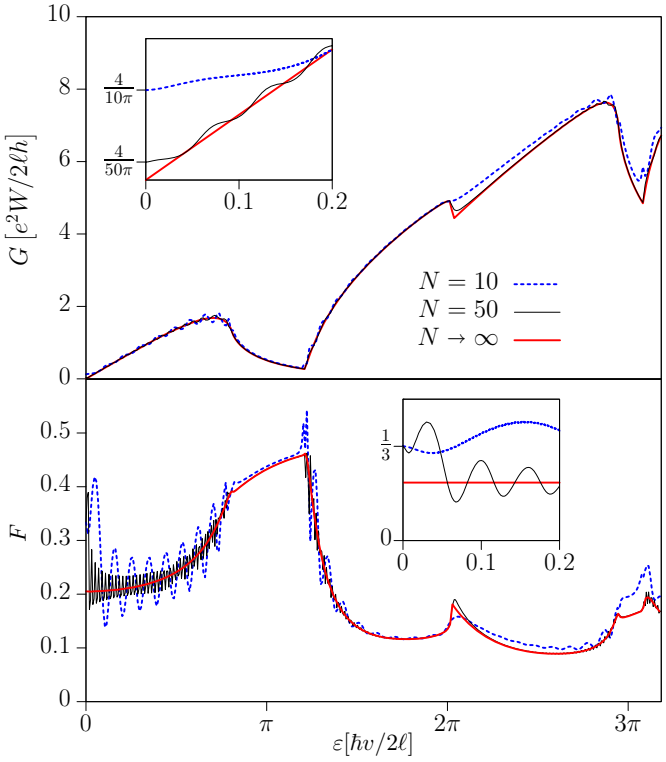

Figure 4.3: Conductance and Fano factor calculated from Eq. (4.28) for finite systems comprising $N = 10$ and $N = 50$ supercells (each having the length 2ℓ) are compared with the averaged expressions, to be derived in Eqs. (4.33,4.34), which correspond to the limit $N \to \infty$ and ignore contributions from evanescent modes. The plots are for graphene with strain modulations, $r_{\theta x} = 1$. In a small vicinity of the Dirac point, $\varepsilon \ll \hbar v/L$, (shown in the insets) the transport is insensitive to strain due to the extended gauge invariance (4.16) and is dominated by the evanescent modes.

energies in a vicinity of band-edges. The role of evanescent modes is especially important at the Dirac point due to the absence of propagating modes. Indeed, the conductance and the Fano-factor determined by (4.28) take on the values $G = 4e^2W/\pi hL$ and $F = 1/3$ for $\varepsilon \ll \hbar v/L$ irrespective of the vector potential. This universality is due to the extended gauge invariance (4.16).

For $N = L/2\ell \gg 1$, the amplitude of the Fabry-Pérot oscillations in G and F decreases (provided $W \gg L$) and the relative contribution of evanescent modes becomes less important. Taking the limit $N \to \infty$ is equivalent to ignoring the imaginary values of k_0 and averaging over the rapid phase, k_0L. This approximation has been used e.g. in Ref. [28] to obtain the full counting statistics of few-layer graphene.

The averaged generating function (4.29) takes the form

$$\overline{\mathcal{F}}(\chi) = 2\sum_q \ln\left(e^{\chi/2} + \sqrt{\overline{T}_q^{-2} + e^{\chi} - 1}\right), \tag{4.31}$$

where we introduce the mean transmission probability

$$\overline{T}_q = |\eta|^{-1}\mathrm{Re}\,\sqrt{1-\lambda^2}. \tag{4.32}$$

The averaged transport quantities do not depend on the system size L and reveal no Fabry-Pérot oscillations. For a ballistic sample, $u_0 = V_0 = 0$, one finds $\overline{T}_q^{\mathrm{ball}} = k/|\varepsilon|$, where $k = \sqrt{\varepsilon^2 - q^2}$ is the x-component of the momentum.

From the generating function (4.31) we readily find the averaged conductance and noise. The conductance is given by the Landauer formula,

$$\overline{G} = \frac{4e^2}{h}\sum_q \overline{T}_q, \tag{4.33}$$

while the Fano-factor is related to the averaged transmission probabilities in a less evident way

$$\overline{F} = \frac{\sum_q \overline{T}_q\left(1-\overline{T}_q^2\right)}{2\sum_q \overline{T}_q}. \tag{4.34}$$

The exact and averaged transmission probabilities (4.27,4.32) together with the corresponding expressions for the full counting statistics (4.29,4.34) provide the complete analytical description of the transport properties in the 1D-Dirac-Kronig-Penney model with scalar and vector potentials of arbitrary strength.

The dependence of the transmission coefficient on the transverse momentum component, q, is called the transmission spectrum. In Fig. 4.4 we plot the transmission spectra obtained from Eq. (4.32) for different strengths of the scalar and vector potentials.

The transmission spectra shown in Fig. 4.4 are qualitatively different for weak, $r_{\theta x} \ll 1$, and strong, $r_{\theta x} \gg 1$, strain modulations. It has to be stressed that the latter regime is well within the experimentally accessible range of parameters. Indeed, for an achievable strain modulation of 0.2% ($u_0 = 0.002$) and the period $\ell = 70\,\mathrm{nm}$ one finds $r_{\theta x} \approx 2$.

Neither the modulated strain nor the electrostatic field does open up a full band gap for any values of the parameters $r_{\theta x}$ or r_0. Nevertheless, very large pseudo-gaps are

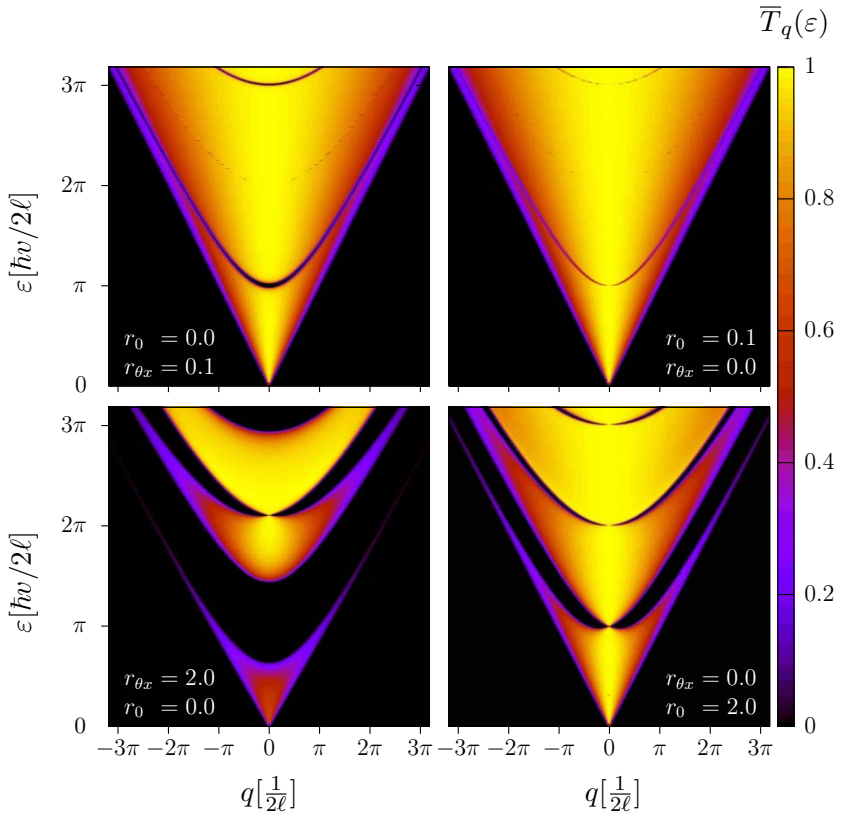

Figure 4.4: The colour plot of the averaged transmission probability, $\overline{T}_q(\varepsilon)$, as a function of the transverse momentum q and the energy ε. $\overline{T}_q(\varepsilon)$ was calculated using Eq. (4.32) for the Dirac-Kronig-Penney model with strain modulation $r_{\theta x} = 0.1$ (top left), $r_{\theta x} = 2.0$ (bottom left) and electrostatic field modulation $r_0 = 0.1$ (top right), $r_0 = 2.0$ (bottom right).

generated by strain modulations with $r_{\theta x} \gg 1$. One can see from the lower left panel in Fig. 4.4 that the charge transport in this regime is suppressed for almost all directions of the momenta (different q values) in a wide energy range. In contrast, the pseudo-gaps do not open at normal incidence ($q = 0$) in the Dirac-Kronig-Penney model with periodic electrostatic potential due to the Klein-tunnelling of quasiparticles through electrostatic barriers.[47]

The effects of strain and electrostatic field modulations on the conductance and noise are compared in Fig. 4.5. The most prominent feature of these plots are the dips in conductivity centered around the energies $\varepsilon_n = n\pi\hbar v/2\ell$ with $n = 1, 2, 3, \ldots$.

For $r_{\theta x} \gg 1$, the conductance is suppressed in wider energy intervals around $\varepsilon = \varepsilon_n$.

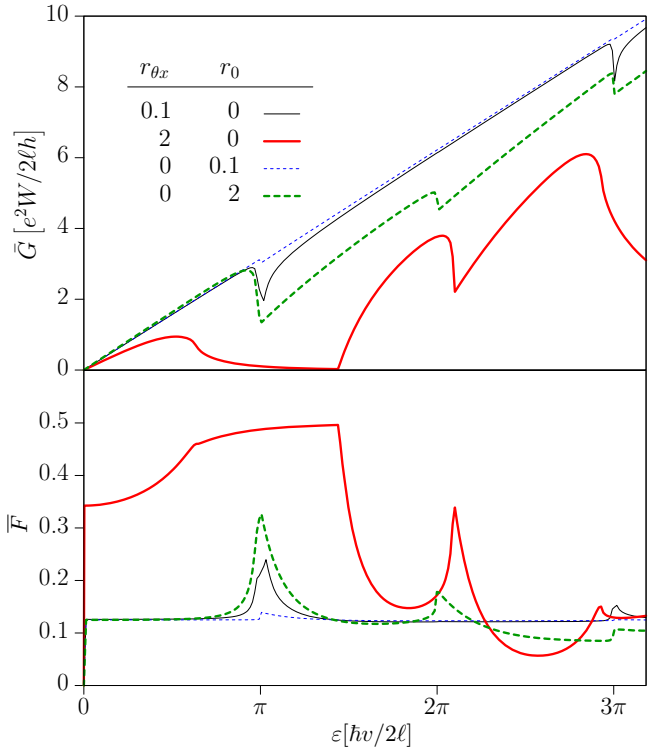

Figure 4.5: The averaged conductance and Fano factor calculated from Eqs. (4.33,4.34) for the one-dimensional Dirac-Kronig-Penney model with different field strengths (4.30). The effect of the scalar potential is suppressed due to Klein tunnelling through potential barriers.

For weak strain or potential amplitude, $r_{\theta x} \ll 1$ or $r_0 \ll 1$, significant pseudo-gaps are only located around the energy values ε_n with odd values of n, since only odd Fourier components of the potentials (4.19,4.20) exist. For a weak harmonic potential, a significant pseudo-gap would only arise around $\varepsilon = \varepsilon_1$.

The areas of vanishing transmission probability in Fig. 4.4 (top left) can be understood on the basis of perturbation theory as presented in Appendix 4.A for small amplitudes of periodic potentials. The pseudo-gap emerging due to a weak periodic strain is described by the functions $\varepsilon_{g-}(q)$ and $\varepsilon_{g+}(q)$ given in the first row of Tab. 4.1. These functions are shown with dashed lines in the upper panel of Fig. 4.6.

Inside the pseudo-gap, i.e. for $\varepsilon_{g-}(q) < \varepsilon < \varepsilon_{g+}(q)$, the transmission coefficient is exponentially small, while it is close to the ballistic value, $\overline{T}_q^{\text{ball}} = \sqrt{\varepsilon^2 - q^2}/|\varepsilon|$, outside the pseudo-gap (one can disregard the change in the resistance of the metal-graphene

	$\varepsilon_{g\pm}$	$\Delta(k_y=0)$
$A_{\theta xn}\neq 0$	$\sqrt{k_x^2+\left\lvert\frac{ng}{2}\right\rvert^2}\pm\lvert A_{\theta xn}\rvert$	0
$A_{\theta yn}\neq 0$	$\sqrt{k_y^2+\left\lvert\frac{ng}{2}\right\rvert^2}\pm\lvert A_{\theta yn}\rvert$	$2\lvert A_{\theta yn}\rvert$
$V_n\neq 0$	$\sqrt{k_y^2+\left\lvert\frac{ng}{2}\right\rvert^2+\lvert V_n\rvert^2\pm\lvert k_y\rvert\lvert V_n\rvert}$	0
$V_{zn}\neq 0$	$\sqrt{k_y^2+\left\lvert\frac{ng}{2}\right\rvert^2+\lvert V_{zn}\rvert^2\pm 2\lvert\frac{ng}{2}\rvert\lvert V_{zn}\rvert}$	$2\lvert V_{zn}\rvert$

Table 4.1: Energy value of the forbidden zone's upper/lower boundary, as well as the width of the gap in forward direction for the different types of periodic potentials. In the first row, $\boldsymbol{b}$ was chosen parallel to $\boldsymbol{e}_y$, for the remaining rows $\boldsymbol{b}\parallel\boldsymbol{e}_x$. For the derivation of the table's content see 4.A

interface due to the weak periodic potentials). Note further, that the pseudo-gap is located near $q=0$ for energies near the dip such that $\overline{T}_q^{\text{ball}}\approx 1$ in this region. We can, therefore, estimate the conductance in the vicinity of the lowest dip ($\varepsilon=\varepsilon_1$) by subtracting the contribution of ballistically propagating modes inside the pseudo-gap from the ballistic result as

$$G_{mc}=G_0-\frac{4e^2}{h}\sum_q\Theta(\varepsilon-\varepsilon_{g-}(q))\,\Theta(\varepsilon_{g+}(q)-\varepsilon), \tag{4.35}$$

where $\Theta(x)$ is the Heaviside step function, $G_0=e^2W\varepsilon/h$, and the limit $W|\varepsilon|\gg 1$ is assumed. The generalisation of Eq. (4.35) around the higher resonant energies, $\varepsilon=\varepsilon_n, n=3,5,\ldots$, is straightforward.

It is shown in Fig. 4.6 for $r_{\theta x}=0.3$ that the result of Eq. (4.35) agrees with the averaged conductance calculated from Eq. (4.33). The band-structure analysis (4.35) predicts characteristic dips in the conductance at $\varepsilon=n\pi\hbar v/2\ell, n=1,3,5\ldots$ of the depth $\delta G=(8e^2W/h\pi)\sqrt{|A_n|n\pi/2\ell}$, where A_n stands for n-th Fourier-component of the vector potential. For the Dirac-Kronig-Penney model one finds $A_n\propto 1/n$ hence the value of the conductance dip does not depend on n. We note that the validity of Eq. (4.35) is restricted to weak potentials. For $r_{\theta x}, r_0\gtrsim 1$, the pseudo-gaps overlap and the perturbation theory of Appendix 4.A is no longer applicable.

Transport in y direction

We have demonstrated that periodic and x-dependent scalar and vector potentials modify transport in x-direction due to the appearance of pseudo-gaps. Let us now argue that

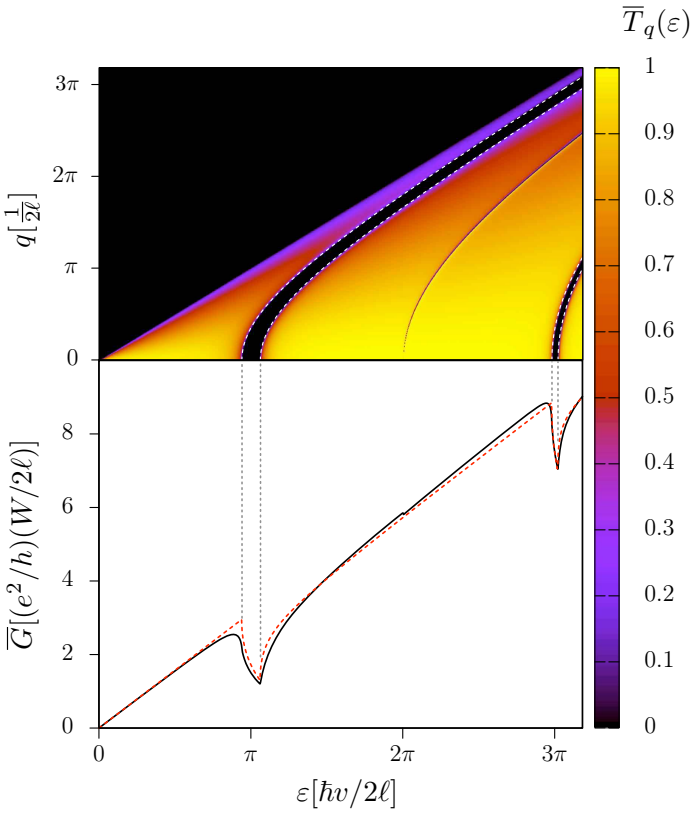

Figure 4.6: The averaged conductance as a function of the energy ε (solid line in the lower panel; calculated using Eq. (4.33)) is compared with an estimate (4.35) based on the mode-counting argument (dashed) for the Dirac-Kronig-Penney model with $r_{\theta x} = 0.3, r_0 = 0$. The upper panel shows the colour plot of the corresponding transmission spectrum that yields the conductance upon summing up $\overline{T}_q(\varepsilon)$ for all values of the transverse momentum q.

such potentials only weakly affect the transport in the y-direction (i.e. in the direction parallel to the equi-potential lines) in the sense that no pseudo-gaps are formed in this case.

In Fig. 4.7 we plot the Fermi surface slightly above the energy value $\varepsilon = \varepsilon_0$ using the exact dispersion relation, $\varepsilon = \varepsilon(k_0, q)$, obtained from Eqs. (4.23,4.24) for the Dirac-Kronig-Penney model. We have seen that the transport in x direction is dominated by the modes with the momenta $q \in (-\varepsilon, \varepsilon)$. For some values of q in this interval one cannot find any propagating states, which correspond to the real values of k_0. This can be seen as the formation of pseudo-gaps in the transmission spectra shown in Fig. 4.4, which is especially strong for $r_{\theta x}, r_0 \gtrsim 1$. In contrast, for each real value of k_0 one

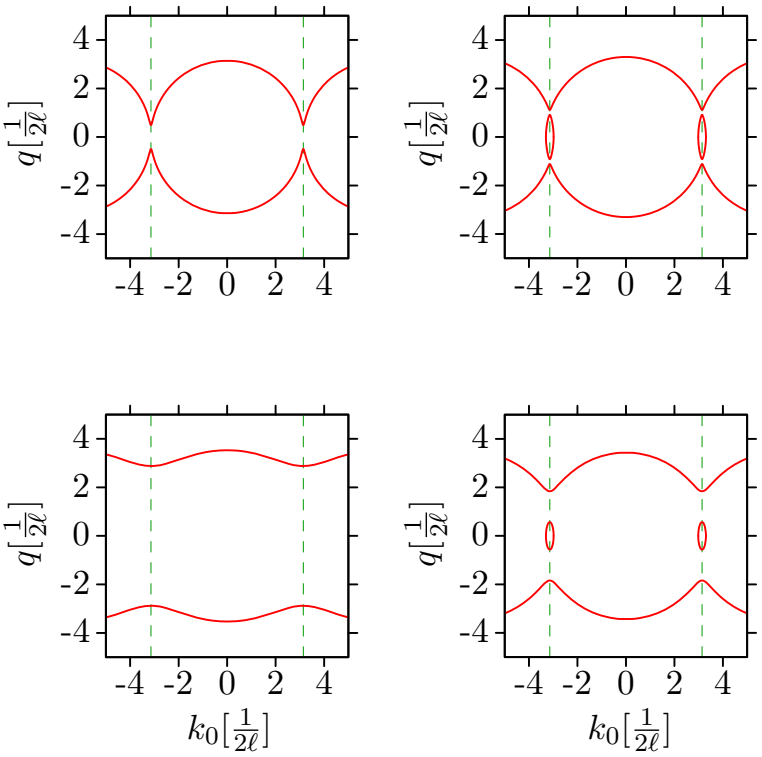

Figure 4.7: The contour plot of the dispersion relation for the Dirac-Kronig-Penney model (4.19,4.20) with strain modulation $r_{\theta x} = 0.3$ (top left), $r_{\theta x} = 2.0$ (bottom left) and electrostatic field modulation $r_0 = 0.3$ (top right), $r_0 = 2.0$ (bottom right) at energy $\varepsilon = 3.3\hbar v/2\ell$.

always finds real values of q. Therefore, the transport in y-direction is not affected by the formation of the pseudo-gaps, and depends only on the details of scattering at the metal-graphene interfaces. The latter effect is, however, weak and falls beyond the scope of our consideration. We therefore conclude that one-dimensional superlattices have a major impact only on the transport properties along the direction of their periodicity.

4.4.2 Density of states

Let us now extend the solution of the Dirac-Kronig-Penney model to the density of states. For purely ballistic system with metal leads, both the local and the integrated density has been found in Ref. [48] using a Green's function approach. Below we take advantage of an alternative route and relate the partial density of states in the channel q to the

corresponding transmission amplitude, t_q, by the well-known formula[49]

$$\nu_q = -\frac{1}{\pi}\mathrm{Im}\left[\frac{\partial \ln t_q}{\partial \varepsilon}\right]. \tag{4.36}$$

Then, the integrated density of states per unit volume is given by

$$\rho(\varepsilon) = \frac{4}{LW}\sum_q \nu_q(\varepsilon), \tag{4.37}$$

where the factor 4 takes into account the spin and valley degeneracy.

The transmission amplitude is readily obtained from Eqs. (4.14,4.25) as

$$t_q = \frac{1}{\cos k_0 L + i\zeta_q \sin k_0 L}, \qquad \zeta_q = \frac{\eta}{\sin 2k_0\ell}, \tag{4.38}$$

where the wave-number k_0 and the real quantity η are determined from the expressions (4.23) and (4.26), respectively. Therefore, the partial density of states can be calculated exactly as

$$\nu_q = \frac{L\zeta_q(dk_0/d\varepsilon) + \sin k_0 L\, \cos k_0 L\, (d\zeta_q/d\varepsilon)}{\pi\left(\cos^2 k_0 L + \zeta_q^2 \sin^2 k_0 L\right)}. \tag{4.39}$$

Unlike the conductance or the shot noise (4.28), the density of states depends on the value of U_{lead}, because the spectrum in a vicinity of the band-edges is dominated by the metal-induced states (evanescent modes).

The metal proximity effect[48] can be seen already for purely ballistic system near the Dirac point. Indeed, for $u_0 = V_0 = 0$, one finds

$$\nu_q^{\mathrm{ball}}(\varepsilon) = \frac{L\varepsilon^2 - (q^2/k)\cos kL\, \sin kL}{\pi(\varepsilon^2 - q^2\cos^2 kL)}, \tag{4.40}$$

where $k = \sqrt{\varepsilon^2 - q^2}$. At zero energy the ballistic result (4.40) is reduced to $\nu_q^{\mathrm{ball}}(0) = \tanh(qL)/\pi q$. Therefore, the density of states at $\varepsilon = 0$ in Eq. (4.37) acquires a logarithmic divergency. This divergency is regularized by the largest available transverse momentum $q_{\max}$, which is simply equal to the Fermi-momentum in the metal lead, $q_{\max} = U_{\mathrm{lead}}/\hbar v$. Thus, the density of states in a close vicinity of the Dirac point, $\varepsilon \ll \hbar v/L$, is given by

$$\rho^{\mathrm{ball}}(0) = \frac{4}{\pi^2 \hbar v L}\ln\frac{U_{\mathrm{lead}} L}{\hbar v}, \tag{4.41}$$

in agreement with Ref. [48]. Similar logarithmic dependence of the density of states on

U_{lead} takes place in the Dirac-Kronig-Penney model for energies inside the pseudo-gaps.

In full analogy with the averaged generating function (4.31) we can introduce the averaged density of states, $\overline{\rho}$, which corresponds to the limit $L \to \infty$. In this limit we disregard the contribution of the metal-induced states by projecting on the real values of the momentum k_0 and average the result of Eq. (4.40) over the rapid phase $k_0 L$. This procedure leads to the simple result

$$\overline{\nu}_q = \frac{L}{\pi} \left| \frac{d\mathrm{Re}\, k_0}{d\varepsilon} \right|, \tag{4.42}$$

hence, in the limit $W \gg L$, the mean density is given by

$$\overline{\rho} = \frac{2}{\pi^2} \int_{-\infty}^{\infty} dq \left| \frac{d\mathrm{Re}\, k_0}{d\varepsilon} \right|. \tag{4.43}$$

In the ballistic limit, $u_0 = V_0 = 0$, Eq. (4.43) yields the density of states of the clean graphene $\overline{\rho}^{\text{ball}} = 2|\varepsilon|/\pi\hbar^2 v^2$. In Fig. 4.8 we plot the averaged density of states calculated from Eq. (4.43) for different strengths of the periodic potentials.

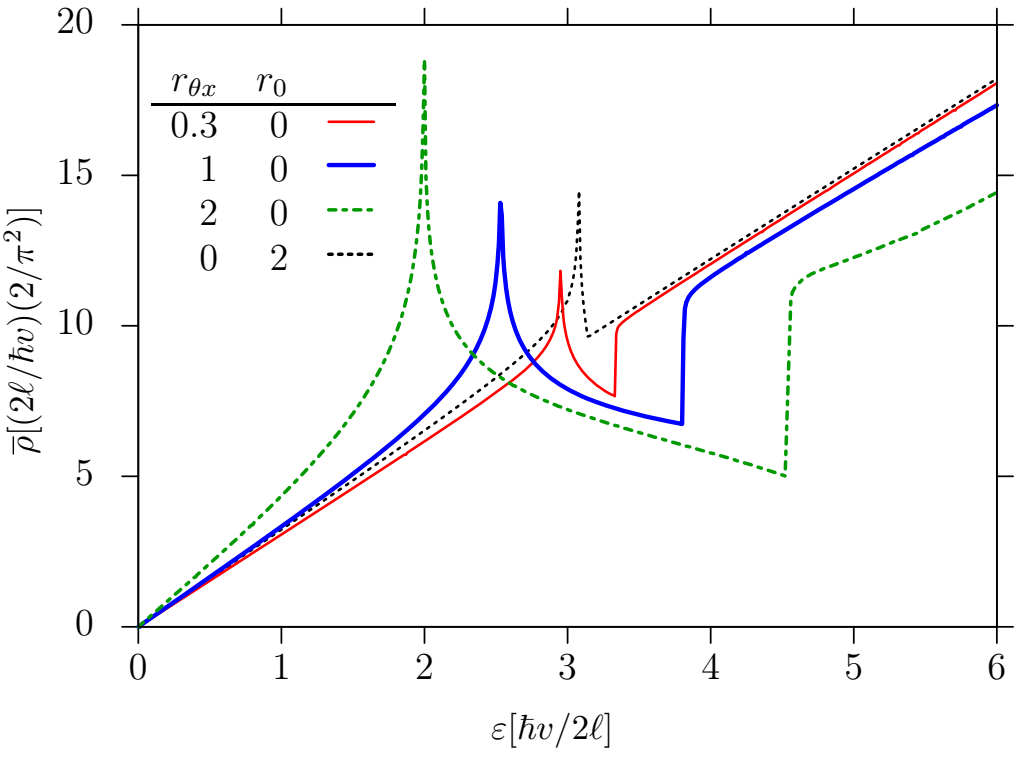

Figure 4.8: The averaged density of states obtained from Eq. (4.43) for the Dirac-Kronig-Penney model with different strengths of the periodic potentials.

4.5 Beyond the DKPM

The results of the previous subsections are readily generalized to a model with arbitrary periodic variation of strain and electrostatic potential in x direction. The analysis of the model is reduced to the calculation of the transfer matrix, $\mathcal{M}_0$, which corresponds to the wave propagation over the distance 2ℓ, the period of the potential. In this generalized model, both the exact and the averaged full counting statistics as well as the density of states are still given by the expressions (4.29,4.31,4.39,4.42) with

$$\lambda = \frac{1}{2}\mathrm{Tr}\,\mathcal{M}_0, \qquad \eta = \frac{i}{2}\mathrm{Tr}\,\sigma_z\mathcal{M}_0, \tag{4.44}$$

and the x-component, k_0, of the quasi-momentum is related to λ by Eq. (4.23). Thus, for a periodic potential of a general type, the full solution of the problem is reduced to the straightforward numerical evaluation of the functions λ and η. Note, that the exact analytical expressions (4.24,4.26) are restricted to the Dirac-Kronig-Penney model and do not apply generally.

We have used Eqs. (4.44) to calculate the energy-dependent conductance for different amplitudes of the periodic strain in the harmonic potential, $u_{xx} = u_0 \sin(\pi x/\ell)$. In this case, the higher pseudo-gaps are found to be suppressed for weak potentials $r_{\theta x}, r_0 \ll 1$ as compared to the Dirac-Kronig-Penney model. The lowest conductance minimum around $\varepsilon = \varepsilon_0$ is essentially the same in both models. The models become even more similar with increasing potential strength. For $r_{\theta x}, r_0 \gtrsim 1$ the transmission spectra of the single-harmonic model, becomes almost equivalent to those of the Dirac-Kronig-Penney model for all energies.

Appendices to Chapter 4

4.A Band structure in graphene superlattices

In this appendix (which is based, in parts, on unpublished notes by W. Belzig), the energy dispersion in the vicinity of the zone boundary is calculated perturbatively. Special attention is paid to the aspects that distinguish the calculation for graphene from the usual Schrödinger case.

We are interested in finding the eigenvalues of the equation

$$[-i\boldsymbol{\sigma}\cdot\boldsymbol{\nabla}+\mathcal{V}(\boldsymbol{r})]\,\Psi(\boldsymbol{r})=\varepsilon\Psi(\boldsymbol{r}), \qquad \text{Use units such that } \hbar v=1. \tag{4.45}$$

where $\mathcal{V}(\boldsymbol{r})$ denotes a matrix-valued potential

$$\mathcal{V}(\boldsymbol{r})=\begin{pmatrix} V(\boldsymbol{r})+V_z(\boldsymbol{r}) & A_{\theta x}(\boldsymbol{r})-iA_{\theta y}(\boldsymbol{r}) \\ A_{\theta x}(\boldsymbol{r})+iA_{\theta y}(\boldsymbol{r}) & V(\boldsymbol{r})-V_z(\boldsymbol{r}) \end{pmatrix} \equiv \begin{pmatrix} V+V_z & \mathrm{A}^* \\ \mathrm{A} & V-V_z \end{pmatrix} \tag{4.46a}$$

that is periodic with lattice vector $\boldsymbol{b}=(b_x,b_y)^{\mathrm{T}}$, i.e.

$$\mathcal{V}(\boldsymbol{r}+\boldsymbol{b})=\mathcal{V}(\boldsymbol{r}). \tag{4.46b}$$

Derivation of the central equation

In accordance with the Bloch theorem, we make the ansatz

$$\Psi(\boldsymbol{r})=\sum_n\ \psi_n(\boldsymbol{k})\ e^{i(\boldsymbol{k}-n\boldsymbol{g})\boldsymbol{r}} \tag{4.47}$$

for the wave function and write the potential as a Fourier series

$$\mathcal{V}(\boldsymbol{r})=\sum_n \mathcal{V}_n\ e^{in\boldsymbol{g}\boldsymbol{r}}. \tag{4.48}$$

In these expressions, n takes values in $\mathbb{Z}$, $\boldsymbol{k} = (k_x, k_y)^{\mathrm{T}}$ is a Bloch wave vector lying in the first Brillouin zone, and $\boldsymbol{g} = (g_x, g_y)^{\mathrm{T}}$ is the reciprocal lattice vector satisfying the relations $\boldsymbol{b} \cdot \boldsymbol{g} = 2\pi$ and $\boldsymbol{b} \parallel \boldsymbol{g}$. The level of zero energy is chosen such that $\mathcal{V}_0 = 0$.

Plugging Eqs. (4.47) and (4.48) into Eq. (4.45) yields

$$\begin{aligned} 0 &= \sum_{\boldsymbol{k}\in 1^{\mathrm{st}}\mathrm{BZ}} e^{i\boldsymbol{k}\boldsymbol{r}} \left[\sum_n (h_n - \varepsilon)\psi_n(\boldsymbol{k}) e^{-in\boldsymbol{g}\boldsymbol{r}} + \sum_{n,m} \mathcal{V}_m \psi_n(\boldsymbol{k}) e^{i(m-n)\boldsymbol{g}\boldsymbol{r}} \right] \\ &= \sum_{\boldsymbol{k}\in 1^{\mathrm{st}}\mathrm{BZ}} e^{i\boldsymbol{k}\boldsymbol{r}} \sum_n \mathrm{e}^{-in\boldsymbol{g}\boldsymbol{r}} \left[(h_n - \varepsilon)\psi_n(\boldsymbol{k}) + \sum_m \mathcal{V}_m \psi_{n+m}(\boldsymbol{k}) \right], \end{aligned} \qquad \text{Shifted summation index in the second summand by } m. \tag{4.49}$$

where we introduced the abbreviation

$$h_n = \begin{pmatrix} 0 & \mathrm{k}^* - n\mathrm{g}^* \\ \mathrm{k} - n\mathrm{g} & 0 \end{pmatrix}, \tag{4.50}$$

with $\mathrm{k} = k_x + ik_y$ and $\mathrm{g} = g_x + ig_y$. Because the $\exp[i(\boldsymbol{k} - n\boldsymbol{g})\boldsymbol{r}]$ are linearly independent, the square brackets have to vanish separately. Shifting the summation index again leads to the so-called *central equation* for the coefficients $\psi_n(\boldsymbol{k})$:

$$[h_n(\boldsymbol{k}) - \varepsilon]\, \psi_n(\boldsymbol{k}) + \sum_m \mathcal{V}_{m-n} \psi_m(\boldsymbol{k}) = 0. \tag{4.51}$$

Perturbative approach to calculate the band structure

When the periodic potential is switched off, $\psi_o^{(\pm)}(\boldsymbol{k}) \exp[i(\boldsymbol{k} - o\boldsymbol{g})\boldsymbol{r}]$ are possible solutions to Eq. (4.45) for some fixed Bloch vector $\boldsymbol{k}$ in the first Brillouin zone and some fixed integer (band index) o; their energies are $\pm|\mathrm{k} - o\mathrm{g}|$ and $\psi_o^{(\pm)}(\boldsymbol{k})$ denote the eigenvectors of $h_o(\boldsymbol{k})$ to these energy eigenvalues. When the periodic potential is switched on but stays 'small' (in a sense that will be become clear below), one expects that the solution will then be of the form Eq. (4.47) and that $\psi_n(\boldsymbol{k}), n \neq o$, will remain 'small' compared to $\Psi_o(\boldsymbol{k})$. To understand this better, consider the central equation

$$[\varepsilon - h_n(\boldsymbol{k})]\psi_n(\boldsymbol{k}) = \mathcal{V}_{o-n}\psi_o(\boldsymbol{k}) + \sum_{\substack{m \\ m\neq o}} \mathcal{V}_{m-n}\psi_m(\boldsymbol{k}) \tag{4.52}$$

for some $n \neq o$ and solve it for $\psi_n(\boldsymbol{k})$. This yields

$$\psi_n(\boldsymbol{k}) = \mathcal{W}_{o-n,n}\psi_o(\boldsymbol{k}) + \sum_{\substack{m \\ m\neq o}} \mathcal{W}_{m-n,n}\psi_m(\boldsymbol{k}) \tag{4.53a}$$

$$\text{with } \mathcal{W}_{m,n} = \frac{1}{\varepsilon^2 - |\mathrm{k} - n\mathrm{g}|^2} \begin{pmatrix} \varepsilon(V_m+V_{zm})+(\mathrm{k}^*-n\mathrm{g}^*)\mathrm{A}_m & \varepsilon\mathrm{A}^\star_m+(\mathrm{k}^*-n\mathrm{g}^*)(V_m-V_{zm}) \\ (\mathrm{k}-n\mathrm{g})(V_m+V_{zm})+\varepsilon\mathrm{A}_m & (\mathrm{k}-n\mathrm{g})\mathrm{A}^\star_m+\varepsilon(V_m-V_{zm}) \end{pmatrix}, \tag{4.53b}$$

where we introduced the somewhat clumsy though necessary notation $\mathrm{A}^\star_m = A_{\theta x,m} - iA_{\theta y,m}$, because A^* is in general different from $\sum_n \exp(in\boldsymbol{gr})(A^*_{\theta x,m} - iA^*_{\theta y,m})$. We find that the $|(\mathcal{W}_{m,n})_{ij}|$ will be small compared to 1 for 'sufficiently small potentials' $|(\mathcal{V}_m)_{ij}|$, so, indeed, $\psi_o(\boldsymbol{k})$ will remain much larger than the other coefficients. Therefore, the energy deviates from $|\mathrm{k} - o\mathrm{g}|$ by a term of second order in the perturbing potentials:

$$\left[\varepsilon - h_o(\boldsymbol{k}) - \sum_m \mathcal{V}_{m-o}\mathcal{W}_{m-o,m}\right]\Psi_o(\boldsymbol{k}) = 0. \tag{4.54}$$

Plugged Eq. (4.53a), neglecting there the sum, into Eq. (4.51).

Note that the expression 'sufficiently small potentials' should be understood as

$$|(\mathcal{V}_n)_{ij}| \ll \left|\frac{\varepsilon^2 - |\mathrm{k} - n\mathrm{g}|^2}{\max\left(|\varepsilon|, |\mathrm{k} - n\mathrm{g}|\right)}\right|, \tag{4.55}$$

and that this conditions cannot be satisfied when $\varepsilon^2 - |\mathrm{k} - n\mathrm{g}|^2$ vanishes. Then we are not able to compute ε by considering $\psi_o(\boldsymbol{k})$ alone (as in Eq. (4.54)) but are forced to also include all those $\psi_n(\boldsymbol{k})$ for which the condition (4.55) breaks down (but, fortunately, in good approximation only those).

To do this calculation in compact notation let us switch to the extended zone scheme where $\boldsymbol{k}$ is not restricted to the first Brillouin zone so we can set $o = 0$ without loss of generality. For simplicity, let us start with the case where the condition (4.55) fails for at most one value of n. We require that $|(\mathcal{V}_n)_{ij}| \ll |\mathrm{g}|$ and assuming that ε stays close $|\mathrm{k}|$, we expect this to happen in regions close to degeneracy: $|\mathrm{k}| \approx |\mathrm{k} - n\mathrm{g}|$ (see Fig. 4.A.1). Neglecting all small coeficients[2] $\psi_m(\boldsymbol{k})$ with $0 \neq m \neq n$, the central equation reduces to

$$[h(\boldsymbol{k}) - \varepsilon]\psi(\boldsymbol{k}) + \mathcal{V}_n\psi(\boldsymbol{k} - n\boldsymbol{g}) = 0 \tag{4.56a}$$

$$\mathcal{V}_{-n}\psi(\boldsymbol{k}) + [h(\boldsymbol{k} - n\boldsymbol{g}) - \varepsilon]\psi(\boldsymbol{k} - n\boldsymbol{g}) = 0. \tag{4.56b}$$

[2] Note that we do not need the $\mathcal{V}_m$ to decay rapidly with m as long the potentials are not too big: $|\mathcal{V}_{ij}| \ll |g|$. Then it is the smallness of the coefficients ψ_m compared to ψ_n, ψ_0 that prevents any potential apart from $\mathcal{V}_n$ to be important for the energy.

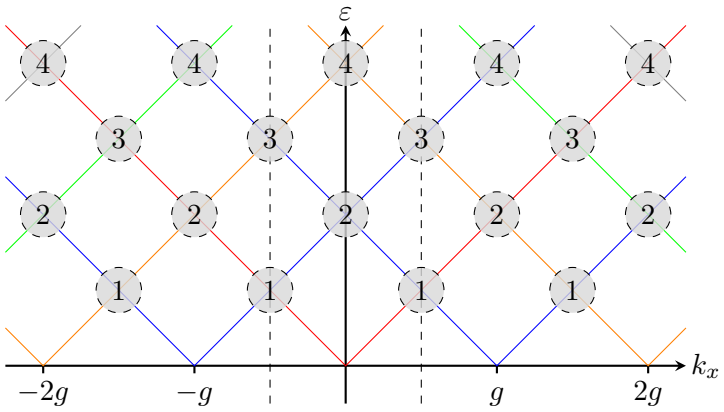

Figure 4.A.1: Free graphene dispersion in the repeated zone scheme for $\boldsymbol{b} \parallel \boldsymbol{e}_x$. (1), ..., (4) denote the first few regions of (approximate) degeneracy where gaps may be created in case a weak periodic potential is switched on.

Thus, the energy has to obey the equation

$$\begin{vmatrix} -\varepsilon & \mathrm{k}^* & V_n + V_{zn} & \mathrm{A}_n^\star \\ \mathrm{k} & -\varepsilon & \mathrm{A}_n & V_n - V_{zn} \\ V_n^* + V_{zn}^* & \mathrm{A}_n^* & -\varepsilon & \mathrm{k}_n^* \\ (\mathrm{A}_n^\star)^* & V_n^* - V_{zn}^* & \mathrm{k}_n & -\varepsilon \end{vmatrix} = 0. \qquad (4.57)$$

Used the relations $V_{-n} = V_n^*$ and $\mathrm{A}_{-n} = (\mathrm{A}_n^\star)^*$ following from $V, A_{\theta x}, A_{\theta y} \in \mathbb{R}$, and introduced $\mathrm{k}_n \equiv \mathrm{k} - n\mathrm{g}$.

The formula for the energy is particularly simple when only one of the coefficients $A_{\theta xn}, A_{\theta yn}, V_n$ or V_{zn} is different from zero [3]:

$$\varepsilon^2 = \frac{|\mathrm{k}|^2 + |\mathrm{k}_n|^2}{2} + |A_{xn}|^2 \pm \frac{1}{2}\sqrt{(|\mathrm{k}|^2 - |\mathrm{k}_n|^2)^2 + 4|A_{xn}|^2|2k_x - n\mathrm{g}|^2} \qquad (4.58a)$$

$$\varepsilon^2 = \frac{|\mathrm{k}|^2 + |\mathrm{k}_n|^2}{2} + |A_{yn}|^2 \pm \frac{1}{2}\sqrt{(|\mathrm{k}|^2 - |\mathrm{k}_n|^2)^2 + 4|A_{yn}|^2|2k_y - in\mathrm{g}|^2} \qquad (4.58b)$$

$$\varepsilon^2 = \frac{|\mathrm{k}|^2 + |\mathrm{k}_n|^2}{2} + |V_n|^2 \pm \frac{1}{2}\sqrt{(|\mathrm{k}|^2 - |\mathrm{k}_n|^2)^2 + 4|V_n|^2|2k - n\mathrm{g}|^2} \qquad (4.58c)$$

$$\varepsilon^2 = \frac{|\mathrm{k}|^2 + |\mathrm{k}_n|^2}{2} + |V_{zn}|^2 \pm \frac{1}{2}\sqrt{(|\mathrm{k}|^2 - |\mathrm{k}_n|^2)^2 + 4|V_{zn}|^2|n\mathrm{g}|^2}. \qquad (4.58d)$$

To check for possible gaps, we use that the wave functions on the boundaries of forbidden

[3] When $A_{\theta xn} \neq 0 \neq A_{\theta yn}$, for instance, the energy is given by the more complicated expression

$$\varepsilon^2 = \frac{|\mathrm{k}|^2 + |\mathrm{k}_n|^2}{2} + |A_{\theta xn}|^2 + |A_{\theta yn}|^2 \pm \frac{1}{2}\sqrt{f(\boldsymbol{k})}$$

with $f(\boldsymbol{k}) = (|\mathrm{k}|^2 - |\mathrm{k}_n|^2)^2 + 4(|\mathrm{k}|^2 + |\mathrm{k}_n|^2)(|A_{\theta xn}|^2 + |A_{\theta yn}|^2) + \mathrm{Im}\,(4A_{\theta xn}A_{\theta yn}^*)^2 + 8\mathrm{Re}\,(\mathrm{k}\,\mathrm{k}_n(|A_{\theta xn}|^2 - |A_{\theta yn}|^2 - 2i\mathrm{Re}\,A_{\theta xn}A_{\theta yn}^*))$

zones must have an eigenvalue of $\exp i\boldsymbol{k}\cdot\boldsymbol{b}=1$ with respect to the discrete translation operator of the superlattice, because it has to interpolate between propagating regions where this eigenvalue is complex and of modulus 1 and evanescent regions where it is purely real. We can achieve this by setting the component of $\boldsymbol{k}$ which is parallel to $\boldsymbol{b}$ to $n|\mathrm{g}|/2$:

- $A_{\theta xn}\neq 0, A_{\theta yn}=V_n=V_{nz}=0, \boldsymbol{b}\parallel\boldsymbol{e}_y$ (for $\boldsymbol{b}\parallel\boldsymbol{e}_x$ there is no gap), $k_y=n|\mathrm{g}|/2$

$$\begin{aligned} \text{gap boundary} &: \sqrt{k_x^2+\left|\frac{n\mathrm{g}}{2}\right|^2}\pm|A_{\theta xn}| && (4.59a)\\ \Delta(k_y=0) &= 0 && (4.59b)\end{aligned}$$

- $A_{\theta yn}\neq 0, A_{\theta xn}=V_n=V_{nz}=0, \boldsymbol{b}\parallel\boldsymbol{e}_x$ (for $\boldsymbol{b}\parallel\boldsymbol{e}_y$ there is no gap), $k_x=n|\mathrm{g}|/2$

$$\begin{aligned} \text{gap boundary} &: \sqrt{k_y^2+\left|\frac{n\mathrm{g}}{2}\right|^2}\pm|A_{\theta yn}| && (4.60a)\\ \Delta(k_y=0) &= 2|A_{\theta yn}| && (4.60b)\end{aligned}$$

- $V_n\neq 0, A_{\theta xn}=A_{\theta yn}=V_{nz}=0, \boldsymbol{b}\parallel\boldsymbol{e}_x$ (another choice of $\boldsymbol{b}$ would lead to analogous formulas), $k_x=n|\mathrm{g}|/2$

$$\begin{aligned} \text{gap boundary} &: \sqrt{k_y^2+\left|\frac{n\mathrm{g}}{2}\right|^2+|V_n|^2\pm|k_y||V_n|} && (4.61a)\\ \Delta(k_y=0) &= 0 && (4.61b)\end{aligned}$$

- $V_{zn}\neq 0, A_{\theta xn}=A_{\theta yn}=V_n=0, \boldsymbol{b}\parallel\boldsymbol{e}_x$ (another choice of $\boldsymbol{b}$ would lead to analogous formulas), $k_x=n|\mathrm{g}|/2$

$$\begin{aligned} \text{gap boundary} &: \sqrt{k_y^2+\left|\frac{n\mathrm{g}}{2}\right|^2+|V_{zn}|^2\pm 2|\frac{n\mathrm{g}}{2}||V_{zn}|} && (4.62a)\\ \Delta(k_y=0) &= 2|V_{zn}| && (4.62b)\end{aligned}$$

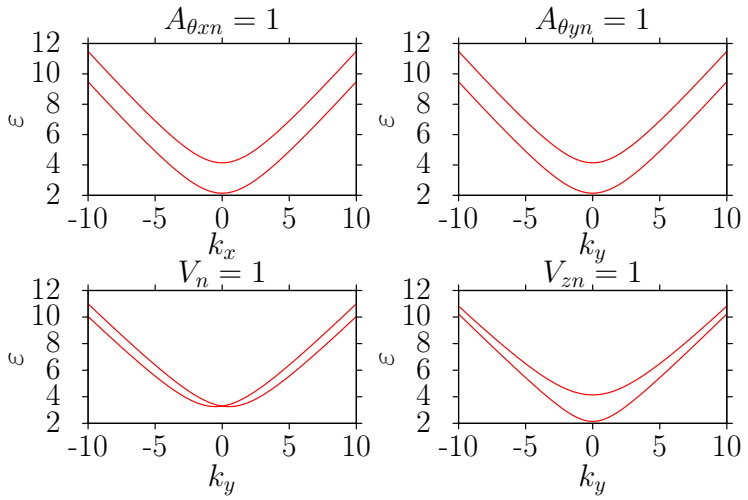

Figure 4.A.9: Typical band gap boundaries. In all plots n, b was set to 1.

References of Chapter 4

[1] Katsnelson, M. I. & Novoselov, K. S. Graphene: new bridge between condensed matter physics and quantum electrodynamics. *Solid State Communications* **143**, 3–13 (2007).

[2] Novoselov, K. S. *et al.* Electric field effect in atomically thin carbon films. *Science* **306**, 666–669 (2004).

[3] Novoselov, K. S. *et al.* Two-dimensional atomic crystals. *Proc.Nat.Acad.Sci.* **102**, 10451–10453 (2005).

[4] Pereira, V. M. & Neto, A. C. Strain engineering of graphene's electronic structure. *Physical Review Letters* **103**, 046801 (2009).

[5] Guinea, F., Geim, A. K., Katsnelson, M. I. & Novoselov, K. S. Generating quantizing pseudomagnetic fields by bending graphene ribbons. *Physical Review B* **81**, 035408 (2010).

[6] Guinea, F., Katsnelson, M. I. & Geim, A. K. Energy gaps and a zero-field quantum Hall effect in graphene by strain engineering. *Nature Physics* **6**, 30–33 (2009).

[7] von Oppen, F., Guinea, F. & Mariani, E. Synthetic electric fields and phonon

damping in carbon nanotubes and graphene. *Physical Review B* **80**, 075420 (2009).

[8] Gattenlöhner, S., Belzig, W. & Titov, M. Dirac-Kronig-Penney model for strain-engineered graphene. *Physical Review B* **82**, 155417 (2010).

[9] Morozov, S. V. *et al.* Strong suppression of weak localization in graphene. *Physical Review Letters* **97**, 016801 (2006).

[10] Guinea, F., Katsnelson, M. I. & Vozmediano, M. Midgap states and charge inhomogeneities in corrugated graphene. *Physical Review B* **77**, 075422 (2008).

[11] Kim, E. A. & Neto, A. Graphene as an electronic membrane - Abstract - EPL (Europhysics Letters) - IOPscience. *EPL (Europhysics Letters)* (2008).

[12] Isacsson, A., Jonsson, L. M., Kinaret, J. M. & Jonson, M. Electronic superlattices in corrugated graphene. *Physical Review B* **77**, 035423 (2008).

[13] Kane, C. L. & Mele, E. J. Size, Shape, and Low Energy Electronic Structure of Carbon Nanotubes. *Physical Review Letters* **78**, 1932–1935 (1997).

[14] Kleiner, A. & Eggert, S. Curvature, hybridization, and STM images of carbon nanotubes. *Physical Review B* **64**, 113402 (2001).

[15] Sasaki, K.-i., Kawazoe, Y. & Saito, R. Local energy gap in deformed carbon nanotubes. *Progress of theoretical physics* **113**, 463–480 (2005).

[16] Huertas-Hernando, D., Guinea, F. & Brataas, A. Spin-orbit coupling in curved graphene, fullerenes, nanotubes, and nanotube caps. *Physical Review B* **74**, 155426 (2006).

[17] Landau, L. D. & Lifshitz, E. M. *Theory of Elasticity.* Course of Theoretical Physics (Pergammon Press, London, 1970).

[18] Lee, C., Wei, X., Kysar, J. W. & Hone, J. Measurement of the Elastic Properties and Intrinsic Strength of Monolayer Graphene. *Science* **321**, 385–388 (2008).

[19] de Juan, F., Cortijo, A. & Vozmediano, M. A. Charge inhomogeneities due to smooth ripples in graphene sheets. *Physical Review B* **76**, 165409 (2007).

[20] Pereira, V. M., Neto, A. C. & Peres, N. Tight-binding approach to uniaxial strain in graphene. *Physical Review B* **80**, 045401 (2009).

[21] Fogler, M. M., Guinea, F. & Katsnelson, M. I. Pseudomagnetic fields and ballistic transport in a suspended graphene sheet. *Physical Review Letters* **101**, 226804 (2008).

[22] Kim, K. S. *et al.* Large-scale pattern growth of graphene films for stretchable transparent electrodes. *Nature* **457**, 706–710 (2009).

[23] Mohiuddin, T. *et al.* Uniaxial strain in graphene by Raman spectroscopy: G peak splitting, Grüneisen parameters, and sample orientation. *Physical Review B* **79**, 205433 (2009).

[24] Tworzydło, J., Trauzettel, B., Titov, M., Rycerz, A. & Beenakker, C. W. J. Sub-Poissonian Shot Noise in Graphene. *Physical Review Letters* **96** (2006).

[25] Titov, M. Impurity-assisted tunneling in graphene. *EPL (Europhysics Letters)* **79**, 17004 (2007).

[26] Aharonov, Y. & Casher, A. Ground state of a spin-1/2 charged particle in a two-dimensional magnetic field. *Physical Review A* **19**, 2461–2462 (1979).

[27] Schuessler, A., Ostrovsky, P., Gornyi, I. V. & Mirlin, A. D. Analytic theory of ballistic transport in disordered graphene. *Physical Review B* **79**, 075405 (2009).

[28] Hannes, W. R. & Titov, M. Ballistic charge transport in chiral-symmetric few-layer graphene. *EPL (Europhysics Letters)* **89**, 47007 (2010).

[29] Bao, W. *et al.* Controlled ripple texturing of suspended graphene and ultrathin graphite membranes. *Nature Nanotechnology* **4**, 562–566 (2009).

[30] Masir, M. R., Vasilopoulos, P. & Peeters, F. M. Magnetic Kronig–Penney model for Dirac electrons in single-layer graphene. *New Journal of Physics* **11**, 095009 (2009).

[31] Barbier, M., Vasilopoulos, P. & Peeters, F. M. Extra Dirac points in the energy spectrum for superlattices on single-layer graphene. *Physical Review B* **81**, 075438 (2010).

[32] Barbier, M., Vasilopoulos, P. & Peeters, F. M. Dirac electrons in a Kronig-Penney potential: Dispersion relation and transmission periodic in the strength of the barriers. *Physical Review B* **80**, 205415 (2009).

[33] Arovas, D. P., Brey, L., Fertig, H. A., Kim, E.-A. & Ziegler, K. Dirac spectrum in

piecewise constant one-dimensional (1D) potentials. *New Journal of Physics* **12**, 123020 (2010).

[34] Park, C.-H., Son, Y.-W., Yang, L., Cohen, M. L. & Louie, S. G. Electron beam supercollimation in graphene superlattices. *Nano Letters* **8**, 2920–2924 (2008).

[35] Park, C.-H., Son, Y.-W., Yang, L., Cohen, M. L. & Louie, S. G. Landau levels and quantum Hall effect in graphene superlattices. *Physical Review Letters* **103**, 046808 (2009).

[36] Park, C.-H., Yang, L., Son, Y.-W., Cohen, M. L. & Louie, S. G. Anisotropic behaviours of massless Dirac fermions in graphene under periodic potentials. *Nature Physics* **4**, 213–217 (2008).

[37] Dell'Anna, L. & De Martino, A. Multiple magnetic barriers in graphene. *Physical Review B* **79**, 045420 (2009).

[38] Snyman, I. Gapped state of a carbon monolayer in periodic magnetic and electric fields. *Physical Review B* **80**, 054303 (2009).

[39] Brey, L. & Fertig, H. A. Emerging zero modes for graphene in a periodic potential. *Physical Review Letters* **103**, 046809 (2009).

[40] Esmailpour, M., Esmailpour, A., Asgari, R., Elahi, M. & Tabar, M. R. R. Effect of a gap opening on the conductance of graphene superlattices. *Solid State Communications* **150**, 655–659 (2010).

[41] Wang, L.-G. & Zhu, S.-Y. Electronic band gaps and transport properties in graphene superlattices with one-dimensional periodic potentials of square barriers. *Physical Review B* **81**, 205444 (2010).

[42] Tan, L. Z., Park, C.-H. & Louie, S. G. Graphene Dirac fermions in one-dimensional inhomogeneous field profiles: Transforming magnetic to electric field. *Physical Review B* **81**, 195426 (2010).

[43] Park, C. H., Tan, L. Z. & Louie, S. G. Theory of the electronic and transport properties of graphene under a periodic electric or magnetic field. *Physica E: Low-dimensional Systems* (2011).

[44] Novikov, D. S. Electron properties of carbon nanotubes in a periodic potential.

Physical Review B **72**, 235428 (2005).

[45] Novikov, D. S. Devil's staircase of incompressible electron states in a nanotube. *Physical Review Letters* **95**, 066401 (2005).

[46] Born, M. & Wolf, E. *Principles of Optics*. Electromagnetic Theory of Propagation, Interference and Diffraction of Light (Cambridge University Press, Cambridge, 2002).

[47] Katsnelson, M. I., Novoselov, K. S. & Geim, A. K. Chiral tunnelling and the Klein paradox in graphene. *Nature Physics* **2**, 620–625 (2006).

[48] Titov, M. & Ostrovsky, P. Metallic proximity effect in ballistic graphene with resonant scatterers. *Semiconductor Science and and Technology* (2010).

[49] Buttiker, M. Capacitance, admittance, and rectification properties of small conductors. *Journal of Physics: Condensed Matter* **5**, 9361 (1993).

5 Electron transport in disordered graphene

We will now investigate the transport properties of graphene at charge neutrality when disordered by adatoms or scalar impurities. The contents of this chapter were partly published in Reference [1].

The present chapter is organised as follows. First, we give a very brief overview of the Altland-Zirnbauer scheme that classifies the possible symmetries of disordered systems (Section 5.1). The next two sections then describe how the results presented in this chapter were obtained. To that end, section 5.2 discusses the conductance formulas for undoped graphene samples with a given configuration of scalar impurities or adatoms; the details of computing the configuration-averaged conductivity are then outlined in section 5.3. The results are presented in sections 5.4 and 5.5. We first deal with the non-magnetic case (Section 5.4) and then consider the localisation behaviour in the magnetic case (Section 5.5).

5.1 The classification of disordered systems

The idea of classifying disordered systems according to their *symmetry* and *topology* will play a predominant role in what is to follow, so it seems advisable to begin this chapter by introducing the basic concepts and notations of the symmetry classification established by Zirnbauer and Altland [2, 3].

5.1.1 Symmetry

Following [4, 5], we will now classify Hamiltonians describing disordered systems of non-interacting fermions according to the following three generic symmetries: the time reversal symmetry (TRS), the particle-hole symmetry (PHS) and the chiral symmetry (CHS). The corresponding symmetry operators are described in Table 5.1.

NAME	SYMBOL	(ANTI-) UNITARITY	SYMMETRY CONDITION
Time reversal operator	$\mathcal{T}$	anti-unitary	$\mathcal{T}H\mathcal{T}^{-1} = \quad H$
Particle-hole operator	$\mathcal{C}$	anti-unitary	$\mathcal{C}H\mathcal{C}^{-1} = -H$
Chiral symmetry operator	$\mathcal{S} = \mathcal{T}\mathcal{C}$	unitary	$\mathcal{S}\,H\,\mathcal{S}^{-1} = -H$

Table 5.1: The three generic symmetry operators and some of their properties. The last column gives the conditions under which the respective operator is called a symmetry of the single particle Hamiltonian H.

Let us denote the symmetry group of the system we want to study by G and let $\mathcal{H}$, the Hilbert space on which the Hamiltonian H acts, be a representation of G. We like to separate G into two classes of symmetries by writing $G = G_0 \cup (G \setminus G_0)$, where G_0 shall consist of all those elements of G that are represented by unitary operators and commute with the Hamiltonian; the symmetries given in Table 5.1 clearly belong to the class $G \setminus G_0$. The point of this distinction is that it is always possible to construct a representation of G where the underlying Hilbert space decomposes into G_0-irreducible sectors with respect to which the Hamiltonian has block-diagonal form: this way, we can study the sub-blocks separately.[1] In the following, we assume that this technical simplification has been performed, i.e. without loss of generality we only consider the case $G_0 = \{\mathrm{Id}\}$.

A few comments on Table 5.1 are in order.

First, we shall draw the reader's attention to the extra minus sign in the last column for the PHS and the CHS. The presence of this extra minus sign directly follows from the fact that we are dealing with fermions (whose Fock space operators anti-commute). An important physical consequence of the minus sign is that the spectrum of a Hamiltonian with PHS or CHS must necessarily be mirror-symmetric.[2] In the graphene context this last observation means that for the particle-hole and the chiral symmetry to be important, the chemical potential has to be tuned (very close) to the Dirac point.

Second, being anti-unitary operators, $\mathcal{T}$ and $\mathcal{C}$ may either square to $+1$ or -1, whereas

[1] The case $G_0 = \mathrm{SO}(3)$ where the Hamiltonian does not mix states of different angular momentum is a typical example for this fact.

[2] To see that consider an eigenstate $|\Psi\rangle$ with $H|\Psi\rangle = \varepsilon|\Psi\rangle$; if H is particle-hole symmetric, then the condition $\mathcal{C}H\mathcal{C}^{-1} = -H$ enforces $\mathcal{C}|\Psi\rangle$ to be also an eigenvector of H but with eigenvalue $-\varepsilon$ (the same can be said on Hamiltonians obeying the chiral symmetry).

the unitary $\mathcal{S}$ has to square to unity. So with respect to the time reversal symmetry, any Hamiltonian has to satisfy one of the following conditions: '0' = (H does not have TRS), '+1'=(H has TRS and $\mathcal{T}^2 = +1$), or '−1'=(H has TRS and $\mathcal{T}^2 = -1$). For the particle-hole symmetry, there are three analogous possibilities, while for the case of the chiral symmetry, there are only the two possibilities of the symmetry being either present or absent. There are in total ten different ways a Hamiltonian can behave with respect to these possibilities (there are three options for the TRS and three independent options for the PHS; being the product of $\mathcal{T}$ and $\mathcal{C}$, the choice for the CHS is already fixed by the previous ones in all but the situation where both the TRS and the PHS are absent). These ten possibilities are listed in Table 5.2.

	CARTAN LABEL	TRS	PHS	SLS	$\{e^{-iHt/\hbar}\}$ (SYMMETRIC SPACE)
Wigner-Dyson classes	A	0	0	0	$\mathrm{U}(N) \times \mathrm{U}(N)/\mathrm{U}(N) = \mathrm{U}(N)$
	AI	+1	0	0	$\mathrm{U}(N)/\mathrm{O}(N)$
	AII	−1	0	0	$\mathrm{U}(2N)/\mathrm{Sp}(2N)$
chiral classes	AIII	0	0	1	$\mathrm{U}(p+q)/\mathrm{U}(p) \times \mathrm{U}(q)$
	BDI	+1	+1	1	$\mathrm{SO}(p+q)/\mathrm{SO}(p) \times \mathrm{SO}(q)$
	CII	−1	−1	1	$\mathrm{Sp}(2p,2q)/\mathrm{Sp}(2p) \times \mathrm{Sp}(2q)$
Bogoliubov-deGennes classes (BdG)	D	0	+1	0	$\mathrm{Sp}(2N) \times \mathrm{Sp}(2N)/\mathrm{Sp}(2N) = \mathrm{Sp}(2N)$
	C	0	−1	0	$\mathrm{Sp}(2N)/U(N)$
	DIII	−1	+1	0	$\mathrm{SO}(N)$
	CI	+1	−1	0	$\mathrm{SO}(2N)/\mathrm{U}(N)$

Table 5.2: The ten generic symmetry classes according to Altland and Zirnbauer [2, 3]. The table employs the notation from Ref. [5] where the entry '0' means that the respective symmetry is absent, while the entry '±1' states that the respective symmetry is present and the operator realising the symmetry squares to ±1.

It is remarkable that for each of the ten symmetry classes, the set of corresponding time-evolution operators, $\{\exp[-iHt/\hbar] \mid H$ belonging to the symmetry class$\}$, can be written in the form G/K (where G is a Lie group and K a subgroup of G). Spaces of this form are called symmetric spaces[3] and have a very rich mathematical structure (for instance they are Riemannian spaces with a covariantly constant curvature so they can

[3]There are some additional requirements on K guaranteeing that it is maximal in the sense that there exists no larger subgroup of G, see [6], Sec. IV.B for details, but these requirements are all satisfied for the K's above.

be thought of as generalised spheres). As there are exactly ten such symmetric spaces (a fact established by E. Cartan who also chose to label them as given in the table), this one-to-one correspondence of symmetry classes and symmetric spaces lead Zirnbauer et al. ([2, 3]) to conjecture that this classification is complete. Indeed, a mathematically rigorous proof for this statement was provided in Ref. [7].

To provide some intuition on what it means for a disordered Hamiltonian to belong to one of the chiral classes, it is helpful to note that this is the case if and only if one can find a basis where H takes the form (see [6] Sec IV. C)

$$H = \begin{pmatrix} 0 & h \\ h^\dagger & 0 \end{pmatrix}, \tag{5.1}$$

and therefore satisfies the symmetry $\tau_z H \tau_z = -H$ where τ_z is the third Pauli matrix in some isospin space. From this viewpoint one can easily see that this group of symmetry classes is prototypically realised in bipartite lattice with a nearest-neighbour-hopping what both explains why this symmetry is sometimes referred to as 'sublattice symmetry' (e.g. in [5]) and why the corresponding operator was called $\mathcal{S}$ (as in $\mathcal{S}$ublattice).

Similarly, Hamiltonians of the Bogoliubov-de Gennes class can be brought to the form (see [6] Sec. IV D for details)

$$H = \begin{pmatrix} h & \Delta \\ -\Delta^* & -h^T \end{pmatrix}, \qquad h = h^\dagger, \qquad \Delta = -\Delta^T, \tag{5.2}$$

in some basis what justifies the name given to this group of symmetry classes since Hamiltonians of this type are prototypically found in superconducting systems governed by the Bogoliubov-de Gennes equation.

In Table 5.3, an overview is given of the symmetry classes realised by the disorder studied in this chapter.

5.1.2 Topology

It has been appreciated only relatively recently that knowing the symmetry of a disordered system is not fully sufficient to understand its localisation behaviour and that the missing ingredient to a better description is the knowledge of its topology. Indeed, while it is 'text book knowledge' that all states are localised in two spatial dimensions [sic!], nine of

	CARTAN LABEL	REALISED IN THIS CHAPTER BY
Wigner-Dyson classes	A	non-resonant scalar impurities ($B \neq 0$), non-resonant adatoms at ($B \neq 0$)
	AI	non-resonant adatoms ($B = 0$)
	AII	non-resonant scalar impurities ($B = 0$)
chiral classes	AIII	vacancies ($B \neq 0$)
	BDI	vacancies ($B = 0$)
	CII	—
Bogoliubov-deGennes classes (BdG)	D	—
	C	—
	DIII	resonant scalar impurities ($B = 0$)
	CI	—

Table 5.3: Six of the ten symmetry classes are realised by the disordered graphene systems studied in this chapter.

the ten symmetry class can actually escape localisation and in many of these cases this can be explained by the presence of a topological term in the field-theoretic description of the disordered system, the NLσM [6, 8].

While we will come back to this topic in many places of this chapter, we will not go into the details of the connection between topology and the localisation behaviour here, as this would be beyond the scope of this thesis, and refer to the review articles [6, 8] for the details, instead.

5.2 Conductance in the presence of scalar impurities or adatoms

We have seen in Section 3.5 that the generating function $\mathcal{F}$, whose Taylor coefficients encode the full-counting-statistics of charge transport, changes by the amount

$$\delta\mathcal{F} = \mathrm{Tr}\,\ln\left(1 - \hat{T}\hat{\mathcal{G}}_{\mathrm{reg}}\right) \tag{5.3}$$

when the clean system is perturbed by the presence of N_{imp} finite range scatterers. In above expression, $\hat{T}$ is a diagonal, $N_{\mathrm{imp}} \times N_{\mathrm{imp}}$-dimensional matrix in the impurity

space which describes the scattering properties of the individual scatterers in an infinite graphene sample. The entries of this matrix are in general matrix-valued, acting on the four-dimensional pseudo-spin⊗valley-space if we restrict ourselves to s-wave scattering, and are called (integrated) T-matrices. Once this deviation of the generating function is known, the deviation of the conductance can be calculated using the relation

$$\delta \mathrm{G} = \frac{4e^2}{h} \frac{\partial^2 \delta \mathcal{F}}{\partial \phi^2}\bigg|_{\phi=0}. \tag{5.4}$$

In the following, we will consider two impurity types: First, we will look at 'scalar impurities' which is the name we want to give to scatterers whose integrated T-matrix is proportional to the unit matrix $\mathbb{1}_{\sigma\otimes\tau}$ (they act as scalars in pseudo-spin⊗valley-space, hence the name). After that, we will discuss adatoms that can each be modelled by an isolated on-site potential at the tight-binding level. Because such a potential mixes the two valleys and distinguishes between the two sublattices, the integrated T-matrix, which is used for its continuum description, acquires a non-trivial structure in pseudo-spin⊗valley-space. This impurity type includes the limiting case of an infinite on-site potential, where the scatterer can be interpreted as a vacancy.

5.2.1 Scalar impurities

To specify a concrete configuration of N_{imp} scalar impurities, one has to provide the following $3N_{\mathrm{imp}}$ numbers:

- the impurities' x-coordinates $x_1, \ldots, x_{N_{\mathrm{imp}}}$ each taken from the open interval $(0, L)$,
- their y-coordinates $y_1, \ldots, y_{N_{\mathrm{imp}}}$ each taken from the open interval $(0, W)$,
- and their strength parametrised by the scattering lengths $\ell_{s1}, \ldots, \ell_{sN_{\mathrm{imp}}}$.

The impurity coordinates enter Eq. (5.3) via $\hat{\mathcal{G}}_{\mathrm{reg}}$ whose components are given by the regularised Green's function evaluated at these coordinates. The impurity strengths can be encoded into the T-matrix

$$(\hat{T})_{nn} = 2\pi(\hat{\ell}_s)_{nn}\mathbb{1}_{\sigma\otimes\tau}. \tag{5.5}$$

where $\hat{\ell}_s = \mathrm{diag}\,(\ell_{s1}, \ldots, \ell_{sN_{\mathrm{imp}}})$. Reference [9] calculates the scattering length for a particular realisation of scalar impurities: a gate-defined quantum dot modelled as a rotationally symmetric square potential of strength V_0 and radius a_{dot}. The authors find that far away from any resonance, the scattering length is of the order $V_0 a_{\mathrm{dot}}^2/\hbar v$, while at

resonance (realised for certain pairs of a_{dot} and V_0), it has an infinite magnitude. For the purpose of this thesis, we will abstract away from these details and will simply assume that the scattering lengths are given parameters taking values in $(-\infty, \infty)$. Plugging the T-matrix (5.5) into Eq. (5.3) followed by evaluating Eq. (5.4) yields (the details of the intermediate steps can be found in the supplemental materials of Reference [1]):

$$G = \frac{4e^2}{\pi h}(W/L + \pi S_{\text{scalar}}), \tag{5.6a}$$

where

$$S_{\text{scalar}} = 4\text{Tr}\left[\hat{Y}_s^\dagger \hat{M}_+ \hat{Y}_s \hat{M}_- - \hat{Y}^2 \hat{M}_+ \hat{M}_-\right] \tag{5.6b}$$

$$\hat{Y}_s = \hat{Y} + i\hat{\ell}_s\sigma_y/2L, \qquad \hat{Y} = L^{-1}\text{diag}(y_1, y_2, \ldots, y_{N_{\text{imp}}}) \tag{5.6c}$$

$$\hat{M}_\pm = (1 \pm i\pi\hat{\ell}_s\hat{R}/2L)^{-1} \tag{5.6d}$$

$$R_{nm} = e^{\chi(\boldsymbol{r}_n)\sigma_z}\begin{pmatrix} \frac{1}{\sin(z_n+z_m^*)} & \frac{1-\delta_{nm}}{\sin(z_n-z_m)} \\ \frac{1-\delta_{nm}}{\sin(z_n^*-z_m^*)} & \frac{1}{\sin(z_n^*+z_m)} \end{pmatrix} e^{\chi(\boldsymbol{r}_m)\sigma_z}, \qquad z_n = x_n + iy_n \tag{5.6e}$$

$$\chi(\boldsymbol{r}) = x(L-x)/2\ell_B^2. \tag{5.6f}$$

5.2.2 Adatoms

To specify a configuration of N_{imp} on-site adatoms, one needs to provide $5N_{\text{imp}}$ numbers:

- the adatoms' x-coordinates $x_1, \ldots, x_{N_{\text{imp}}}$ each taken from the open interval $(0, L)$,
- their y-coordinates $y_1, \ldots, y_{N_{\text{imp}}}$ each taken from the open interval $(0, W)$,
- their scattering lengths $\ell_{a1}, \ldots, \ell_{aN_{\text{imp}}}$,
- their colours $c_1, \ldots, c_{N_{\text{imp}}}$ which are related to the Bloch phase at the impurity site (each c_n taking a value in $\{-1, 0, 1\}$),
- and their sublattice indices $\zeta_1, \ldots, \zeta_{N_{\text{imp}}}$, where $\zeta = 1$ for adatoms on the A-sublattice and $\zeta = -1$ for adatoms on the B-sublattice.

The impurity coordinates enter Eq. (5.3) via $\hat{\mathcal{G}}_{\text{reg}}$ whose components are given by the regularised Green's function evaluated at these coordinates. The adatoms' scattering

properties are described by the T-matrix

$$(\hat{T})_{mn} = \delta_{mn}(\hat{\ell}_a)_{nn} \begin{cases} \begin{pmatrix} 1 & 0 & 0 & e^{-i(\hat{\theta}^c_+)_{nn}} \\ 0 & 0 & 0 & 0 \\ 0 & 0 & 0 & 0 \\ e^{i(\hat{\theta}^c_+)_{nn}} & 0 & 0 & 1 \end{pmatrix}, & (\hat{\zeta})_{nn} = +1, \\ \begin{pmatrix} 0 & 0 & 0 & 0 \\ 0 & 1 & e^{-i(\hat{\theta}^c_+)_{nn}} & 0 \\ 0 & e^{i(\hat{\theta}^c_+)_{nn}} & 1 & 0 \\ 0 & 0 & 0 & 0 \end{pmatrix}, & (\hat{\zeta})_{nn} = -1, \end{cases} \tag{5.7}$$

where

$$\theta^c_\pm = \pm\alpha + 2\pi c/3, \tag{5.8}$$

and α denotes the angle between the x-axis and the armchair direction of the lattice. The derivation of this T-matrix is described in detail in Section 5.A.

Plugging the T-matrix (5.7) into Eq. (5.3) followed by evaluating Eq. (5.4) yields the following expression for the conductance (the details of the intermediate steps can be found in the supplemental materials of Reference [1]):

$$G = \frac{4e^2}{\pi h}(W/L + \pi S_{\text{adatoms}}), \tag{5.9a}$$

where

$$S_{\text{adatoms}} = \text{Tr}\left\{[\hat{Y}, \hat{Q}_+][\hat{Y}, \hat{Q}_-] + \hat{Q}_+[\hat{Y}, \hat{\Gamma}_+]\hat{Q}_-[\hat{Y}, \hat{\Gamma}_-] + \hat{Q}_+[\hat{Y}, \hat{\Gamma}_-]\hat{Q}_-[\hat{Y}, \hat{\Gamma}_+]\right\} \tag{5.9b}$$

$$\hat{\Gamma}_\pm = (i\hat{\ell}_a/8L)\hat{\zeta}\hat{A}_\pm \tag{5.9c}$$

$$\hat{Q}_\pm = [1 \pm (\hat{\Gamma}_+ + \hat{\Gamma}_-)]^{-1} \tag{5.9d}$$

$$(\hat{A}_\pm)_{nm} = \frac{e^{\pm(\zeta_n\chi(x_n)+\zeta_m\chi(x_m)+i(\theta_n-\theta_m)/2)}}{\sin\frac{\pi}{2L}\left[\zeta_n x_n + \zeta_m x_m + i(y_n - y_m)\right]}. \tag{5.9e}$$

5.3 Numerical simulation of the configuration-averaged conductivity

In this section we briefly describe the numerical procedure that will be used to compute the configuration-averaged longitudinal conductivity, $\langle \sigma_{xx} \rangle = \langle G \rangle \, L/W$, in the following sections.[4] The general idea is to let a random number generator produce a concrete disorder configuration, calculate the conductance for this configuration (using the formulas (5.6) and (5.9) given in Sec. 5.2) and repeat this step N_{samples} many times to compute the conductance average and its standard deviation (for the data shown in this chapter, N_{samples} was typically between 500 and 2000).

We shall close this section with a few comments on the choice of the aspect ratio and on how the evaluation of above conductance formulas was actually implemented on a computer.

Concerning the first point, we note that while a dependence of the conductivity on the aspect ratio can be observed when W/L is close to one or smaller, this dependency becomes negligible at larger values of the aspect ratio. Preliminary checks for both impurity types showed that a value of $W/L = 4$ is sufficiently large for that to be the case and so this value was chosen for all the samples studied in this chapter.

The formulas (5.6) and (5.9) are implemented in C++ using the standard algorithm of Gaussian elimination with full pivoting to perform matrix inversion (as described in [10]). To deal with numerical instabilities, the code allows the usage of arbitrary precision floating point numbers employing the GNU mpfr package (`www.mpfr.org`).

5.4 Transport in absence of a magnetic field

We are now in the position to apply the numerical procedure outlined in the previous section to systems with a random configuration of scalar impurities or adatoms and we begin by studying the case of a vanishing magnetic field.

[4] To simplify the notation, we will omit the brackets $\langle \cdot \rangle$ outside of this section as it should be clear from the context whether the averaged or individual conductance/conductivity is meant.

5.4.1 Scalar impurities

We first consider scalar impurities. The case of a diverging scattering length was already studied in Ref. [11] and the numerically obtained conductivity for a sample of length L and impurity density n was found to grow according to $\sigma = (4e^2/\pi h)(\ln nL^2 - \ln\ln nL^2)$, agreeing quantitatively with the RG-prediction for the corresponding Nonlinear σ-model in the symmetry class DIII with a Wess-Zumino term. This subsection aims to find out what happens when a finite value of ℓ_s breaks the chiral symmetry thereby driving the system into the class AII (with a topological θ term). To that end, we numerically calculate the average conductivity as a function of the system size (in units of the mean impurity distance $\ell_{\text{imp}} = \sqrt{WL/N\text{imp}} = \sqrt{1/n}$) for several values of the scattering length (using the method outlined in Sec. 5.3).

Fig. 5.1 shows the results of this computation, where for each data point, an average was taken over approximately 500 disorder configurations (in this section we will simply write σ instead of σ_{xx}). We observe that differences compared to the resonant case are merely quantitative and small. This can also be seen in Fig. 5.2 where the averaged conductivity at a fixed system size $L = 20\ell_{\text{imp}}$ as a function of the scattering length ℓ_s is shown (both for exclusively positive and random sign scattering lengths).

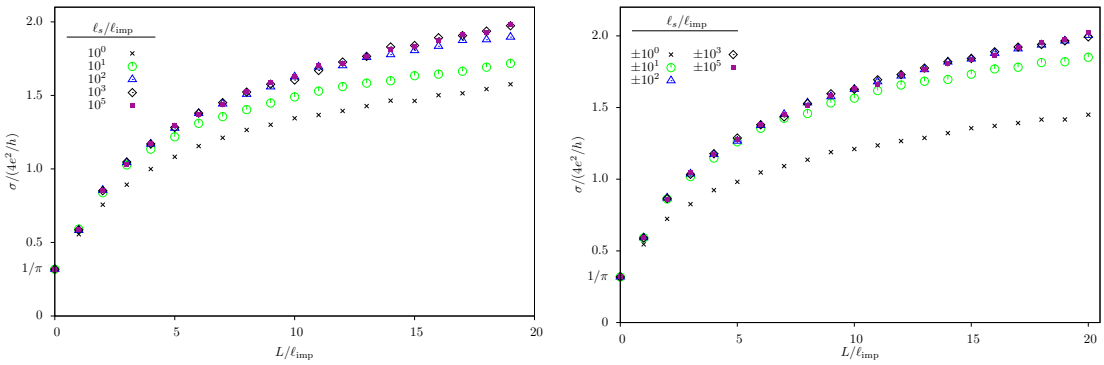

(a) positive sign scalar potentials

(b) random sign scalar potentials

Figure 5.1: The conductivity for non-resonant scalar impurities shows a behaviour very similar to the one observed in Ref. [11] for resonant scalar impurities. The conductivity for strictly positive values of the scattering length is slightly larger than it is for scattering lengths of the same magnitude but of random sign; this effect becomes less pronounced upon increasing the modulus of ℓ_s.

Another point to mention is that the conductivity for strictly positive values of the scattering length is slightly larger than it is for scattering lengths of the same magnitude

but of random sign. This is most likely because the equal-sign scalar potentials systematically shift the spectrum into one direction thereby increasing the density of states at the Dirac point (even if the DOS does not change much beyond that shift); this doping effect becomes less pronounced at larger values of L/ℓ_{imp} or ℓ_s/ℓ_{imp} where the presence of many/strong impurities already makes the density of states quite different from the clean scenario.

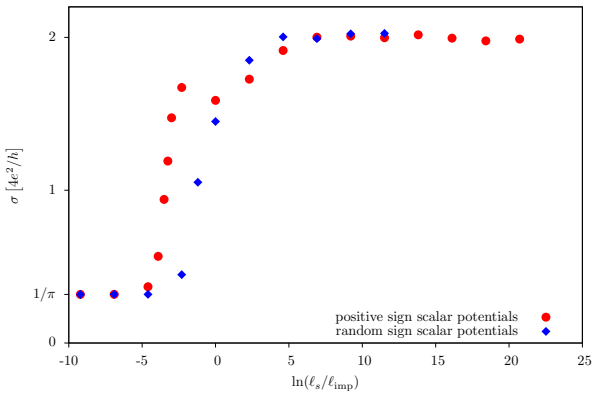

Figure 5.2: The conductivity at a fixed system size $L/\ell_{\text{imp}} = 20$ saturates at a scattering-length-independent value reasonably quickly when ℓ_s is increased towards the resonant limit.

5.4.2 Adatoms

Let us now investigate the case of adatoms. We will only consider the compensated scenario, where the number of adatoms on the A-sublattice equals the number of adatoms on the B-sublattice and also assume that the adatom's colour is random (the study of situations with unbalanced colour distributions is postponed to the following chapter). We numerically calculate the averaged conductivity as a function of the system size (in units of the mean impurity distance ℓ_{imp}) for several values of the scattering length using the method outlined in Sec. 5.3. The aspect ratio is again fixed at $W/L = 4$ and the average was taken over approximately 500 samples. Figure 5.3 shows the results of this computation both for strictly positive and random-sign scattering lengths.

To discuss these results, we would first like to note the quasi-ballistic regime at small values of the scattering length and the impurity density ℓ_{imp}^{-1}, where the presence of impurities enhances the conductivity when the adatoms have strictly positive scattering lengths while this phenomenon is absent in the case random-sign scattering lengths. As

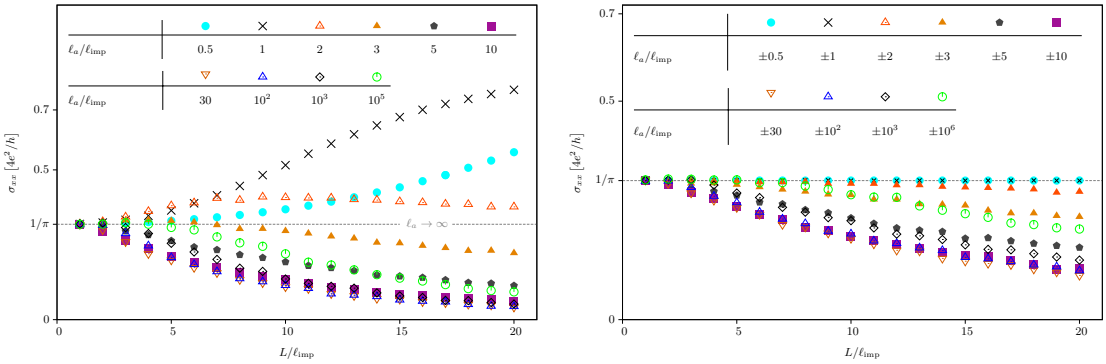

(a) positive sign on-site-potentials

(b) random sign on-site-potentials

Figure 5.3: Averaged conductivity for compensated, randomly coloured adatoms.

with the scalar impurities, this is likely to be caused by a systematic shift of the spectrum (thereby increasing the density of states at zero energy) when all the on-site potentials have the same sign whereas no such shift can be expected when the on-site potentials vanish on average.

Next we would like to comment on the change in localisation behaviour for curves of different scattering lengths. This is best done on the background of the NLσM predictions [8]. Anderson localisation is expected at long scales if a finite ℓ_a breaks the chiral symmetry (because the system then belongs to the conventional Wigner-Dyson class AI), while in the vacancy limit $\ell_a \to \infty$, the chiral symmetry is preserved, and the system belongs to the chiral BDI class where no localisation is expected (the conductivity is of the order $4e^2/\pi h$, [11]). This behaviour can indeed be observed in Fig. 5.3 and is further illustrated in Fig. 5.4, where the conductivity at a large, fixed value of L/ℓ_{imp} is shown as a function of the scattering length.

Fig. 5.4 indicates that at a fixed value of the impurity concentration, ℓ_{imp}^{-2}, the localisation length is a non-monotonic function function of the impurity strength: for small $\ell_a/\ell_{\mathrm{imp}}$, the mean free path is large and ballistic behaviour prevails up to large values of L/ℓ_{imp}; for very large values of $\ell_a/\ell_{\mathrm{imp}}$ the system behaves chiral up to certain scale due to the vicinity to a fixed point of the chiral BDI class, but eventually gets attracted to the localisation fixed point of the Wigner-Dyson class AI; at an intermediate value (the data suggests $\ell_a/\ell_{\mathrm{imp}} \approx 30$), the localisation length has a minimum.

It is important to note, however, that Fig. 5.4 predicts that extremely large scattering lengths are needed to avoid localisation – even the biggest value shown in Fig. 5.4,

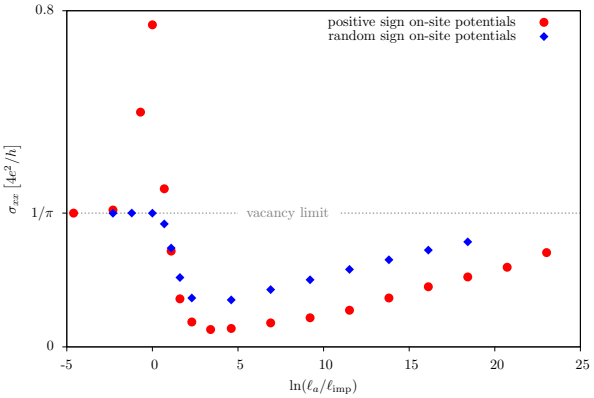

Figure 5.4: Averaged conductivity at a fixed value $L/\ell_{\rm imp} = 20$ as a function of the adatom scattering length ℓ_a (the average was taken over roughly 500 samples). The dotted grey line indicates the averaged conductivity expected for vacancies as obtained numerically in Ref. [11]. Prolonging the curves far enough to see this limit actually reached was not possible with the current version of the code, as the computation in mpfr precision (which is necessary at such large values of the scattering length) would require too much time.

$\ell_a/\ell_{\rm imp} = 10^{10}$, is not yet sufficient. This means that although above data further supports the prediction of the NLσM and the finding of Ref. [11] that there is no localisation due to vacancies at the Dirac point, it also suggests that this absence of localisation is close to impossible to observe in an experiment where the ideal situation of being exactly at zero energy can hardly be achieved. The sample doping is relevant here, as Fig. 5.A.2 shows that it is crucial to be exponentially close to the Dirac point in order to see the resonant aspect of vacancy physics: if the sample doping deviates from zero by just a meV, the scattering length of the vacancy is already reduced to the order of $10^3 a$ (which is not anywhere near $10^{10}\ell_{\rm imp}$ even more so as typically $\ell_{\rm imp} \gg a$).

Indeed, numerical studies of the conductivity in the presence of vacancies using recursive Green's function methods like in Ref. [12] (see in particular their Fig. 4) show a conductivity that eventually goes to zero upon increasing the vacancy density. Looking at their data more closely, one can see that in sweeping through different sample doping, the authors come very close to the Dirac point but never are exactly at zero doping. In the lower left inset of their Fig. 4 one can see that their smallest doping is of the order of μeV. This seems very small but the scattering length of a vacancy at this sample doping is of the order of only $10^5 a$ according to Eq. (5.14).

Figure 5.5 finally compares the results of the unfolded scattering theory (as shown in

the previous figures) with those obtained using the KWANT package [13] and yields reasonable agreement.

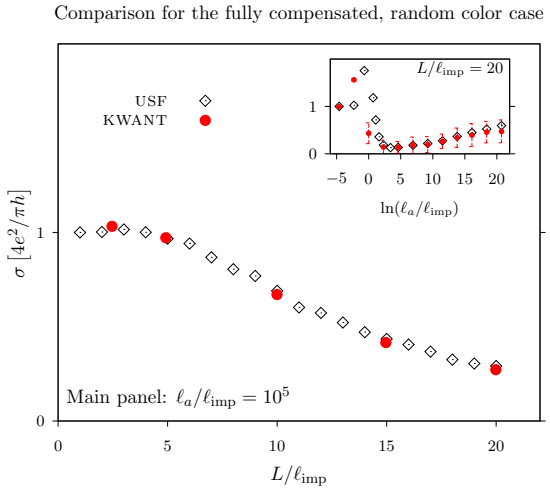

Figure 5.5: Comparison of the data obtained by the unfolded scattering formalism (short: USF; the data was already presented in Figures 5.3 and 5.4, see their captions for more details) with conductivities calculated by the KWANT code and averaged over 30 to 50 graphene ribbons of dimensions $W \approx 600a, L \approx 100a$ with armchair edges at the transversal boundaries.

5.5 The case of a quantising magnetic field

5.5.1 Scalar impurities

To study the effect of a strong magnetic field, we calculate the conductivity for the case of scalar-impurity-disorder as a function of L/ℓ_{imp} for various magnetic lengths $\ell_B = \sqrt{\hbar/eB}$. Fig. 5.6 shows the results of this computation, where for each data point, an average was taken over 1000-2000 disorder configurations.

The most salient features of Fig. 5.6 are the following:

1. The conductivity goes to zero when impurities all have a positive sign.

2. The conductivity strives to a value of approximately $0.4 \times 4e^2/\pi h$ when the sign of the scattering lengths is random.

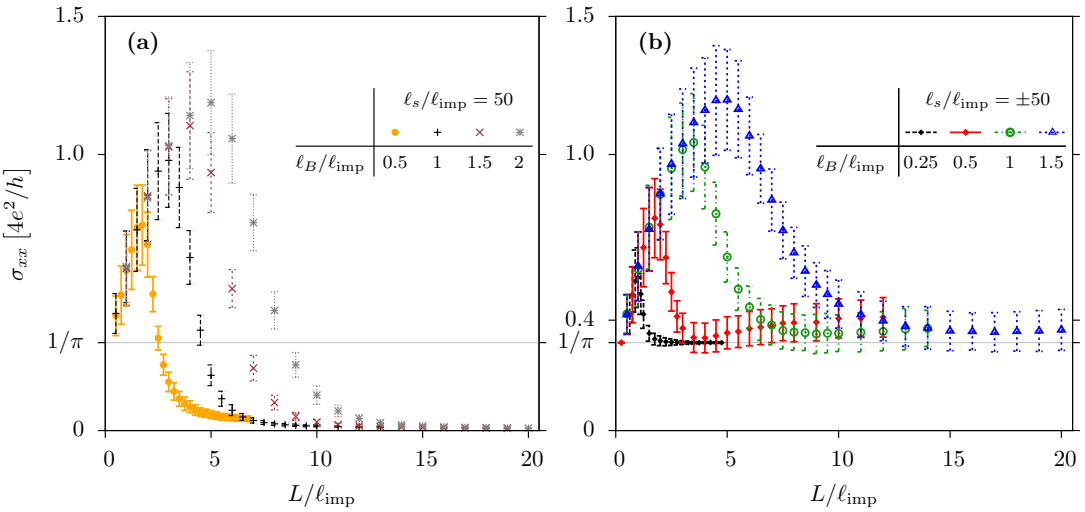

Figure 5.6: Under the influence of a strong magnetic field, the conductivity shows a rather diverse behaviour: depending on the parameter values, one can observe localisation (a), the approach to some critical conductivity $\approx 0.4 \times 4e^2/\pi h$ (curves in b apart from the black one), and a quasi-ballistic regime where $\sigma = 4e^2/\pi h$ for any disorder realisation (black curve in b). The plot shows the average conductivity in the presence of scalar-impurity-disorder with a fixed scattering length $|\ell_s| = 50$ (strictly positive sign in subplot a, random sign in subplot b) for various values of the magnetic length. The error bars represent sample-to-sample fluctuations (i.e. the standard deviations) of the conductivity.

3. For the largest magnetic field shown, the deviation from the ballistic conductivity is fully suppressed (black curve in subplot b).

Let us begin by discussing the first two phenomena which can be understood in terms of the quantum Hall behaviour expected for graphene systems where the disorder does not mix valleys [14]. In this case, the problem can be described, on large length scales, by two decoupled NLσMs in symmetry class A with a topological θ term. The renormalisation flow is the same as in the standard IQHE (which was first proposed in Refs. [15, 16]) as depicted in Fig. 5.7. When all the impurities have a positive sign, there is an effective shift of the spectrum and the Fermi energy of our system is removed from the Landau level centre leading to an expected renormalisation flow as indicated by the blue curve in Fig. 5.7. In the case of scalar impurities with a scattering length of random sign, there is no shift of the spectrum such that the Fermi energy of our system remains in the centre of the broadened level, where the delocalised, valley-degenerate critical state is to located and one expects a renormalisation flow along the critical line (see red arrow in Fig. 5.7).

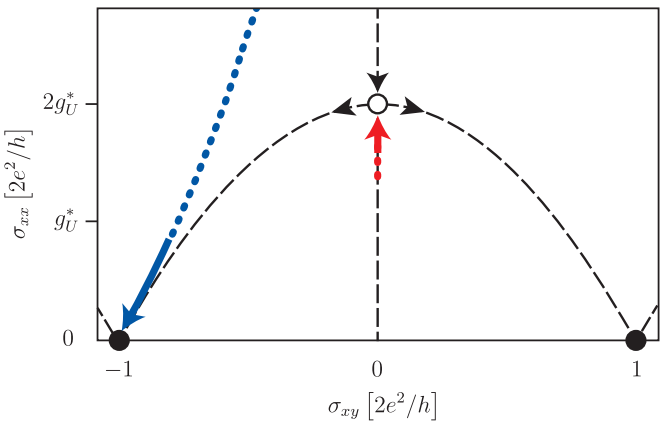

Figure 5.7: Schematic RG flow for scalar impurities. The red and blue lines illustrate possible flows leading to the conductivity curves observed in Fig. 5.6, where the red curve corresponds to the situation with random sign impurities, while the blue curve belongs to the equal-sign case.

To support this hypothesis, Fig. 5.8 verifies that the data shown in Fig. 5.6 is consistent with one-parameter scaling for $\ell_s/\ell_{\mathrm{imp}} = 50$ (subplot b) and two-parameter scaling for $\ell_s/\ell_{\mathrm{imp}} = \pm 50$ (subplot a) as suggested by the tentative flows in Fig. 5.7.

Let us now come to the third feature of Fig. 5.6 mentioned in the list above: for the strongest magnetic field shown, $\ell_B = 0.25\ell_{\mathrm{imp}}$ (see the black curve in subplot b), we

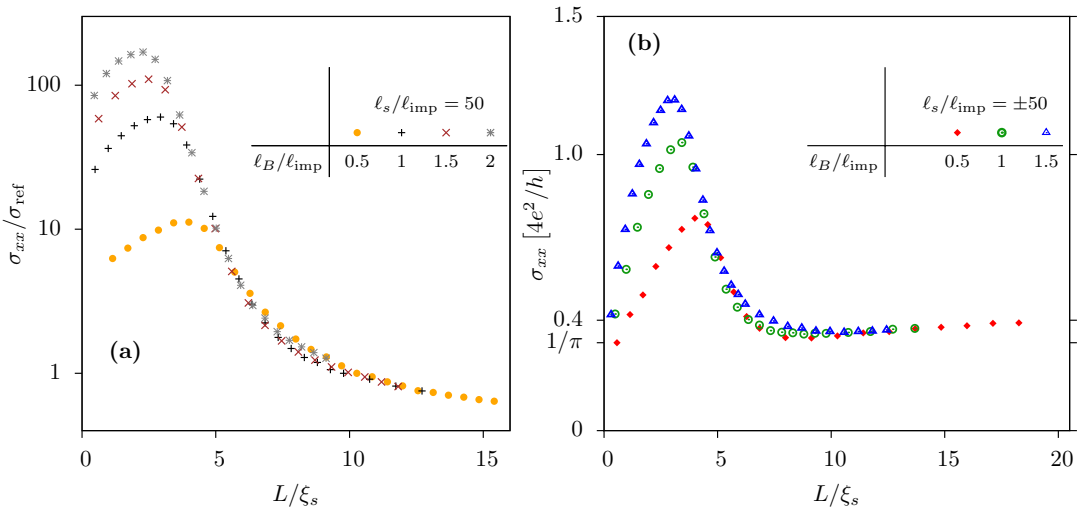

Figure 5.8: The plot shows the same data as Fig. 5.6 but as a function of the rescaled system length, L/ξ_s, where $\xi_s = 1.17\ell_B(1 + 0.126\ell_{\rm imp}/\ell_B)$ was obtained by making the curves in subplot b (the single-parameter-scaling case) overlap. When the scattering lengths are all positive, we expect that the conductivity depends on two parameters, $\sigma_{xx} = \sigma_{xx}(L/\xi_s, \theta)$. The data given in subplot (a) suggests that the two-parameter-scaling is of the special form $\sigma_{xx}(L/\xi_s, \theta) = f(\theta) \cdot g(L/\xi_s)$ as can be seen by plotting the ratio $\sigma_{xx}/\sigma_{\rm ref}$ with $\sigma_{\rm ref} = \sigma_{xx}(L/\xi_s = 10\xi_s, \theta)$ what eliminates the unknown function f and leads to an overlap of all the curves.

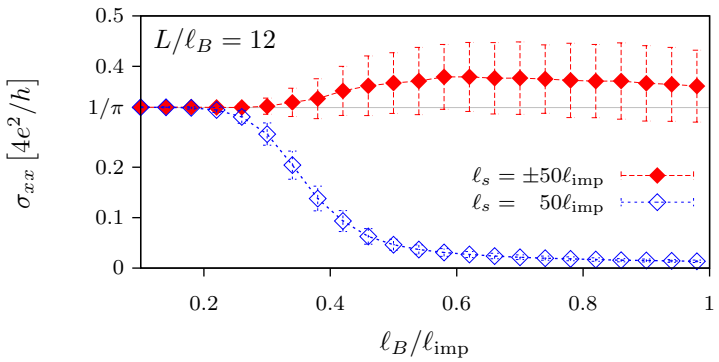

Figure 5.9: Depending on the strength of the magnetic field, the conductivity either stays at its ballistic value (with no sample-to-sample fluctuations) or shows quantum Hall behaviour (flowing either to the quantum Hall critical point or gets localised). The plot shows the average conductivity in presence of scalar impurities at a fixed system size $L = 12\ell_B$ as a function of the magnetic length (in units of the average impurity distance $\ell_{\rm imp}$).

observe a regime where the deviations of the conductivity from its ballistic value $4e^2/\pi h$ are fully suppressed (note that the sample-to-sample fluctuations vanish). As can be seen in Fig. 5.9, this regime also exists when the sign of the scattering length is strictly positive (here the effect is even more surprising as the conductivity at smaller magnetic fields would tend to zero) and in the following subsection we will see that it also exists for adatoms. While the details of this surprising phenomenon are not fully understood, it is likely that an explanation includes the following ingredients:

- the fact that magnetic fields are unable to change the Dirac point conductivity in *clean* graphene [17, in particular Sec. V.C],
- the observation that the Dirac point conductivity is typically carried by only a small number of modes (see Section 3.3),
- and the finding that s-wave scatterers are unable to fully lift the degeneracy of a Landau level when the flux per impurity is large compared to the flux quantum [18, 19] (Brezin et al. call this phenomenon 'level condensation' [18]).

5.5.2 Adatoms

Fig. 5.6 shows the situation for compensated, randomly coloured adatoms (the average was again taken over 1000-2000 disorder configurations).

Unlike the case of scalar impurities, this case shows localisation for both strictly positive and random sign values of the scattering length. This can be understood, again, from the theory proposed in Ref. [14]: as the presence of adatoms mixes valleys, the initially valley-degenerate critical state is now split into a state below and a state above the centre of the broadened Landau level. This means that the random-sign disorder leads to a flow towards a plateau fixed point so we therefore observe localisation (see the red curve in Fig. 5.11). While for scattering lengths that are all positive, one can hope to shift the energy critical state to zero energy, this does not seem to be case for parameter values chosen in Fig.5.10 and it is reasonable to assume that the data realises a flow similar to the blue curve in Fig. 5.11.

As was done for scalar impurities in the previous subsection, we can check whether the current data is consistent with the single- or two-parameter-scaling suggested by the conjectured RG flows. Fig. 5.12 shows that this is indeed the case.

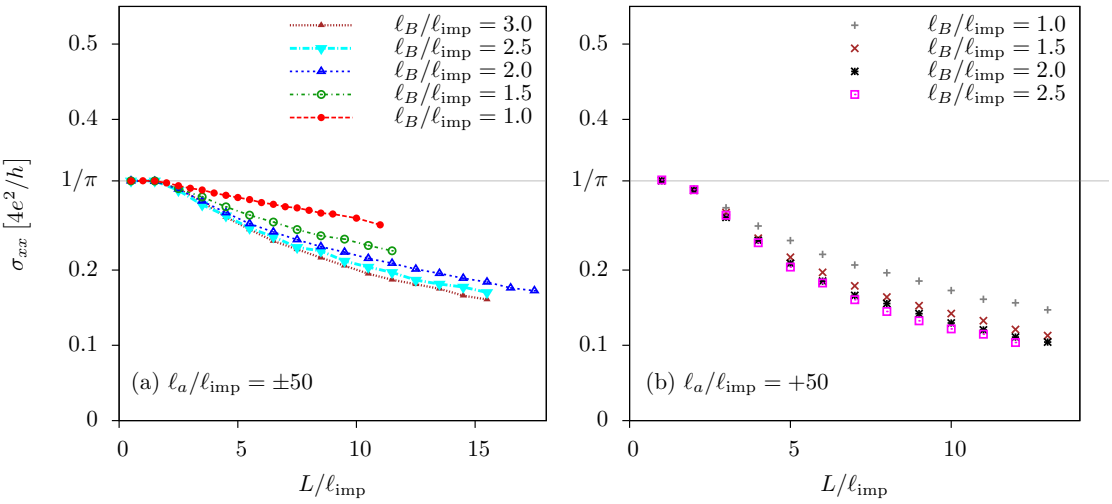

Figure 5.10: Average conductivity in presence of compensated, randomly coloured adatoms with a fixed scattering length $|\ell_a| = 50$ (random signs in subplot a, strictly positive signs in subplot b) for various values of the magnetic length.

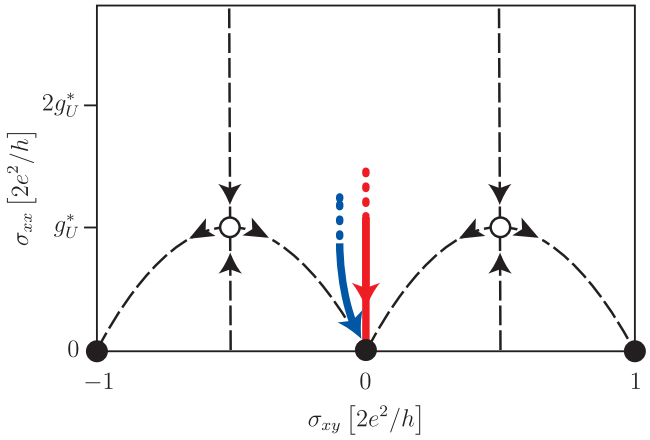

Figure 5.11: Schematic RG flow for adatoms. The red and blue lines illustrate possible flows leading to the conductivity curves observed in Fig. 5.10, where the red curve corresponds to the situation with random sign impurities, while the blue curve belongs to the equal-sign case.

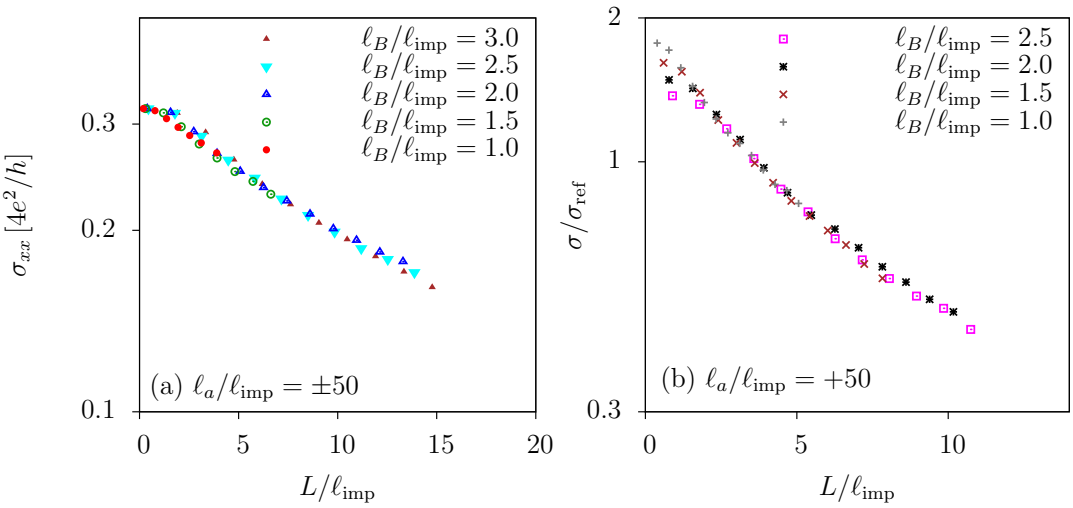

Figure 5.12: The plot shows the same data as Fig. 5.10 but as a function of the rescaled system length, L/ξ_a, where $\xi_a = 8.85\ell_{\rm imp} + 8.85\exp(-1.73\ell_B/\ell_{\rm imp})$ was obtained by making the curves in subplot a (where single-parameter-scaling is expected) overlap. When the scattering lengths are all positive, we expect that the conductivity depends on two parameters, $\sigma_{xx} = \sigma_{xx}(L/\xi_a, \theta)$. The data given in subplot (b) suggests that the two-parameter-scaling is of the special form $\sigma_{xx}(L/\xi_a, \theta) = f(\theta) \cdot g(L/\xi_a)$ as can be seen by plotting the ratio $\sigma_{xx}/\sigma_{\rm ref}$ with $\sigma_{\rm ref} = \sigma_{xx}(L/\xi_a = 3.6\xi_a, \theta)$ what eliminates the unknown function f and leads to an overlap of all the curves.

We want to finish this subsection by noting, that the level-condensation physics can also be observed for adatoms (see Fig. 5.13).

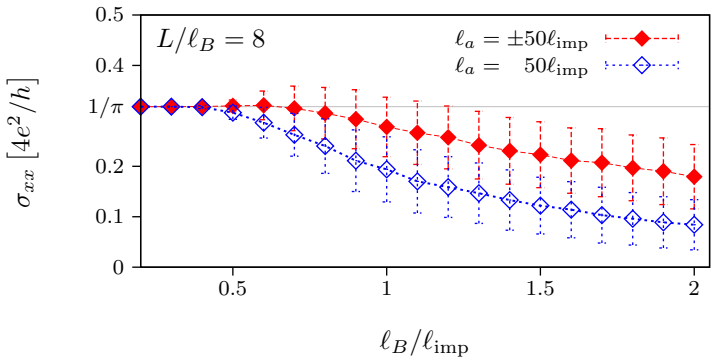

Figure 5.13: Depending on the strength of the magnetic field, the conductivity either stays at its ballistic value (with no sample-to-sample fluctuations) or shows quantum Hall behaviour (gets localised). The plot shows the average conductivity in presence of randomly coloured, compensated adatoms at a fixed system size $L = 8\ell_B$ as a function of the magnetic length (in units of the average impurity distance ℓ_{imp}).

Appendices to Chapter 5

5.A The T matrix for adatoms and vacancies

We will now calculate the integrated T matrix for adatoms and vacancies. We will show in the case of undoped graphene with an on-site potential of strength V_0 located in unit cell $\boldsymbol{R}_0$, that the integrated T matrix is given by the expression

$$T = \ell_a \begin{cases} \begin{pmatrix} 1 & 0 & 0 & e^{-i\theta_+^c} \\ 0 & 0 & 0 & 0 \\ 0 & 0 & 0 & 0 \\ e^{i\theta_+^c} & 0 & 0 & 1 \end{pmatrix}, & \text{if the adatoms is on an } A \text{ site,} \\ \begin{pmatrix} 0 & 0 & 0 & 0 \\ 0 & 1 & e^{-i\theta_-^c} & 0 \\ 0 & e^{i\theta_-^c} & 1 & 0 \\ 0 & 0 & 0 & 0 \end{pmatrix}, & \text{if the adatoms is on a } B \text{ site,} \end{cases} \tag{5.10}$$

where we have introduced the scattering length

$$\ell_a = A_{\mathrm{UC}} V_0 \tag{5.11}$$

and phases

$$\theta_\pm^c = \pm\alpha + 2\boldsymbol{K}\boldsymbol{R}_0. \tag{5.12}$$

Using the fact that $\exp[2i\boldsymbol{K}\boldsymbol{R}_0] = \exp[-i\boldsymbol{K}\boldsymbol{R}_0]$ can take only three possible values $\exp[2\pi ic/3]$ with $c = -1, 0, 1$, one can rewrite this phase as

$$\theta_\pm^c = \pm\alpha + 2\pi c/3, \qquad c = -1, 0, 1. \tag{5.13}$$

We follow the nomenclature of Ref. [20] and call the index c the colour of the on-site impurity.

We see that the (s-wave) scattering properties (on the level of the effective mass approximation) of an individual adatom in undoped graphene is fully characterised

1. by its position $\boldsymbol{r}$,
2. its sublattice index $\eta = \pm 1$,
3. its strength (parametrised by the scattering length ℓ_a),
4. and its colour $c \in \{-1, 0, 1\}$.

Before proceeding with the proof of Eq. (5.10), there are two important remarks to be made.

First, note that the colour degree of freedom equips the honeycomb lattice with the superstructure illustrated in Fig. 6.1. Chapter 7 studies the implications coloured adatoms on the transport properties.

Although we will only consider the case of undoped graphene in this chapter, as a second remark it is important to mention how the integrated T matrix looks at finite doping μ. This is relevant, for instance, when comparing the results of this chapter with numerical calculations in a tight binding model (where one often uses a small finite doping of the sample to increase the numerical stability; Ref. [20] is an example) or (even more importantly), when using the results of this chapter to interpret experimental data, as there always will be some uncertainty how close to undoped the measured sample actually was. As was shown in Ref. [21], the integrated T matrix keeps the form of Eq. (5.10) but the scattering length is changed to

$$\frac{\ell_a}{a} = \left[\left(\frac{\sqrt{3} V_0}{t} \right)^{-1} + \frac{2}{3\pi} \frac{\mu}{t} \left(\ln \left(\frac{3}{0.56 |\mu| / t} \right) - \gamma + i\pi/2 \right) \right]^{-1}, \tag{5.14}$$

where $\gamma = 0.577216\ldots$ is the Euler-Mascheroni constant. As is illustrated in Fig. 5.A.2, the scattering length remains proportional to the on-site potential as long as V_0 is not too large, but saturates at a finite μ-dependent value when V_0 is sufficiently big. This means in particular, that realising an ideal vacancy limit is only possible for very small doping.

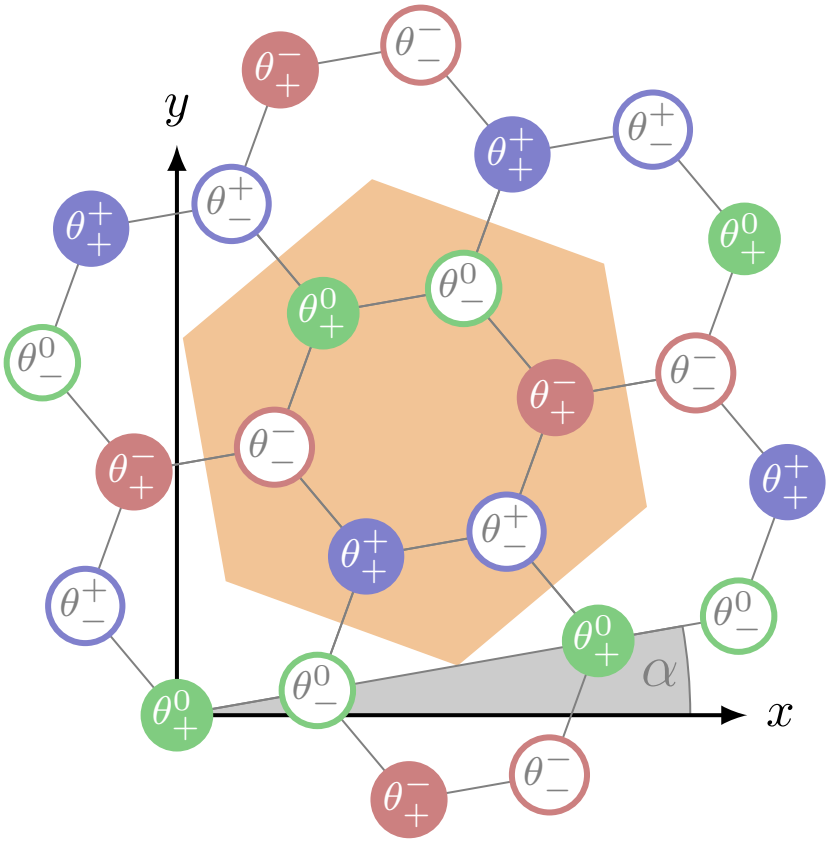

Figure 5.A.1: The phase $\theta_\pm^c = \pm\alpha + 2\pi c/3, c \in \{-, 0, +\}$ of the adatom T matrices endows the honeycomb lattice with a superstructure whose six-atomic unit cell is shown here in yellow and has an area three times as big as $A_{\mathrm{UC}} = \sqrt{27}a^2/2$, the area of the graphene unit cell. This Figure was adapted from [20].

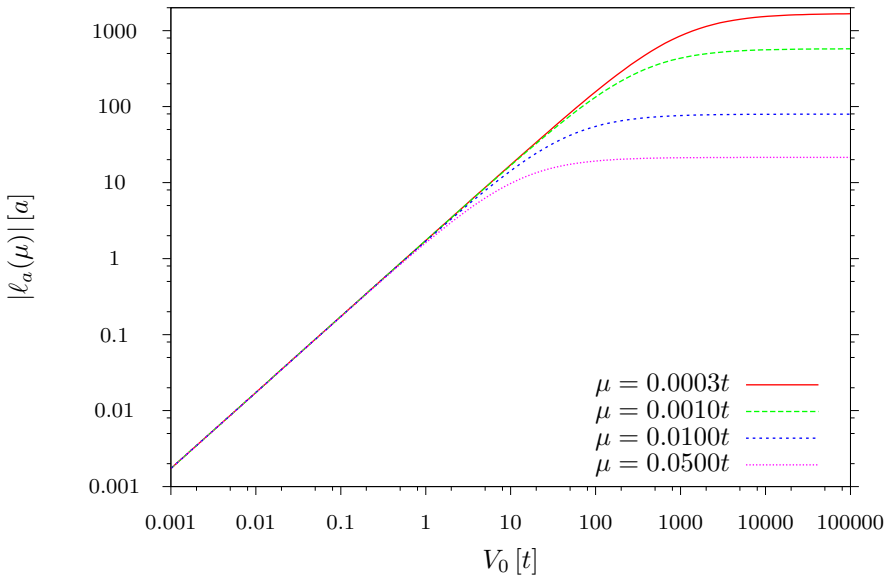

Figure 5.A.2: Dependence of scattering length on the on-site potential for various sample dopings.

Proof of Eq. (5.10) (Expression for the T matrix a zero doping)

The T matrix has the form

$$T(\boldsymbol{r},\boldsymbol{r}') = V(\boldsymbol{r})\delta(\boldsymbol{r}-\boldsymbol{r}') + V(\boldsymbol{r})g^R(\boldsymbol{r}-\boldsymbol{r}')V(\boldsymbol{r}') + \int \mathrm{d}^2 r''\; V(\boldsymbol{r})g^R(\boldsymbol{r}-\boldsymbol{r}'')V(\boldsymbol{r}'')g^R(\boldsymbol{r}''-\boldsymbol{r}')V(\boldsymbol{r}') + \ldots, \tag{5.15}$$

where $g^R(\boldsymbol{r}-\boldsymbol{r}')$ is the retarded Green's function of clean graphene as it was derived in the Appendix 3.A. We can anticipate a strong simplification of Eq. (5.15) when considering undoped graphene as the Green's function at zero energy is off-diagonal in sublattice space while V acts on only one sublattice: in this case the T matrix is basically identical to the potential itself, $T(\boldsymbol{r},\boldsymbol{r}') = \delta(\boldsymbol{r}-\boldsymbol{r}')V(\boldsymbol{r})$, since all but the first term of Eq. (5.15) vanish.

The main difficulty in deriving the T-matrix of an on-site potential at zero energy and zero doping is therefore to figure out how such short range potentials can be described within the effective-mass approximation in the first place (as this description was initially developed to study potentials which are smooth on the scale of the lattice constant [22]). This problem was already addressed in the context of carbon-nanotubes [23, 24]

but we will follow the approach taken in [21] which is to solve the scattering problem off a single isolated on-site potential in infinitely extended graphene (this can be done analytically) and then to compare the result with the solution of the Lippmann-Schwinger equation in the effective-mass-description (which will involve the integrated T matrix). This way of deriving the T matrix has the positive side-effect that we can briefly discuss the zero-energy solution that forms in a close vicinity and on the opposite sublattice of an infinitely strong on-site impurity (i.e. the vacancy-induced localised state studied, for instance, in Refs. [25, 26]).

Let us start by calculating the zero-energy scattering solution off an isolated on-site potential in the following tight-binding model of undoped graphene:

$$0 = V_0 \delta_{\boldsymbol{R}\boldsymbol{R}_0} \Psi_A(\boldsymbol{R}) - t\left[\Psi_B(\boldsymbol{R}) + \Psi_B(\boldsymbol{R}-\boldsymbol{a}_1) + \Psi_B(\boldsymbol{R}-\boldsymbol{a}_2)\right], \tag{5.16a}$$

$$0 = -t\left[\Psi_A(\boldsymbol{R}) + \Psi_A(\boldsymbol{R}+\boldsymbol{a}_1) + \Psi_A(\boldsymbol{R}+\boldsymbol{a}_2)\right]. \tag{5.16b}$$

Here we assumed that the impurity is located on the A site of the unit cell at position $\boldsymbol{R}_0$; further, $\boldsymbol{R} = n_1\boldsymbol{a}_1 + n_2\boldsymbol{a}_2, n_1, n_2 \in \mathbb{Z}$ denotes a vector of the direct lattice (see Figure 5.A.3) and $t \approx 2.7\,\mathrm{eV}$ is the nearest-neighbour hopping energy. We allow the lattice to be rotated by an angle α relative to the previously used convention where the x-axis was parallel to the armchair direction. The lattice is then spanned by the vectors $\boldsymbol{a}_1 = \sqrt{3}(\cos(\pi/6+\alpha), \sin(\pi/6+\alpha))^T$ and $\boldsymbol{a}_2 = \sqrt{3}(\cos(-\pi/6+\alpha), \sin(-\pi/6+\alpha))^T$, while the reciprocal lattice has basis vectors $\boldsymbol{b}_2 = (4\pi/3a)(\sin(\pi/6+\alpha), -\cos(\pi/6+\alpha))^T$. The Dirac points have coordinates $\boldsymbol{K} = (4\pi/3\sqrt{3}a)(\sin\alpha, -\cos\alpha)^T$ and we choose $\boldsymbol{K}' = -\boldsymbol{K}$.

The scattering solution $\Psi(\boldsymbol{R})$ due to an incoming wave $\Psi^{(0)}(\boldsymbol{R})$, which is a linear combination of the four zero energy solutions $\left\{(e^{\pm i\boldsymbol{K}\boldsymbol{R}}, 0)^T, (0, e^{\pm i\boldsymbol{K}\boldsymbol{R}})^T\right\}$, can be determined from the Lippmann-Schwinger equation

$$\begin{aligned}\Psi(\boldsymbol{R}) &= \Psi^{(0)}(\boldsymbol{R}) + \sum_{\boldsymbol{R}'} \mathrm{g}^R(\boldsymbol{R}-\boldsymbol{R}')V(\boldsymbol{R})\Psi(\boldsymbol{R}') \\ &= \Psi^{(0)}(\boldsymbol{R}) + \mathrm{g}^R(\boldsymbol{R}-\boldsymbol{R}_0)\begin{pmatrix} V_0 & 0 \\ 0 & 0 \end{pmatrix}\Psi(\boldsymbol{R}_0)\end{aligned} \tag{5.17}$$

where we used that

$$V(\boldsymbol{R}) = \delta_{\boldsymbol{R}\boldsymbol{R}_0}\begin{pmatrix} V_0 & 0 \\ 0 & 0 \end{pmatrix}, \tag{5.18}$$

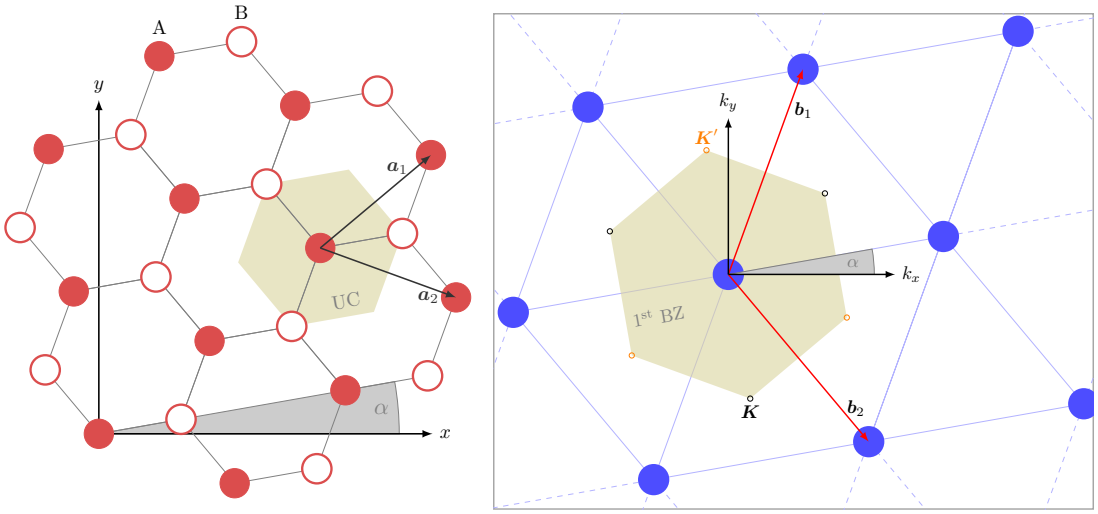

(a) coordinate space (b) reciprocal space

Figure 5.A.3: The choice of coordinate system used to describe the honeycomb lattice in this section. It is characterised by the angle α enclosed between the x-axis and the armchair direction. The Wigner-Seitz cells of the direct and the reciprocal lattice are shown in yellow and have areas $A_{\mathrm{UC}} = \sqrt{27}a^2/2$ and $A_{\mathrm{BZ}} = (2\pi)^2/A_{\mathrm{UC}}$, respectively.

and g^R denotes the retarded zero-energy/zero-doping Green's function of clean, infinitely extended graphene. In Appendix 3.A.1, above Green's function is derived in detail so we can restrict ourselves to summarise a few of its main properties here. First, we note that the retarded and advanced Green's functions coincide when $\varepsilon = \mu = 0$ (that is why the superscript R was omitted). Second, its diagonal elements in sublattice space vanish. And third, its off-diagonal elements are equal, real, and given by

$$\mathrm{g}_{BA}(\boldsymbol{R}-\boldsymbol{R}') = \begin{cases} \frac{A_{\mathrm{UC}}}{2\pi|\boldsymbol{R}-\boldsymbol{R}_0|}\left[e^{i\boldsymbol{K}(\boldsymbol{R}-\boldsymbol{R}_0)+i(\theta-\alpha)} + \mathrm{c.c.}\right], & \text{for } |\boldsymbol{R}-\boldsymbol{R}_0| \gg a, \\ \frac{a}{2}, & \text{for } |\boldsymbol{R}-\boldsymbol{R}_0| \lesssim a. \end{cases} \tag{5.19}$$

When the incoming wave is limited to the B sublattice, the scattering solution does not feel the impurity on the A sublattice and is therefore identical to $\Psi^{(0)}$. If the incoming wave is of the form $c_\pm(e^{\pm i\boldsymbol{K}\boldsymbol{R}}, 0)^T$ ($c_\pm$ being a constant), Eq. (5.17) can be easily solved and one finds

$$\Psi(\boldsymbol{R}) = \begin{pmatrix} c_\pm e^{\pm i\boldsymbol{K}\boldsymbol{R}} \\ \mathrm{g}_{BA}(\boldsymbol{R}-\boldsymbol{R}_0)c_\pm V_0 e^{\pm i\boldsymbol{K}\boldsymbol{R}_0} \end{pmatrix}. \tag{5.20}$$

In the vacancy limit we can simultaneously take $V_0 \to \infty, c_\pm \to \infty$ while keeping the

product $c_\pm V_0$ constant and thus obtain a localised vacancy state

$$\Psi_{\text{vac}}(\boldsymbol{R}) \propto \begin{pmatrix} 0 \\ g_{BA}(\boldsymbol{R}-\boldsymbol{R}_0)e^{\pm i\boldsymbol{K}\boldsymbol{R}_0} \end{pmatrix} \tag{5.21}$$

residing fully on the sublattice opposite to the one where the vacancy is located and decaying like $|\boldsymbol{R}-\boldsymbol{R}_0|^{-1}$ away from the impurity.

We are now in the position to determine the components of the integrated T matrix by comparison with the solution of the Lippmann-Schwinger equation in the effective-mass description,

$$\Phi(\boldsymbol{r}) = \Phi^{(0)}(\boldsymbol{r}) + \int \mathrm{d}^2 r' \int \mathrm{d}^2 r''\; g^R(\boldsymbol{r}-\boldsymbol{r}')T(\boldsymbol{r}',\boldsymbol{r}'')\Phi^{(0)}(\boldsymbol{r}''). \tag{5.22}$$

Here, $\Phi(\boldsymbol{r})$ is a four-component Dirac spinor in the valley-isotropic representation which can be related to the tight-binding wave function via

$$\begin{pmatrix} \Psi_A(\boldsymbol{R}) \\ \Psi_B(\boldsymbol{R}) \end{pmatrix} = \begin{pmatrix} u_A^\dagger(\boldsymbol{R})\Phi(\boldsymbol{R}) \\ u_B^\dagger(\boldsymbol{R})\Phi(\boldsymbol{R}) \end{pmatrix}, \tag{5.23a}$$

where for the given choice of coordinate system

$$u_A^\dagger(\boldsymbol{R}) = (e^{i\alpha/2 - i\pi/4 + i\boldsymbol{K}\boldsymbol{R}}, 0, 0, e^{-i\alpha/2 - i\pi/4 - i\boldsymbol{K}\boldsymbol{R}}), \tag{5.23b}$$

$$u_B^\dagger(\boldsymbol{R}) = (0, e^{-i\alpha/2 + i\pi/4 + i\boldsymbol{K}\boldsymbol{R}}, e^{i\alpha/2 + i\pi/4 - i\boldsymbol{K}\boldsymbol{R}}, 0). \tag{5.23c}$$

We will only consider the case of an incoming wave in the $\boldsymbol{K}$-valley which is residing on the A sublattice, i.e. $\Psi^{(0)}(\boldsymbol{R}) = (e^{i\boldsymbol{K}\boldsymbol{R}}, 0)^T$. We find that in this case, the scattering solution far away from the scattering centre, $|\boldsymbol{R}| \gg |\boldsymbol{R}_0|$, is given by (see Eq. (5.20))

$$\Psi(\boldsymbol{R}) \simeq \begin{pmatrix} e^{i\boldsymbol{K}\boldsymbol{R}} \\ \frac{A_{\text{UC}}V_0}{2\pi R}\left[e^{i\boldsymbol{K}(\boldsymbol{R}-\boldsymbol{R}_0)+i(\theta-\alpha)} + e^{-i\boldsymbol{K}(\boldsymbol{R}-\boldsymbol{R}_0)-i(\theta-\alpha)}\right] e^{i\boldsymbol{K}\boldsymbol{R}_0} \end{pmatrix} \tag{5.24}$$

In the effective-mass description, the incoming wave corresponds to the constant spinor $\Phi^{(0)} = (e^{-i\alpha/2+i\pi/4}, 0, 0, 0)^T$. Evaluating Eq. (5.22) in the asymptotic region with this incoming wave yields

$$\Phi_{A\boldsymbol{K}}(\boldsymbol{r}) \approx \begin{pmatrix} e^{-i\alpha/2+i\pi/4} \\ 0 \\ 0 \\ 0 \end{pmatrix} + \frac{1}{2\pi i r} \begin{pmatrix} 0 & e^{-i\theta} & 0 & 0 \\ e^{i\theta} & 0 & 0 & 0 \\ 0 & 0 & 0 & e^{-i\theta} \\ 0 & 0 & e^{i\theta} & 0 \end{pmatrix} \begin{pmatrix} T_{11} & T_{12} & T_{13} & T_{14} \\ T_{21} & T_{22} & T_{23} & T_{24} \\ T_{31} & T_{32} & T_{33} & T_{34} \\ T_{41} & T_{42} & T_{43} & T_{44} \end{pmatrix} \begin{pmatrix} e^{-i\alpha/2+i\pi/4} \\ 0 \\ 0 \\ 0 \end{pmatrix} \tag{5.25}$$

where we have used that g^R and $\Phi^{(0)}$ can be taken out of the integral for large $|\boldsymbol{r}|$ such that the spatial integration over $T(\boldsymbol{r}', \boldsymbol{r}'')$ produces the integrated T matrix we are looking for. The corresponding tight-binding wave function reads

$$\begin{pmatrix} u_A^\dagger(\boldsymbol{R})\Phi_{A\boldsymbol{K}}(\boldsymbol{R}) \\ u_B^\dagger(\boldsymbol{R})\Phi_{A\boldsymbol{K}}(\boldsymbol{R}) \end{pmatrix} = \begin{pmatrix} e^{i\boldsymbol{K}\boldsymbol{R}}\left(1+\frac{e^{-i\theta T_{21}}}{2\pi i R}\right) + e^{-i\boldsymbol{K}\boldsymbol{R}}\frac{e^{i(\theta-\alpha)}T_{31}}{2\pi i R} \\ e^{i\boldsymbol{K}\boldsymbol{R}}\frac{e^{i(\theta-\alpha)}T_{11}}{2\pi R} + e^{-i\boldsymbol{K}\boldsymbol{R}}\frac{e^{-i\theta}T_{41}}{2\pi R} \end{pmatrix}. \tag{5.26}$$

Comparing this with Eq. (5.24) shows that

$$T_{11} = A_{\mathrm{UC}}V_0, \qquad T_{21} = T_{31} = 0, \qquad T_{41} = A_{\mathrm{UC}}V_0 e^{i\alpha + 2i\boldsymbol{K}\boldsymbol{R}_0}. \tag{5.27}$$

The remaining components of the integrated T matrix can easily be obtained by repeating above calculation for the three other possible incoming waves and the completely analogous case of an adatom on a B site. Doing so, one finds

$$T = \ell_a \begin{cases} \begin{pmatrix} 1 & 0 & 0 & e^{-i\theta_+^c} \\ 0 & 0 & 0 & 0 \\ 0 & 0 & 0 & 0 \\ e^{i\theta_+^c} & 0 & 0 & 1 \end{pmatrix}, & \text{if the adatoms is on an } A \text{ site,} \\ \begin{pmatrix} 0 & 0 & 0 & 0 \\ 0 & 1 & e^{-i\theta_-^c} & 0 \\ 0 & e^{i\theta_-^c} & 1 & 0 \\ 0 & 0 & 0 & 0 \end{pmatrix}, & \text{if the adatoms is on a } B \text{ site,} \end{cases} \tag{5.28}$$

where

$$\ell_a = A_{\mathrm{UC}}V_0 \tag{5.29}$$

and

$$\theta_\pm^c = \pm\alpha + 2\pi c/3, \qquad c = -1, 0, 1. \tag{5.30}$$

The last definition uses the fact that $\exp[2i\boldsymbol{K}\boldsymbol{R}_0] = \exp[-i\boldsymbol{K}\boldsymbol{R}_0]$ can take only three possible values $\exp[2\pi i c/3]$ with $c = -1, 0, 1$ and this concludes the proof of Eq. (5.10). □

References of Chapter 5

[1] Gattenlöhner, S. *et al.* Quantum Hall Criticality and Localization in Graphene with Short-Range Impurities at the Dirac Point. *Physical Review Letters* **112**, 026802 (2014).

[2] Zirnbauer, M. R. Riemannian symmetric superspaces and their origin in random matrix theory. *J. Math. Phys.* **37**, 4986 (1996).

[3] Altland, A. & Zirnbauer, M. R. Nonstandard symmetry classes in mesoscopic normal-superconducting hybrid structures. *Physical Review B* **55**, 1142–1161 (1997).

[4] Zirnbauer, M. R. Symmetry Classes. *arXiv.org* (2010). 1001.0722v1.

[5] Schnyder, A. P., Ryu, S., Furusaki, A. & Ludwig, A. W. Classification of topological insulators and superconductors in three spatial dimensions. *Physical Review B* **78**, 195125 (2008).

[6] Evers, F. & Mirlin, A. D. Anderson transitions. *Reviews of Modern Physics* **80**, 1355–1417 (2008).

[7] Heinzner, P., Huckleberry, A. & Zirnbauer, M. R. Symmetry classes of disordered fermions. *Communications in Mathematical Physics* **257**, 725–771 (2005).

[8] Mirlin, A. D., Evers, F., Gornyi, I. V. & Ostrovsky, P. Anderson transitions: Criticality, symmetries and topologies. *International Journal Of Modern Physics B* **24**, 1577–1620 (2010).

[9] Titov, M., Ostrovsky, P., Gornyi, I. V., Schuessler, A. & Mirlin, A. D. Charge Transport in Graphene with Resonant Scatterers. *Physical Review Letters* **104** (2010).

[10] Press, W. H. (ed.) *Numerical Recipes 3rd Edition.* The Art of Scientific Computing (Cambridge University Press, Cambridge, 2007).

[11] Ostrovsky, P., Titov, M., Bera, S., Gornyi, I. V. & Mirlin, A. D. Diffusion and Criticality in Undoped Graphene with Resonant Scatterers. *Physical Review Letters* **105**, 266803 (2010).

[12] Cresti, A., Ortmann, F., Louvet, T., Van Tuan, D. & Roche, S. Broken Symme-

tries, Zero-Energy Modes, and Quantum Transport in Disordered Graphene: From Supermetallic to Insulating Regimes. *Physical Review Letters* **110**, 196601 (2013).

[13] Groth, C. W., Wimmer, M., Akhmerov, A. R. & Waintal, X. Kwant: a software package for quantum transport. *New Journal of Physics* **16**, 063065 (2014).

[14] Ostrovsky, P., Gornyi, I. V. & Mirlin, A. D. Theory of anomalous quantum Hall effects in graphene. *Physical Review B* **77**, 195430 (2008).

[15] Khmel'nitskii, D. E. Quantization of Hall conductivity. *JETP lett* (1983).

[16] Pruisken, A. M. M. On localization in the theory of the quantized hall effect: A two-dimensional realization of the θ-vacuum. *Nuclear Physics B* **235**, 277–298 (1984).

[17] Schuessler, A., Ostrovsky, P., Gornyi, I. V. & Mirlin, A. D. Analytic theory of ballistic transport in disordered graphene. *Physical Review B* **79**, 075405 (2009).

[18] Brezin, E., Gross, D. & Itzykson, C. Density of states in the presence of a strong magnetic field and random impurities. *Nuclear Physics B* **235**, 24–44 (1984).

[19] Gredeskul, S., Zusman, M., Avishai, Y. & Azbel, M. Electron in two-dimensional system with point scatterers and magnetic field. *IMA VOLUMES IN MATHEMATICS AND ITS APPLICATIONS* **96**, 95–142 (1998).

[20] Schelter, J., Ostrovsky, P., Gornyi, I. V., Trauzettel, B. & Titov, M. Color-dependent conductance of graphene with adatoms. *Physical Review Letters* **106**, 166806 (2011).

[21] Basko, D. M. Resonant low-energy electron scattering on short-range impurities in graphene. *Physical Review B* **78**, 115432 (2008).

[22] DiVincenzo, D. P. & Mele, E. J. Self-consistent effective-mass theory for intralayer screening in graphite intercalation compounds. *Physical Review B* **29**, 1685 (1984).

[23] Ando, T., Nakanishi, T. & Igami, M. Effective-Mass Theory of Carbon Nanotubes with Vacancy. *Journal of the Physical Society of Japan* **68**, 3994–4008 (1999).

[24] McCann, E. & Fal'ko, V. I. Symmetry properties of impurities in metallic single-wall carbon nanotubes. *International Journal Of Modern Physics B* **18**, 3195–3212 (2004).

[25] Pereira, V., Guinea, F., Lopes dos Santos, J., Peres, N. & Castro Neto, A. Disorder Induced Localized States in Graphene. *Physical Review Letters* **96**, 036801 (2006).

[26] Pereira, V., Lopes dos Santos, J. & Castro Neto, A. Modeling disorder in graphene. *Physical Review B* **77**, 115109 (2008).

6 Transport in the presence of coloured adatoms and vacancies

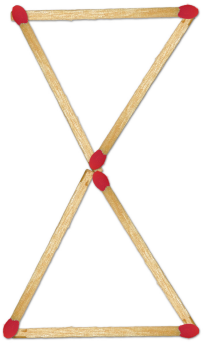

Move three matches to turn the two Dirac cones into four equilateral triangles.

An old puzzle

Let us imagine a large, rectangular graphene sample at charge-neutrality and attach strongly doped graphene leads to it; as was discussed in Sect. 3.2, such a setup behaves pseudo-diffusively with a conductivity of $\sigma = 4e^2/\pi h$, independent of the system length.[1] Imagine further that we perturb this clean sample by randomly choosing carbon sites (equally distributed between the two sublattices) and equipping these with finite on-site potentials by depositing suitable adatoms; such a situation was studied in the previous chapter and, as Fig. 5.3 indicates, leads to a vanishing conductivity: $\sigma \to 0$ for $L \to \infty$.[2] Let us use this scenario as the starting point to formulate the following question: Is it possible to turn this insulator into a quasi-ballistic conductor by slightly moving some of the adatoms? By 'quasi-ballistic conductor' we want to mean that its conductivity increases with the sample length (keeping the other parameters, such as the impurity

[1] To reduce the effect of the boundary conditions in transversal direction, let us assume for simplicity that $W \gg L$, where W is the width and L the length of the sample.

[2] We choose the number of adatoms such that $L \gg \ell_{\text{imp}} \gg a$, where ℓ_{imp} is the average distance between impurity sites and a the lattice constant of the honeycomb lattice.

density, fixed) and 'slightly moving' shall be concretised by the following constraint: the adatoms may at most be moved to an adjacent unit cell and must stay on the same sublattice.

As was discussed in the previous chapter, the scattering due to adatoms (or vacancies understood as a special case of adatoms) can be studied within the effective mass approximation and that on this level, each adatom is characterised by the following data:

1. its position $\boldsymbol{r}_n$,
2. its strength, parametrised by the scattering length $(\hat{\ell}_a)_n$ (which is infinite for vacancies at zero sample doping),
3. its sublattice, represented by the variable ζ_n, which is $+1$ for adatoms on the A-sublattice and -1 for adatoms on the B-sublattice, and finally
4. its colour $c_n \in \{-1, 0, +1\}$ which is related to the Bloch phase of the unit cell that the adatom occupies (see Fig. 6.1).

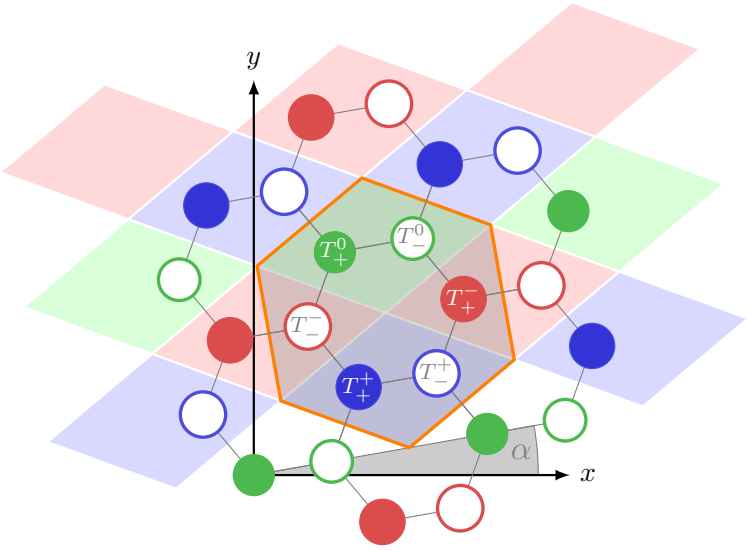

Figure 6.1: The T-matrix of an adatom, having colour c and being located on sublattice ζ, is proportional to the matrix T^c_ζ (the proportionality constant being the scattering length ℓ_a). The six distinct matrices $T^c_\zeta = \ell_a(1+\zeta\sigma_z\tau_z+\sigma_{-\zeta}\tau_- \exp[i\theta^c_\zeta]+\sigma_\zeta\tau_+ \exp[-i\theta^c_\zeta]$ (using the definitions $\sigma_\pm = (\sigma_x \pm i\sigma_y)/\sqrt{2}$, $\tau_\pm = (\tau_x \pm i\tau_y)/\sqrt{2}$, and $\theta^c_\pm = \pm\alpha + 4\pi c/3$) endow the honeycomb lattice with a superstructure whose six-atomic unit cell (see the orange hexagon) is three times as big as the graphene unit cell. See the appendix 5.A for more details.

Only the first and the last of these parameters may be changed in our thought experiment. Changing the $\boldsymbol{r}_n$ only slightly, however, cannot substantially alter the conductivity, as these parameters only enter the calculation as the arguments of the regularised Green's function which hardly changes on the length scale of the lattice constant. Consequently, any solution to our problem will need to make use the colour degree of freedom – if there is a solution at all.

While we have 'ignored' the colour degree of freedom so far (having only considered systems with adatoms of random colour), it is the aim of this chapter to explore the colours' impact on transport at the Dirac point. In particular, we will study the conductivity in the presence of many randomly placed adatoms which are *all* of the same colour. To that end, we will both use the unfolded scattering formalism (USF) on the effective-mass level (as outlined in Sec. 5.3) as well as the software package KWANT (see Ref. [1]) on the tight-binding level to calculate the conductivity for a single impurity configuration and average over many such configurations. It turns out that the conductivity of undoped graphene with single-colour adatoms of intermediate strength is not vanishing but increases with the sample length (keeping the other parameters, such as the impurity density, fixed), see Figures 6.8, 6.9 and 6.10. Consequently, the insulator in our thought experiment can indeed be turned conducting and the solution consists in picking one colour, leaving all adatoms of that colour where they are, while moving the other adatoms to one of the adjacent unit cells of the chosen colour.

There is only a small number of works that have looked into colour-related effects in electronic transport in graphene so far. That the colour degree of freedom is relevant for transport at all, has been demonstrated by Schelter et al. [2] for the case of vacancies, where the conductivity of the simplest non-trivial system[3] consisting of a short-and-wide graphene sample with two vacancies already showed a significant dependence on their colour.

Colour remains to be important in disordered systems. Ostrovsky et al. [4] found, using the unfolded scattering formalism, that when the numbers of vacancies on the two sublattices, N_A and N_B, are both equal and become sufficiently large, the conductivity saturates at a constant value that depends on whether the vacancy sites are all of the same colour or not: when the colours are random, the configuration-averaged conductivity remains roughly at its ballistic value of $4e^2/\pi h$ while for the single colour case, saturation happens approximately at $1.6 \times 4e^2/\pi h$ (see the top of Fig. 6.2; it was assumed that

[3] A system with only one vacancy would be trivial as a single vacancy does not change the Dirac point conductivity [3, 2].

the sample was oriented such that the x-axis was parallel to the zig-zag direction of the honeycomb lattice, i.e. $\alpha = \pi/2$; we will see that for $\alpha = 0$, the saturations value increases to roughly $2.2 \times 4e^2/\pi h$). The physical reason behind the formation of these plateaus is still unclear.

Hitherto unpublished recursive Green's function calculations for single-colour vacancies by Jörg Schelter [5] at small but finite sample doping (see the bottom of Fig. 6.2) do not show these plateaus. The reason for this is most likely that vacancies behave rather like finite-strength adatoms away from the Dirac point, as was discussed in Subsection 5.4.2. This suggests that a lot can be learned from studying the conductivity in presence of single-colour adatoms of finite strength (not only for their own sake but also to understand the vacancy case better).

Following the nomenclature of Ref. [4], we introduce the sublattice imbalance $\delta = (N_A - N_B)/N_{\text{imp}}$ (N_A and N_B being the number of adatoms on the respective sublattice), which is zero in the 'compensated' case, where $N_A = N_B$ and which equals 1 (or -1) in the fully sublattice-ordered case. We will only consider the extremal cases $\delta = 1$ and $\delta = 0$. This chapter is organised as follows: We begin by looking at the fully sublattice-ordered situation ($\delta = 1$) in Sec. 6.1 and will then study the more interesting compensated case ($\delta = 0$) in Sec. 6.2.

The *work in progress* presented in this chapter is being conducted in collaboration with Igor Gorny, Alexander Mirlin, Pavel Ostrovsky, Jörg Schelter, Björn Trauzettel, and Misha Titov.

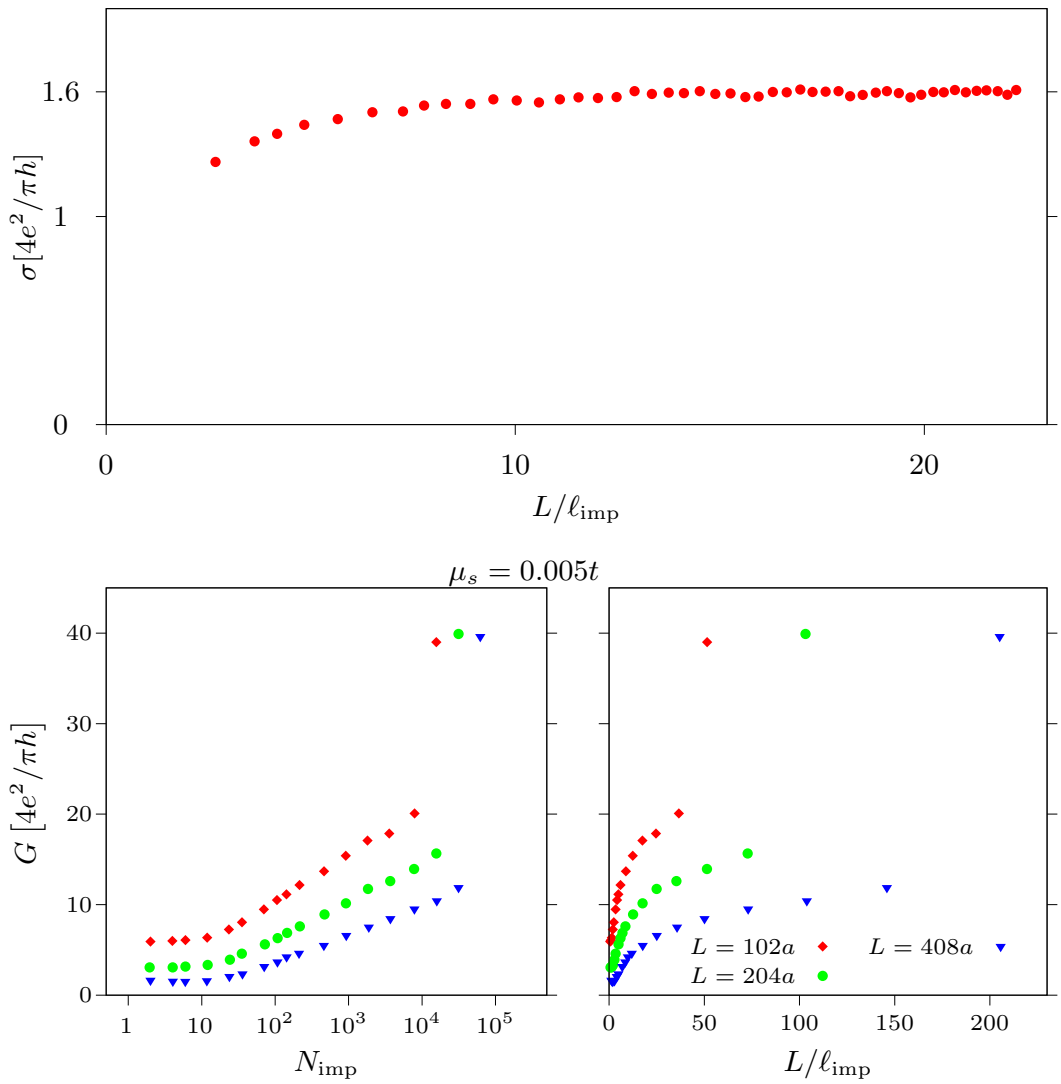

Figure 6.2: Top: Average conductivity for single-colour vacancies at the Dirac point calculated using the unfolded scattering formalism in [4] ($\alpha = \pi/2$.) Bottom: Conductance as a function of the impurity number (left) as well as a function of $L/\ell_{\mathrm{imp}} = \sqrt{nL^2}$ (right; n being the vacancy density). The calculation has been performed by Jörg Schelter using the recursive Green's function method (see [5]). The samples had a width of $W \approx 600a$ and (semi-conducting) armchair edges in transversal direction (corresponding to $\alpha = 0$); the leads where doped to $\mu_L = 0.15t$). For each data set, the point with the largest value of L/ℓ_{imp} corresponds to the scenario where all carbon atoms of the chosen colour are removed and the sample became 'striped'.

6.1 Fully sublattice-ordered, single-coloured adatoms

As was discussed by several groups [6, 7], adatoms have a tendency to attach themselves to sites of the same sublattice. It is therefore interesting to study situations where the sublattice imbalance $\delta = (N_A - N_B)/(N_{\mathrm{imp}})$ is non-zero. For simplicity, we consider only the case where the adatoms are *all* located on the same sublattice ($\delta = 1$). Sublattice-ordered adatoms introduce a spectral gap around zero energy [7]. When the adatoms are of infinite strength (i.e. in the vacancy limit), a very sharp peak remains exactly at zero energy [8]; this peak allows for a finite Dirac point conductivity of the order of the ballistic value $4e^2/\pi h$ [4, see the black curve in their Fig. 2(a) for the single-colour case; the conductivity seems not to vanish either in the fully sublattice-ordered, random-colour case, as one can check numerically with the USF]. In the numerical studies of reference [9], this non-zero conductivity is not observed (which is probably because the sample doping was never set exactly to zero in their calculations; see the discussion in Section 5.4.2).

For adatoms of finite strength, one expects no peak in the density of states at zero energy and the Dirac point conductivity should be zero in this case. As is shown in Figures 6.3 and 6.4, this is basically true also for the single-colour case, but only in the limit $W/L \to \infty$. This can be explained as follows. Consider the solutions of the Dirac equation in *clean* graphene at charge-neutrality when attached to highly doped leads [10] (compare with the results given in Section 3.3 in the limit of a vanishing magnetic field) and perform a rotation in valley space introducing the constant $\beta = -\exp\left[i(\alpha - 4\pi c/3)\right]$:

$$|\Phi_q^{(1)}\rangle = \begin{cases} e^{i(kx+qy)} \begin{pmatrix} 1 \\ 1 \\ \beta \\ \beta \end{pmatrix} - e^{i(-kx+qy)} \tanh qL \begin{pmatrix} 1 \\ -1 \\ \beta \\ -\beta \end{pmatrix}, & \text{if } x < 0, \\ \frac{e^{q(x-L)+iqy}}{\cosh qL} \begin{pmatrix} 1 \\ 0 \\ \beta \\ 0 \end{pmatrix} + \frac{e^{-q(x-L)+iqy}}{\cosh qL} \begin{pmatrix} 0 \\ 1 \\ 0 \\ \beta \end{pmatrix}, & \text{if } 0 < x < L, \\ \frac{e^{i(k(x-L)+qy)}}{\cosh qL} \begin{pmatrix} 1 \\ 1 \\ \beta \\ \beta \end{pmatrix}, & \text{if } x > L, \end{cases} \tag{6.1a}$$

$$|\Phi_q^{(2)}\rangle = \begin{cases} e^{i(kx+qy)} \begin{pmatrix} 1 \\ 1 \\ -\beta \\ -\beta \end{pmatrix} - e^{i(-kx+qy)} \tanh qL \begin{pmatrix} 1 \\ -1 \\ -\beta \\ \beta \end{pmatrix}, & \text{if } x < 0, \\ \frac{e^{q(x-L)+iqy}}{\cosh qL} \begin{pmatrix} 1 \\ 0 \\ -\beta \\ 0 \end{pmatrix} + \frac{e^{-q(x-L)+iqy}}{\cosh qL} \begin{pmatrix} 0 \\ 1 \\ 0 \\ -\beta \end{pmatrix}, & \text{if } 0 < x < L, \\ \frac{e^{i(k(x-L)+qy)}}{\cosh qL} \begin{pmatrix} 1 \\ 1 \\ -\beta \\ -\beta \end{pmatrix}, & \text{if } x > L. \end{cases} \tag{6.1b}$$

One can see that for $q = 0$, the wave function

$$\Psi(\boldsymbol{R}) = \left(e^{i\alpha/2 - i\pi/4 + i\boldsymbol{K}\boldsymbol{R}} \quad 0 \quad 0 \quad e^{-i\alpha/2 - i\pi/4 - i\boldsymbol{K}\boldsymbol{R}}\right) |\Phi^{(1)}_{q=0}\rangle \tag{6.2}$$

vanishes on all sites $\boldsymbol{R}$ on sublattice A and of colour c and this wave function is therefore not disturbed by any adatoms on these sites. This unperturbed wave function contributes a conductance quantum e^2/h per spin to the conductance. Fig. 6.5 shows the situation where the signs of the adatoms are random.

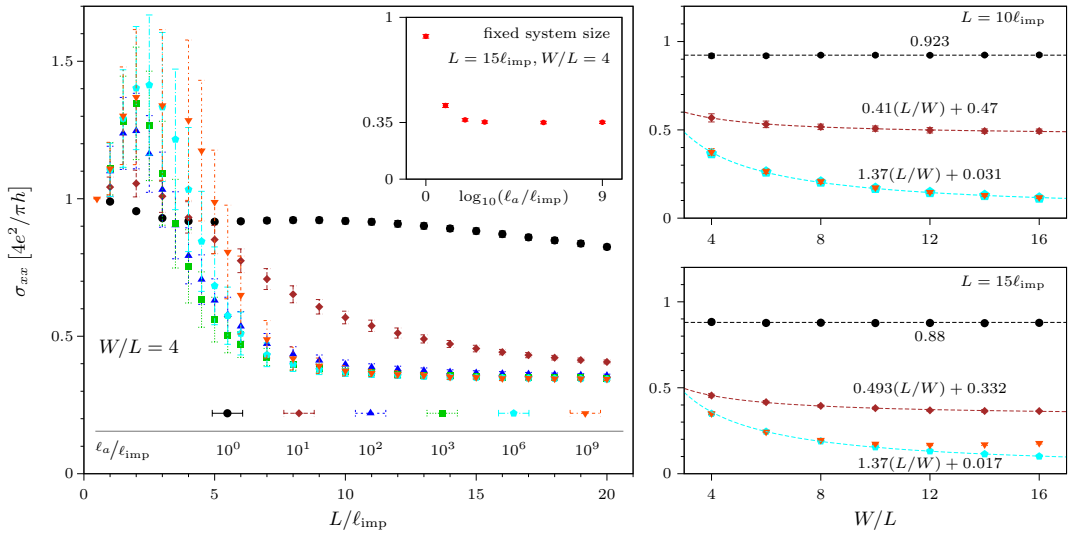

Figure 6.3: Conductivity for single colour, single sublattice adatoms of various scattering lengths (calculated by means of the unfolded scattering formalism as described in Section 5.3; error bars show sample-to-sample fluctuations). For large but finite scattering lengths, the conductivity vanishes in the limit $W/L \to \infty$ (for the smaller values of ℓ_a there is probably no full suppression of the conductivity), while the conductance remains non-zero due to the unperturbed state at zero transversal momentum.

It is also instructive to look at the conductivity in the presence of single-colour, single-sublattice vacancies at non-zero sample doping as was done by Jörg Schelter [5] using the recursive Green's function method. In Figure 6.1, we try to interpret this data by comparing the conductivity at very large impurity densities with the expected conductivity for clean supergraphene, which is the name we want to give to the lattice that arises when removing all carbon atoms of one colour and sublattice from the graphene sample.

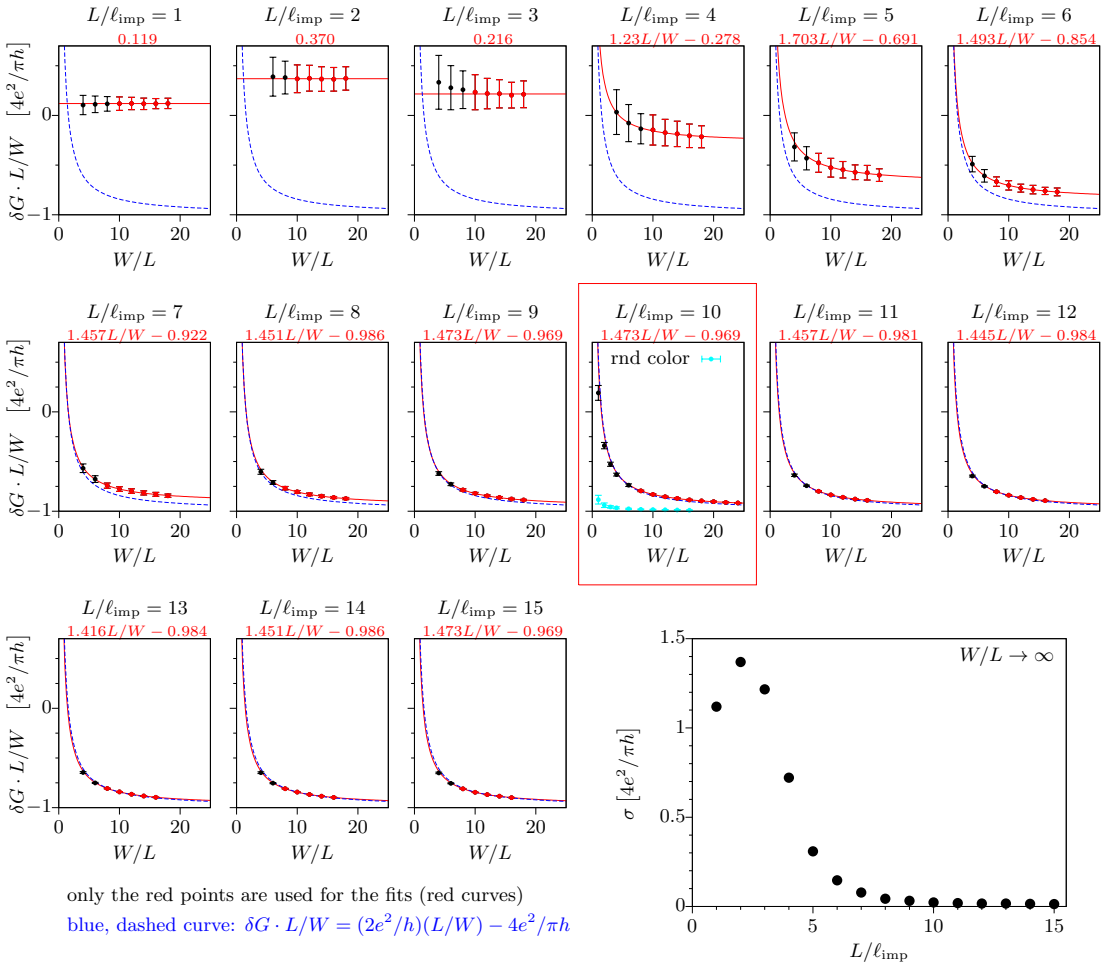

Figure 6.4: Conductivity (larger plot) and change of conductance relative to the ballistic value (smaller plots) for single colour, single sublattice adatoms of large but finite scattering length $\ell_a = 10^6 \ell_{\rm imp}$. For large $L/\ell_{\rm imp}$ the conductivity is close to zero (due to the formation of a gap at zero energy) and only the unperturbed mode contributes to the conductance (compare with the dashed blue lines which correspond to $G = G_{\text{unperturbed mode}}$). As the small plot for $L/\ell_{\rm imp} = 10$ confirms, the unperturbed mode is absent for random colour, single sublattice adatoms. The data was obtained by means of the unfolded scattering formalism (USF) as described in Section 5.3 and error bars show sample-to-sample fluctuations.

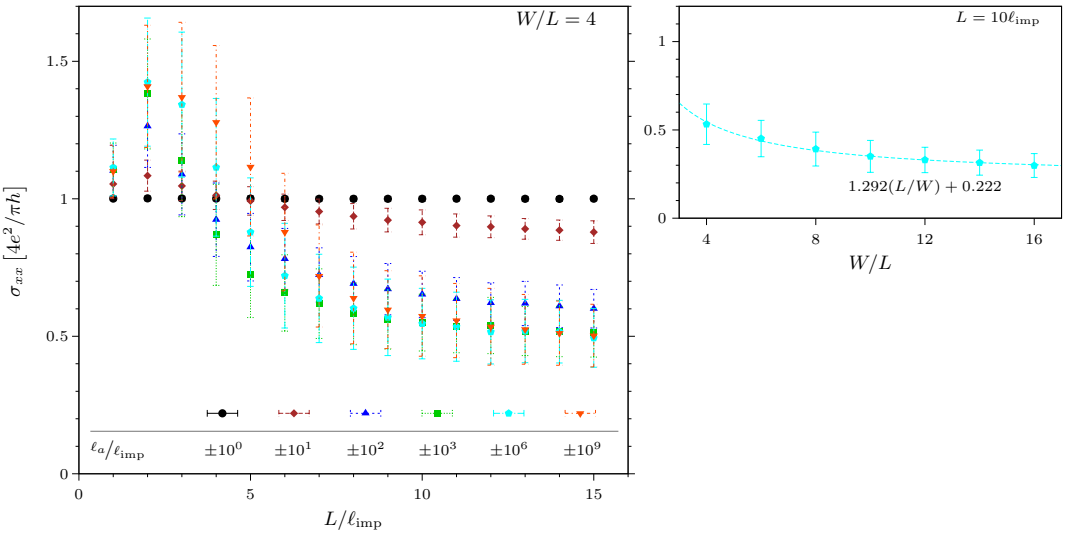

Figure 6.5: Conductivity for single colour, single sublattice adatoms (the potentials have random sign) of various scattering lengths (USF results; error bars show sample-to-sample fluctuations).

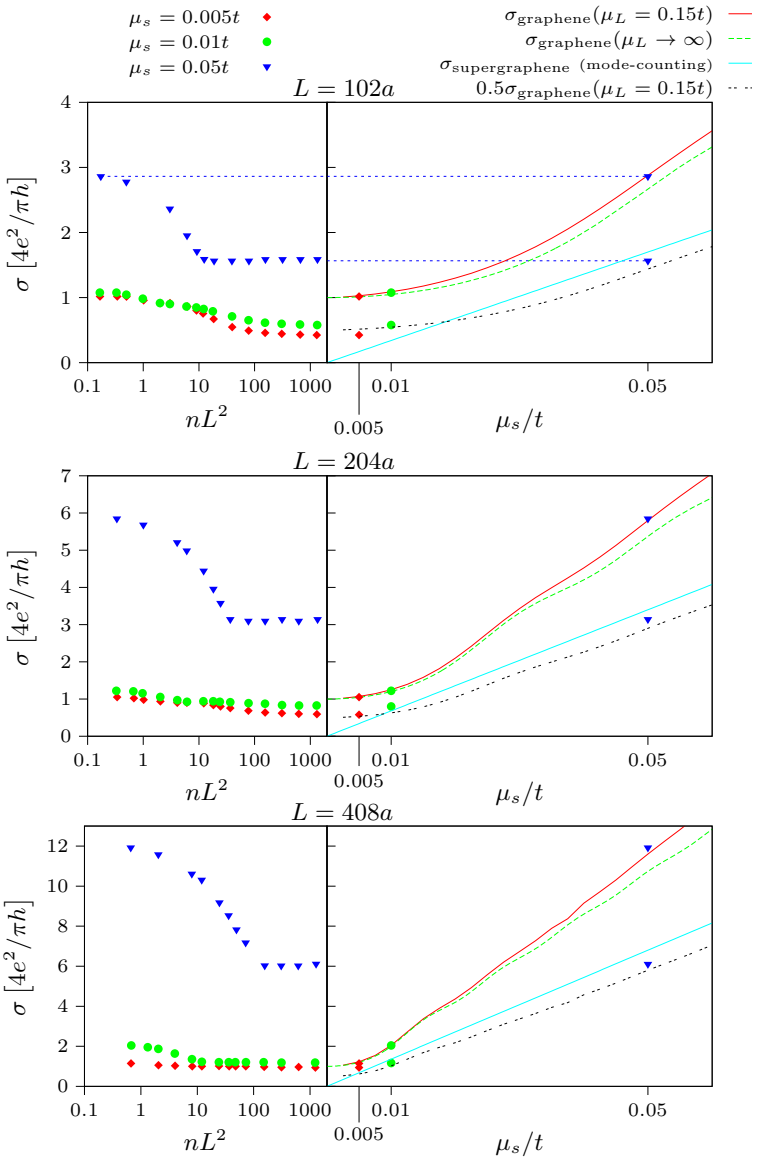

Figure 6.6: Comparison of Jörg Schelters's RGF results [5, The data was extracted from his Figure 5.6] for single colour, single sublattice vacancies (left panels) with the ballistic conductivities of graphene and supergraphene (right panels) which seem to be the limiting cases. The RGF results for small nL^2 values coincide nicely with the predictions for ballistic graphene whereas the results for large nL^2 approximately match the predictions for ballistic supergraphene (as is explained in the Sec. 6.A, the conductivity for supergraphene should be roughly half the graphene conductivity as there is just one distinct Dirac cone for supergraphene). The parameters in the RGF calculation were: doping in the leads $\mu_L = 0.15t$, sample width $W = 348\sqrt{3}a \approx 600a$.

6.2 Compensated, single-colour adatoms

In this section, preliminary results for the compensated, single-colour case are presented. Interestingly, the conductivity increases as a function of L/ℓ_{imp} for intermediate values of the scattering length ℓ_a (Figures 6.7 and 6.8) where localisation was strongest in the random-colour situation. This increase is also observed for adatoms of random sign (Figure 6.9), what rules out the possibility that a systematic shift of the density of states (as it happens in the case of on-site potentials of the same sign) is the main cause for the increasing conductivity. It is important to note that the unfolded scattering theory only describes the regime where the typical impurity distance ℓ_{imp} is much larger than the graphene lattice constant a; it is therefore unlikely that above increase is related to the formation of stripes in real space (stripes will play a role for very large adatom numbers when practically all sites of the chosen colour are occupied by adatoms; see Figures 6.10 and 6.11).

Figure 6.10 compares the results of the unfolded scattering formalism with those from a tight-binding calculation using Kwant. As long as $\ell_{\mathrm{imp}} \gg a$, the results agree. For smaller values of ℓ_{imp}, the conductivity starts to behave differently due to the formation of stripes in real space.

Figure 6.12 demonstrates that there is no significant dependence of the conductivity on the aspect ratio in the compensated case. Figure 6.13 shows as a consequence of Equation (5.14) in that the vacancy limit can only be observed directly at the Dirac point.

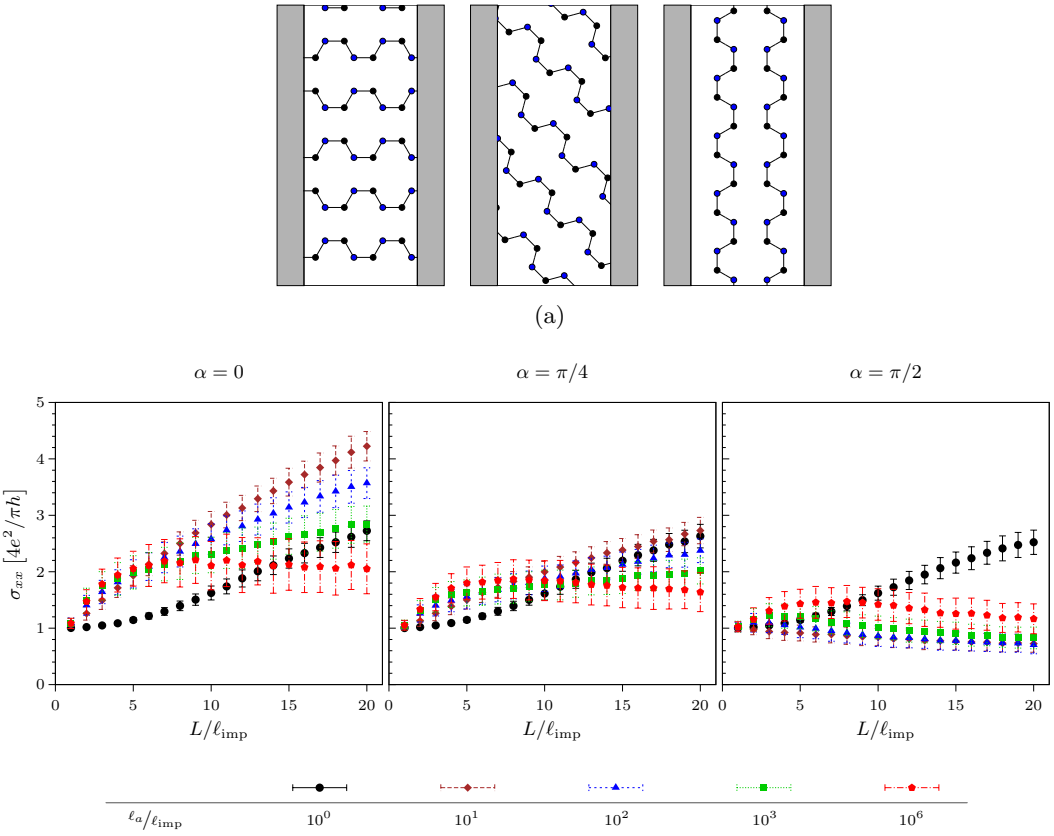

Figure 6.7: When adatoms are randomly put on lattice sites of one colour, the set of sites without adatoms is made up by all the sites of the other two colours (let us call these the backbone of the unperturbed sites) and the remaining sites of the chosen colour without adatoms. The subfigure **(a)** shows the backbone for orientations $\alpha = 0, \pi/4, \pi/2$. **(b)** Dirac point conductivity of graphene with single colour adatoms (equally distributed between the two sublattices) for different lattice orientations α and scattering lengths ℓ_a. The aspect ratio is $W/L = 4$ in all three plots and the data was obtained using the unfolded scattering formalism as described in Section 5.3; error bars show sample-to-sample fluctuations.

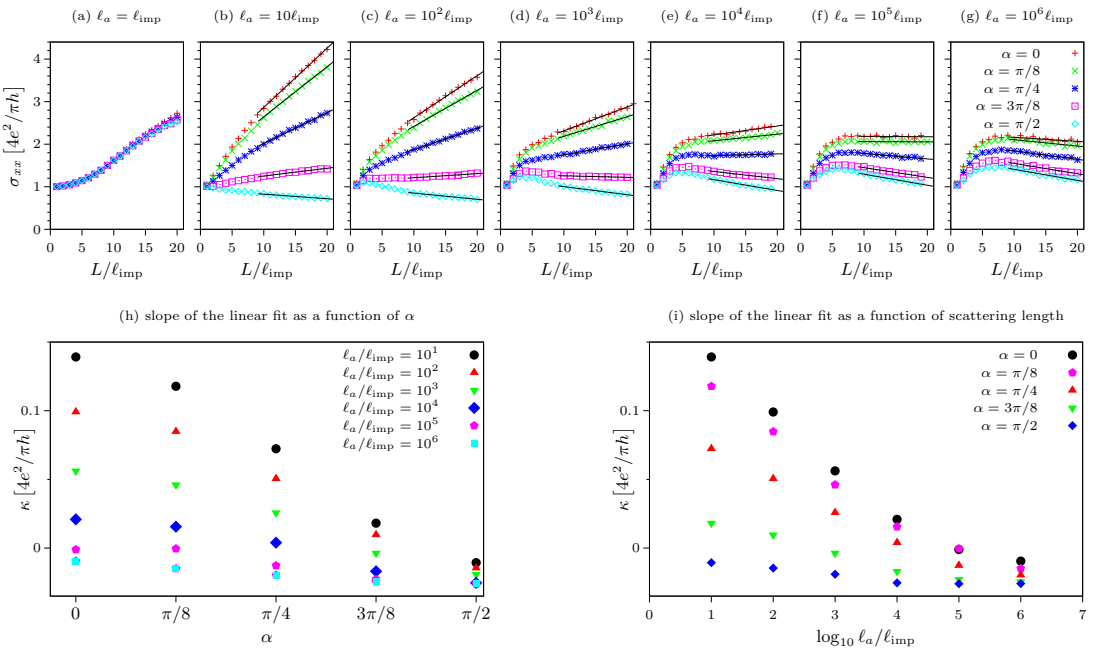

Figure 6.8: Dirac point conductivity of graphene with strictly positive adatom potentials (single color) and further parameters $W/L = 4, N_A = N_B, N_{\mathrm{samples}} = 500$ (USF results). The linear fits in Figs. (a)-(g) are of the form $\kappa L/\ell_{\mathrm{imp}} + \lambda$, its slopes are shown in Figs. (h)-(i).

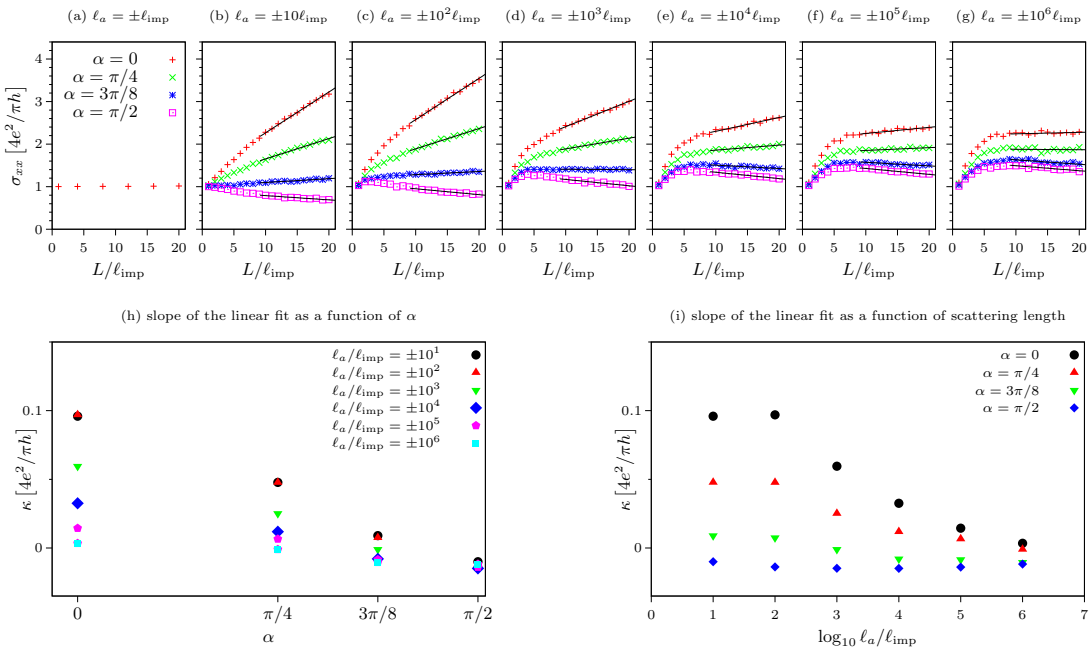

Figure 6.9: Dirac point conductivity of graphene with random sign adatom potentials (single color) and further parameters $W/L = 4, N_A = N_B, N_{\mathrm{samples}} = 200$ (USF results). The random signs destroy the effective doping effect but do not stop the α-dependent rise of σ. The linear fits in Figs. (a)-(g) are of the form $\kappa L/\ell_{\mathrm{imp}} + \lambda$, its slopes are shown in Figs. (h)-(i).

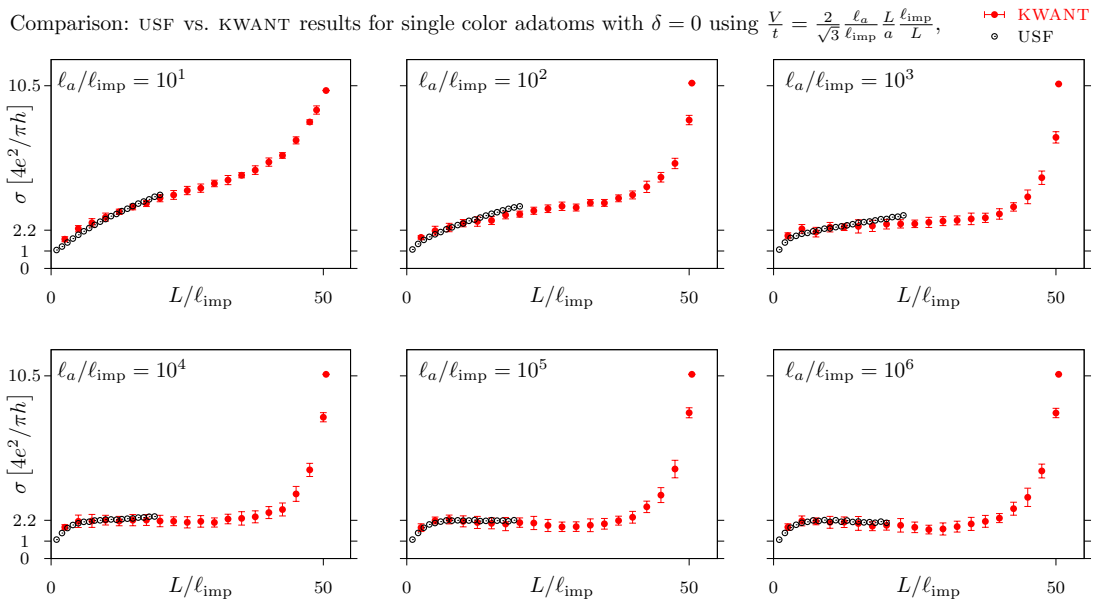

Figure 6.10: Comparison of the USF conductivities at the Dirac point with those calculated by the KWANT package. The Kwant results were obtained by averaging over 20 samples with metallic armchair edges ($\alpha = 0$) of dimensions $L \approx 100a$ and $W \approx 600a$ being attached to clean graphene leads doped to $\mu_L = 0.3t$ (error bars show sample-to-sample fluctuations); the adatoms were realised by on-site potentials of strength $(V/t) = (2/\sqrt{3})(\ell_a/\ell_{\rm imp})(L/a)(\ell_{\rm imp}/L)$. Note that the last point of each Kwant curve corresponds to the case where all sites of one colour are turned into impurities ('striped' graphene).

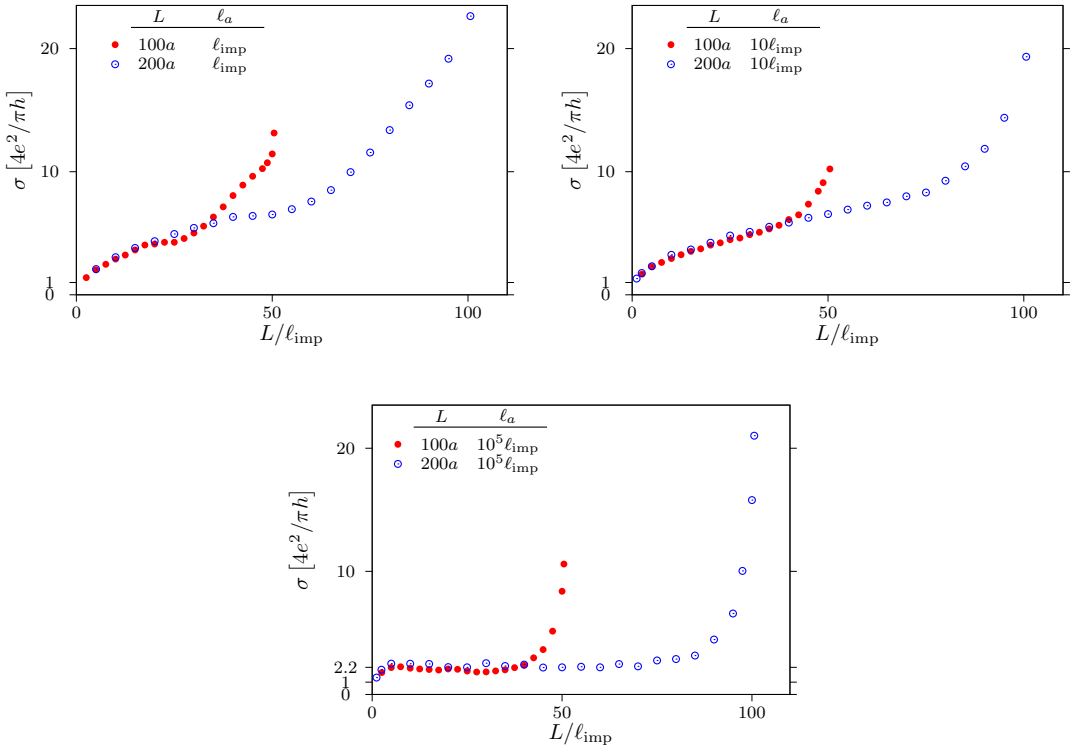

Figure 6.11: By choosing larger system sizes one can defer the transition to ballistic striped graphene and the conductivity behaves as expected from the continuum calculation for a wider range of L/ℓ_{imp} values. In particular, the plateau for very strong onsite potentials as seen in Ref. [4] is reproduced; the saturation value is larger in the plot at hand because in the paper $\alpha = \pi/2$ was chosen where the conductivity saturates at $1.6 \cdot 4e^2/\pi h$. Note that the last point of each curve corresponds to the case where all sites of one colour are turned into impurities ('striped' graphene). In above plots, $W \approx 600a$ was kept constant and the data was obtained using the KWANT package.

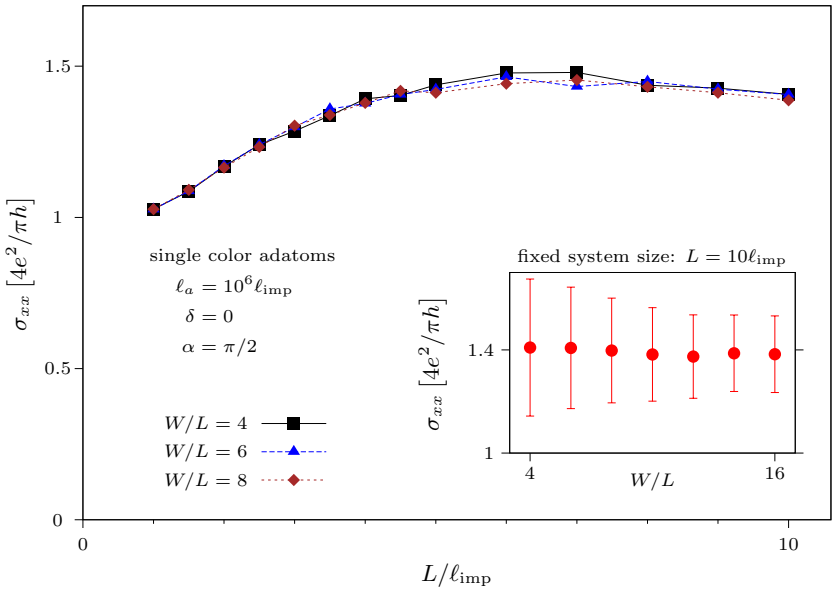

Figure 6.12: There seems to be no significant W/L-dependence of the conductivity in the presence of compensated, single-colour adatoms; the sample-to-sample fluctuations show some W/L-dependence, at least for small aspect ratios.

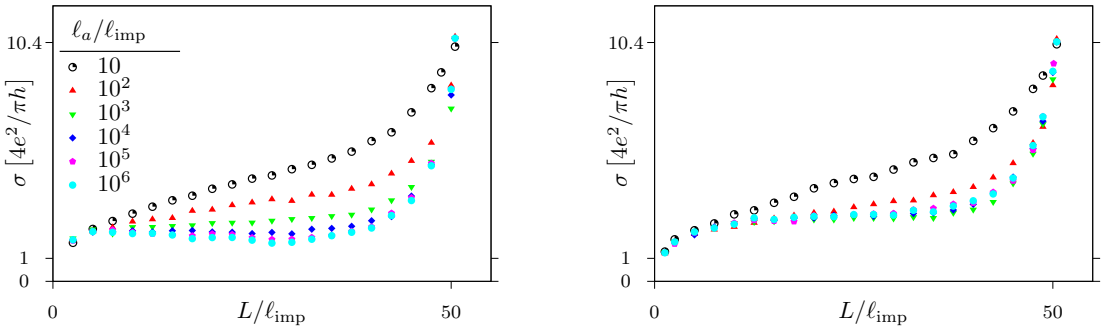

Figure 6.13: Conductivity in presence of single colour adatoms as a function of $L/\ell_{\rm imp}$ for zero sample doping (subplot a) and finite sample doping ($V_{\rm S} = -0.001t$, subplot b). To observe the resonant behaviour of impurities with large onsite potentials, it is essential to do the tight-binding calculation at zero sample doping, as for finite energies and strong impurities, we end up in the unitary limit where the T matrix is almost exclusively determined by the sample doping (see Eq. 5.14 or Fig. 5.A.2). Indeed, at non-zero energies (see subplot b), increasing the value of $\ell_a/\ell_{\rm imp}$ above some critical value around 10^3 does not significantly change the conductivity anymore. The samples used to obtain this data had the same parameters as in Fig. 6.10 and were also obtained using the KWANT package.

Appendices to Chapter 6

6.A Band structure of supergraphene

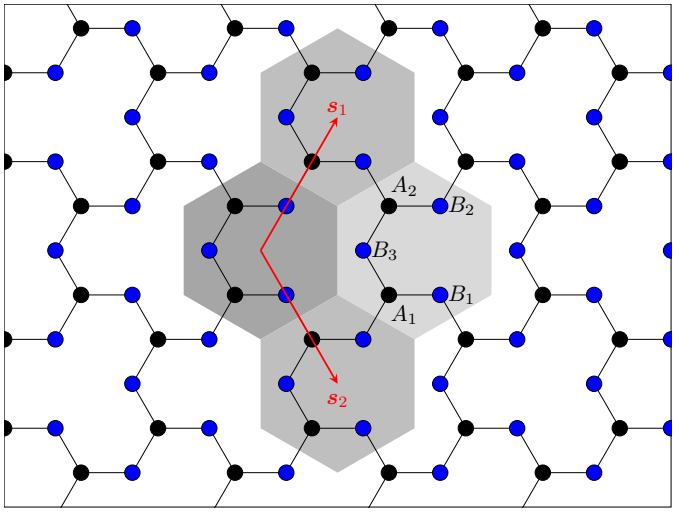

Figure 6.A.1: Lattice structure of "supergraphene" where all atoms of one given colour and sublattice are removed from the honeycomb lattice. The underlying Bravais lattice is triagonal with lattice vectors $\boldsymbol{s}_1 = (3a/2)(1, \sqrt{3})$, $\boldsymbol{s}_2 = (3a/2)(1, -\sqrt{3})$; the unit cell contains five atoms at positions $a(\cos n\pi/3, \sin n\pi/3), n = 1, \ldots, 5$ relative to the centres of the hexagonal Wigner-Seitz cells.

To obtain the dispersion of supergraphene, we need to solve the following set of equations

$$\varepsilon\Psi_{A_1}(\boldsymbol{R}) = -t\left[\Psi_{B_1}(\boldsymbol{R}) + \Psi_{B_2}(\boldsymbol{R} - \boldsymbol{s}_1) + \Psi_{B_3}(\boldsymbol{R})\right] \tag{6.3a}$$

$$\varepsilon\Psi_{A_2}(\boldsymbol{R}) = -t\left[\Psi_{B_1}(\boldsymbol{R} - \boldsymbol{s}_2) + \Psi_{B_2}(\boldsymbol{R}) + \Psi_{B_3}(\boldsymbol{R})\right] \tag{6.3b}$$

$$\varepsilon\Psi_{B_1}(\boldsymbol{R}) = -t\left[\Psi_{A_1}(\boldsymbol{R}) + \Psi_{A_2}(\boldsymbol{R} + \boldsymbol{s}_2)\right] \tag{6.3c}$$

$$\varepsilon\Psi_{B_2}(\boldsymbol{R}) = -t\left[\Psi_{A_1}(\boldsymbol{R} + \boldsymbol{s}_1) + \Psi_{A_2}(\boldsymbol{R})\right] \tag{6.3d}$$

$$\varepsilon\Psi_{B_3}(\boldsymbol{R}) = -t\left[\Psi_{A_1}(\boldsymbol{R}) + \Psi_{A_2}(\boldsymbol{R})\right]. \tag{6.3e}$$

For a specific momentum,

$$\Psi_{\eta,\boldsymbol{k}}(\boldsymbol{R}) = e^{i\boldsymbol{k}\cdot\boldsymbol{R}}\phi_\eta(\boldsymbol{k}), \qquad \eta \in \{A_1, A_2, B_1, B_2, B_3\}\,, \tag{6.4}$$

this turns into the matrix equation

$$-tM_{\boldsymbol{k}}\Phi(\boldsymbol{k}) = \varepsilon(\boldsymbol{k})\Phi(\boldsymbol{k}), \tag{6.5}$$

where

$$M_{\boldsymbol{k}} = \begin{pmatrix} 0 & 0 & 1 & z_1^* & 1 \\ 0 & 0 & z_2^* & 1 & 1 \\ 1 & z_2 & 0 & 0 & 0 \\ z_1 & 1 & 0 & 0 & 0 \\ 1 & 1 & 0 & 0 & 0 \end{pmatrix}, \qquad \Phi(\boldsymbol{k}) = \begin{pmatrix} \phi_{A_1}(\boldsymbol{k}) \\ \phi_{A_2}(\boldsymbol{k}) \\ \phi_{B_1}(\boldsymbol{k}) \\ \phi_{B_2}(\boldsymbol{k}) \\ \phi_{B_3}(\boldsymbol{k}) \end{pmatrix}, \qquad z_j = e^{i\boldsymbol{k}\cdot\boldsymbol{s}_j}. \tag{6.6}$$

The corresponding secular equation

$$0 = \det\left(M_{\boldsymbol{k}} + \frac{\varepsilon}{t}\mathbb{1}\right) = \frac{\varepsilon}{t}\left(\frac{\varepsilon^4}{t^4} - 6\frac{\varepsilon^2}{t^2} + 9u_{\boldsymbol{k}}\right) \tag{6.7a}$$

with

$$u_{\boldsymbol{k}} = \frac{2}{9}\left(3 - \cos 3k_x a - 2\cos\frac{3k_x a}{2}\cos\frac{3\sqrt{3}k_y a}{2}\right), \tag{6.7b}$$

is readily solved by

$$\varepsilon^{(0)}(\boldsymbol{k}) = 0, \qquad \varepsilon^{(1)}(\boldsymbol{k}) = \pm\sqrt{3}t\sqrt{1-\sqrt{1-u_{\boldsymbol{k}}}}, \qquad \varepsilon^{(2)}(\boldsymbol{k}) = \pm\sqrt{3}t\sqrt{1+\sqrt{1-u_{\boldsymbol{k}}}}. \tag{6.8}$$

For small values of $\boldsymbol{k}$, the $\varepsilon^{(1)}$-branch can be approximated by

$$\varepsilon^{(1)}(\boldsymbol{k}) \approx \pm\frac{3at}{2}\sqrt{k_x^2 + k_y^2}, \tag{6.9}$$

i.e. by the very same Dirac cone as in graphene. The supergraphene band structure is further explored in Fig. 6.A.2.

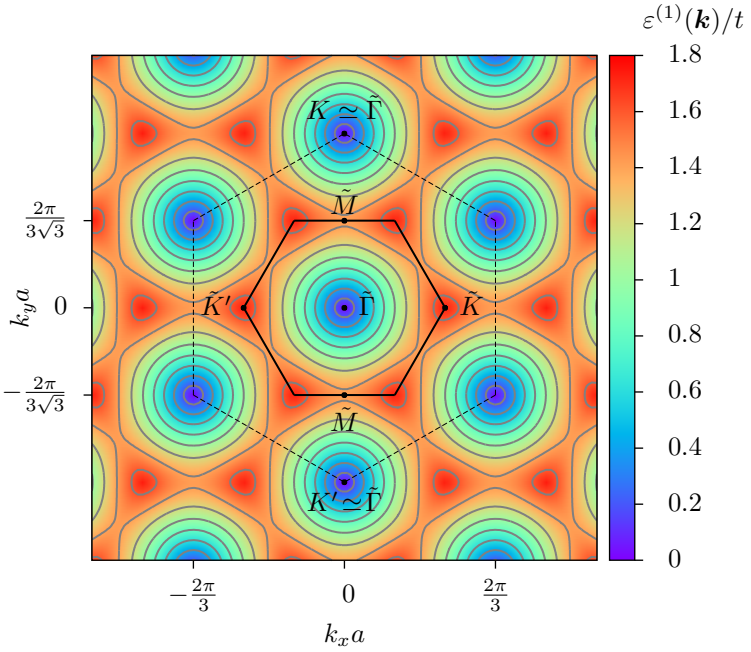

(a) Contour plot of the $\varepsilon^{(1)}$-branch of the energy dispersion. The solid black hexagon with corners $\tilde{K}$ and $\tilde{K}'$ represents the Brillouin zone of supergraphene and contains a single Dirac cone at its center $\tilde{\Gamma}$. Because the RGF calculation assumes graphene leads attached to what approaches the supergraphene lattice for large nL^2, it is important to note that this $\tilde{\Gamma}$ point is the same (up to a reciprocal lattice vector) as K and K' which form the corners of the graphene Brillouin zone.

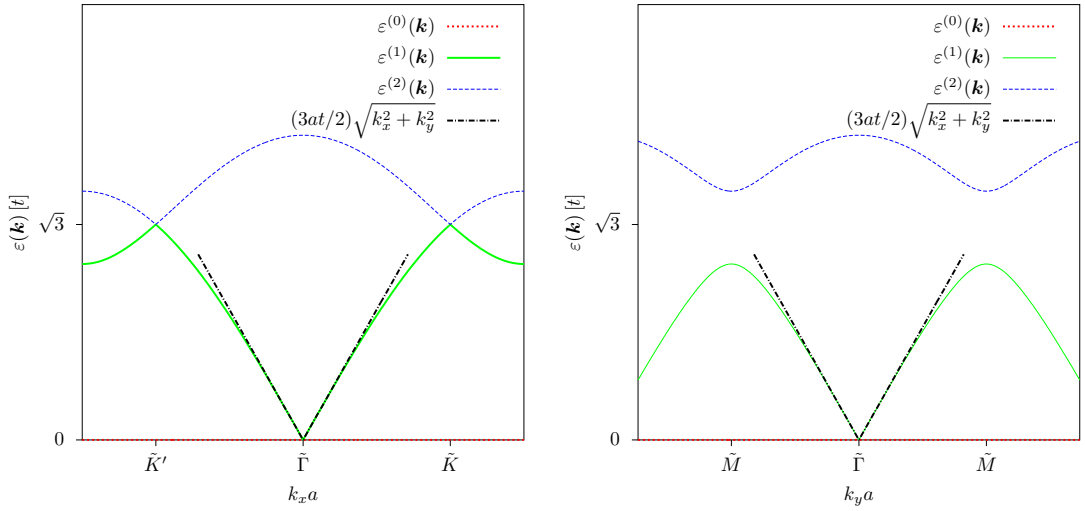

(b) Energy dispersion of supergraphene along the k_x- and k_y-axis. The Dirac cone around $\boldsymbol{k} = \boldsymbol{0}$ has the same slope $\hbar v = 3at/2$ as the cones in graphene.

Figure 6.A.2: Energy dispersion of supergraphene. As far as the dispersion around the charge neutrality point is concerned, the only important difference between graphene and supergraphene seems to be the number of distinct Dirac cones in the Brillouin zone.

References of Chapter 6

[1] Groth, C. W., Wimmer, M., Akhmerov, A. R. & Waintal, X. Kwant: a software package for quantum transport. *New Journal of Physics* **16**, 063065 (2014).

[2] Schelter, J., Ostrovsky, P., Gornyi, I. V., Trauzettel, B. & Titov, M. Color-dependent conductance of graphene with adatoms. *Physical Review Letters* **106**, 166806 (2011).

[3] Ando, T., Nakanishi, T. & Igami, M. Effective-Mass Theory of Carbon Nanotubes with Vacancy. *Journal of the Physical Society of Japan* **68**, 3994–4008 (1999).

[4] Ostrovsky, P., Titov, M., Bera, S., Gornyi, I. V. & Mirlin, A. D. Diffusion and Criticality in Undoped Graphene with Resonant Scatterers. *Physical Review Letters* **105**, 266803 (2010).

[5] Schelter, J. *The Aharonov-Bohm Effect and Resonant Scattering in Graphene*. Ph.D. thesis, University of Wuerzburg.

[6] Abanin, D. A., Shytov, A. V. & Levitov, L. S. Peierls-Type Instability and Tunable Band Gap in Functionalized Graphene. *Physical Review Letters* **105**, 086802 (2010).

[7] Cheianov, V. V., Syljuasen, O., Altshuler, B. L. & Fal'ko, V. I. Sublattice ordering in a dilute ensemble of monovalent adatoms on graphene. *EPL (Europhysics Letters)* **89**, 56003 (2010).

[8] Ostrovsky, P. *et al.* Density of states in a two-dimensional chiral metal with vacancies. *arXiv.org* (2014). 1404.6139v2.

[9] Cresti, A., Ortmann, F., Louvet, T., Van Tuan, D. & Roche, S. Broken Symmetries, Zero-Energy Modes, and Quantum Transport in Disordered Graphene: From Supermetallic to Insulating Regimes. *Physical Review Letters* **110**, 196601 (2013).

[10] Tworzydło, J., Trauzettel, B., Titov, M., Rycerz, A. & Beenakker, C. W. J. Sub-Poissonian Shot Noise in Graphene. *Physical Review Letters* **96** (2006).